

REVIEW ARTICLE

Quantum Magnetism in Minerals

Dmytro S. Inosov^{1,*}¹Institut für Festkörper- und Materialphysik, TU Dresden, D-01069 Dresden, Germany

Abstract. The discovery of magnetism by the ancient Greeks was enabled by the natural occurrence of lodestone—a magnetized version of the mineral magnetite. Nowadays, natural minerals continue to inspire the search for novel magnetic materials with quantum-critical behavior or exotic ground states such as spin liquids. The recent surge of interest in magnetic frustration and quantum magnetism was largely encouraged by crystalline structures of natural minerals realizing pyrochlore, kagomé, or triangular arrangements of magnetic ions. As a result, names like azurite, jarosite, volborthite, and others, which were barely known beyond the mineralogical community a few decades ago, found their way into cutting-edge research in solid-state physics. In some cases, the structures of natural minerals are too complex to be synthesized artificially in a chemistry lab, especially in single-crystalline form, and there is a growing number of examples demonstrating the potential of natural specimens for experimental investigations in the field of quantum magnetism. On many other occasions, minerals may guide chemists in the synthesis of novel compounds with unusual magnetic properties. The present review attempts to embrace this quickly emerging interdisciplinary field that bridges mineralogy with low-temperature condensed-matter physics and quantum chemistry.

Keywords: magnetic minerals, quantum magnetism, frustration, low-dimensional spin models

PACS: 75.30.-m — intrinsic properties of magnetically ordered materials;
75.10.Jm — models of magnetic ordering, including quantum spin frustration;
91.60.Pn — magnetic properties of minerals.

Submitted to: *Advances in Physics*

*Corresponding author. E-mail: dmytro.inosov@tu-dresden.de

Contents

1 Historical introduction	4
2 Coupled spin dimers	7
2.1 Short motivation and physical models	7
2.2 Malachite: A 2D network of antiferromagnetically coupled dimers	8
2.3 Callaghanite: Nearly compensated solitary dimers	10
2.4 Urusovite: Corrugated honeycomb planes prone to dimerization	11
2.5 Clinoclase: Nonequivalent dimers with two energy scales	12
3 Quantum spin chains	14
3.1 The assortment of spin chains and ladders	14
3.2 Tolbachite: Cycloidal helimagnet with field-driven ferroelectricity	16
3.3 Trippkeite: A linear-chain ferromagnet close to criticality	17
3.4 Linarite: Frustrated spin chains with helimagnetic order	18
3.5 Azurite: Realization of the generalized diamond-chain model	20
3.6 Euchroite: Frustrated sawtooth chains with a spin gap	23
3.7 Fedotovite: Haldane chains of edge-shared tetrahedral spin clusters	23
3.8 Dioptase: A hexagonal network of ferromagnetically coupled AFM chains	25
3.9 Szenicsite and antlerite: Frustrated spin chains near the Majumdar-Ghosh point	27
4 Kagomé systems	28
4.1 The perplexing magnetism in kagomé layers	28
4.2 Jarosites: Classical spins on the kagomé lattice	30
4.3 Herbertsmithite and related $S = 1/2$ kagomé-layer antiferromagnets	33
4.4 Kapellasite vs. haydeeite: The role of further-neighbor exchange	36
4.5 Volborthite and vesignieite: Nonequivalent bonds resulting from lattice distortions	39
4.6 Francisite: buckled kagomé planes with bond frustration	44
4.7 Brochantite and Zn-brochantite: A new route to a kagomé spin liquid	47
4.8 Claringbullite and barlowite: Three-dimensionally coupled kagomé planes	48
5 Other layered quasi-2D lattices	49
5.1 The variety of two-dimensional crystal structures	49
5.2 Delafossite and mcconnellite: Classical spins on the triangular lattice	51
5.3 Devilline: Distorted spin- $\frac{1}{2}$ triangular lattice	54
5.4 Spangolite: A maple-leaf lattice antiferromagnet	56
5.5 Diaboleite: A spin- $\frac{1}{2}$ square lattice without frustration	57
5.6 Shattuckite: A combination of CuO_2 planes and ribbons	58
5.7 Langite and Wroewolfeite: Coexistence of magnetic order and quantum disorder	59

6 Three-dimensional frustrated lattices	60
6.1 Magnetic frustration on 3D crystal lattices	60
6.2 Atacamite and other polymorphs of $\text{Cu}_2(\text{OH})_3\text{Cl}$: Distorted pyrochlore structure . .	61
6.3 Melanothallite: A pyrochlore-lattice antiferromagnet with multiferroic properties .	64
6.4 Choloalite: A 3D quantum spin liquid on a hyper-hyperkagomé lattice	65
6.5 Magnetic minerals of the perovskite group	66
7 Molecular magnets	67
7.1 Magnetism in spin clusters	67
7.2 Olivenite and libethenite: A weakly interacting network of AFM tetramer units . .	69
7.3 Boleite: Cu_{24} clusters in the form of truncated cubes	70
7.4 Tschörtnerite: Cubooctahedral Cu_{12} clusters	72
8 Itinerant magnetism	72
8.1 Mackinawite: The natural prototype of an iron-based superconductor	72
9 Summary and outlook	73

1. Historical introduction

Many developments in solid-state physics and crystallography were historically inspired by observations on naturally occurring minerals. Various phenomena in condensed-matter physics were first discovered in natural samples, which had unsurpassed quality as compared to synthetic materials before the advent of modern chemical and crystal-growth technology [1, 2]. Among the most eminent examples are the first observations of ferromagnetism in lodestone dating back to the Greek philosopher and engineer *Thales of Miletus* in the 6th century BC [3]. Alchemists of the early 17th century were awed by Vincenzo Casciorola's discovery of phosphorescence in the "Bologna stone", or *lapis solaris* (presumably baryte, BaSO₄) [4]. At the beginning of the 19th century, optical activity was discovered by François Arago in one of Earth's most common minerals, quartz [5]. Then, in 1875, Weber noticed a deviation in the heat capacity of diamond from the Dulong-Petit law at room temperature [6], which was ultimately explained in Einstein's seminal paper of 1907 that became one of the cornerstones of quantum mechanics [7]. However, synthetic diamonds remained unavailable until 1955 [8] and lacked quality until much later. From more recent examples, bulk electronic band structure of the prototypical layered material graphite has been studied using quantum oscillations [9] and modern angle-resolved photoelectron spectroscopy on natural single crystals [10, 11], as they are often superior in quality to synthetic graphite samples.

In modern times, experimental solid-state physics predominantly relies on synthetic crystals, whose quality and chemical purity can be well controlled for an ever increasing number of materials. Therefore, today's condensed-matter physics has largely departed from mineralogy and geophysical sciences in its need for samples. Yet, there have always been exceptions to this general tendency, especially in the field of magnetism. In the early 1950's, the first triple-axis neutron spectrometer was put together by Brockhouse at the Chalk River NRX reactor in Canada [12, 13], which enabled the first direct measurements of phonon and magnon excitations by inelastic neutron scattering (INS). For the spin-wave measurement, Brockhouse needed a large single crystal of a substance in which magnetic scattering dominated over nuclear scattering, with a high enough Curie or Néel temperature, and with small neutron absorption and incoherent scattering cross-sections [14]. He rightly judged that magnetite (Fe₃O₄) is the best possibility in spite of its complex ferrimagnetic structure, which was already known by that time from the works of Néel [15, 16]. The platelike specimen with a size of 6.3×3.8×0.3 cm³ (~37 g) was cut from a natural single crystal of magnetite, which contained multiple impurities (Ti, Mn, Al, Si) on the Fe sites, but nevertheless facilitated the first direct observation of ferromagnetic (FM) spin waves and the first measurement of their low-energy dispersion. Later, spin-wave measurements on magnetite were repeated at low temperatures below the Verwey transition ($T_V \approx 120$ K), but revealed no significant changes in the dispersion [17].

Unlike magnetite, another famous iron-bearing mineral hematite (α -Fe₂O₃, with a corundum crystal structure) is an antiferromagnet with a very high Néel point, $T_N = 960$ K. In addition, weak ferromagnetism is observed above the so-called Morin transition ($T_M \approx 263$ K) due to a spin-flop rearrangement of magnetic moments [20, 21]. This caused much confusion before the 1950's when its antiferromagnetic (AFM) structure was finally confirmed by neutron diffraction [22, 23]. The

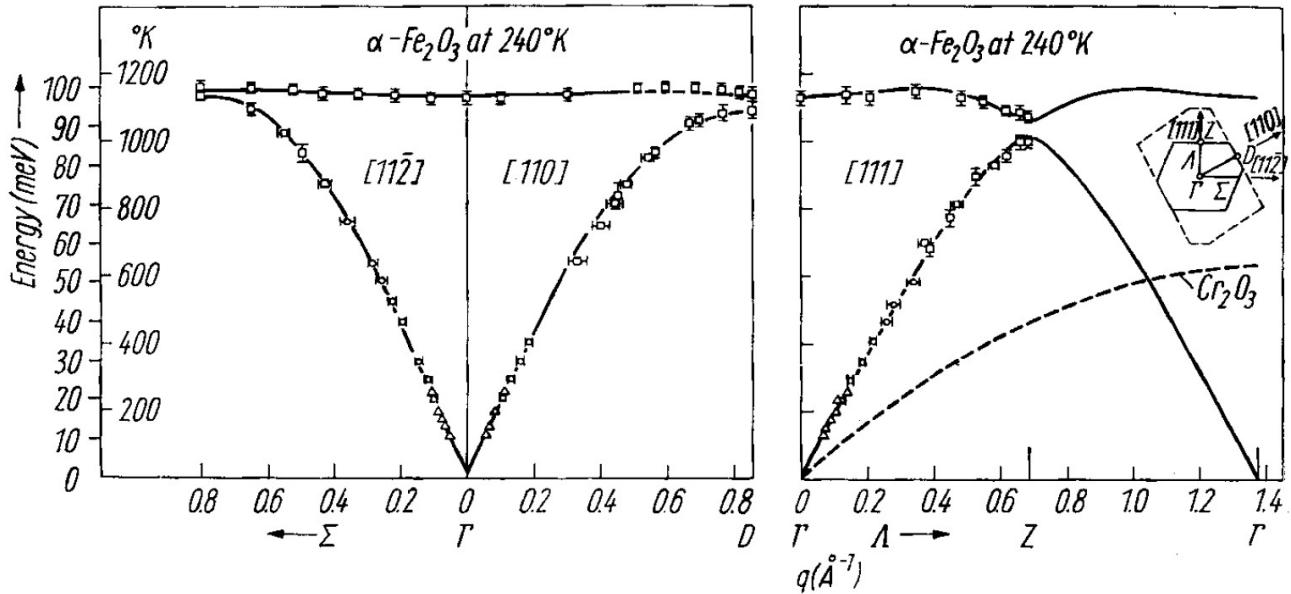


Figure 1. First INS measurements of spin-wave dispersions in a 48 g natural single crystal of hematite along three principal directions, which were used to extract exchange parameters of the Heisenberg model (solid curve). The dashed line is a comparison with the dispersion relation of Cr_2O_3 [18]. Reproduced from Ref. [19], copyright by John Wiley & Sons, Inc.

dispersion relations for AFM spin waves in hematite ($\alpha\text{-Fe}_2\text{O}_3$), shown in Fig. 1, were reported in 1970 by Samuels and Shirane [19], from which they obtained Heisenberg exchange interactions up to the 5th nearest neighbor. They also confirmed linear dispersion relationships for low-energy AFM spin waves, predicted by Hulthén [24], and accurately measured the corresponding spin-wave velocities. Hematite is found not only as a pure mineral, but also in the form of nanoscale exsolution lamellae in the ilmenite host (FeTiO_3). This mineral intergrowth, known as hemoilmenite, possesses a large natural remanent magnetization (NRM) that has been claimed responsible for Earth's local magnetic field anomalies [25, 26]. A recent polarized neutron diffraction study on a single-crystalline hemoilmenite specimen from South Rogaland, Norway, has confirmed that lamellar magnetism of hematite can fully account for the observed NRM at ambient temperature [27]. In the resulting model, magnetic moments in contact layers between exsolution lamellae that align parallel to the magnetizing field combine with the canted AFM moments above the Morin transition that are approximately orthogonal to the field to produce a net magnetic moment at an intermediate angle with a saturation value of $\sim 56^\circ$.

Another example of a classical antiferromagnet that was investigated by neutron scattering is hauerite (MnS_2 , pyrite structure), which has a habit of forming large cm-sized octahedral single crystals of high natural quality. It adopts a commensurate collinear AFM structure with a $\mathbf{k} = (1 \frac{1}{2} 0)$ wave vector below $T_N = 48 \text{ K}$ [28]. Above this temperature, diffuse critical scattering of magnetic origin was revealed by INS at an incommensurate wave vector $(1 0.44 0)$, with a temperature dependence characteristic of a lock-in transition of a three-dimensionally (3D) ordered system [29, 30]. The same study also found two branches of spin-wave excitations: a nearly flat one at about 2 meV and a strongly dispersing one (2–7 meV) with a spin gap of 2 meV

that is unusually large for the Mn^{2+} ion in the spin- $\frac{5}{2}$ state [29]. Very recently, the lock-in transition to the commensurate AFM phase received a natural explanation as a result of a tiny tetragonal distortion of the lattice with the c/a ratio of 1.0006 that could be resolved in a synchrotron x-ray diffraction (XRD) experiment [31]. This distortion is sufficient to lift the geometric frustration on the face-centered cubic (fcc) magnetic sublattice of Mn^{2+} ions and stabilize long-range AFM order. Another recent study revealed that hauerite undergoes an unprecedented collapse of the unit cell volume by 22% under the application of hydrostatic pressure above 11 GPa [32]. This occurs as a result of a transition to the much denser arsenopyrite structure that favors low-spin state of Mn and leads to the total loss of magnetic moments.

As can be seen from the few examples of classical ferro- and antiferromagnets listed above, until the end of the 20th century neutron scattering had been applied only sporadically to study magnetic dynamics in natural minerals. The applications of neutron scattering to the Earth and mineral sciences in this period have been reviewed in a number of books and articles [33–35], but their focus was mainly on structural properties, phononic spectra, and magnetic phase transitions. A substantial body of literature also covers magnetic properties of minerals from the perspective of geophysics and geochemistry [33, 36–41], with an emphasis on ferro- and ferrimagnetism at ambient or elevated temperatures and pressures that can occur in the Earth’s crust. More recently, some of the iron-bearing compounds that occur as natural minerals also attracted attention of material scientists because of their intriguing magnetic properties that are promising for applications. To name a few examples, the polar magnet $Fe_2Mo_3O_8$ (kamiokite) has been discussed because of its field-driven multiferroic and pyroelectric properties [42–44]. As a result of its magnetic structure that represents an antiferromagnetic alignment of weakly ferrimagnetic layers [45], it exhibits giant magnetoelectricity with a differential magnetoelectric coefficient approaching 10^4 ps/m [42]. Kurumaji *et al.* [46] recently revealed an electric-field active magnon mode (electromagnon) in $Fe_2Mo_3O_8$ using terahertz spectroscopy and suggested possible spin configurations for these excitations. Later, linear magnetoelectric effect was also observed in α -FeOOH (góthite), persisting above room temperature because of the high $T_N \approx 400$ K [47]. Another mineral $LiFePO_4$ (triphylite) is an olivine-type compound that attracted considerable interest as a storage cathode material for rechargeable lithium batteries [48]. From the point of view of magnetism, it is a collinear $S = 2$ antiferromagnet with a Néel temperature of 52 K [49, 50]. It was recently suggested that Fe^{2+} ions in this compound undergo a high-spin to low-spin transition at pressures of the order of 72 GPa, which is unprecedently high among Fe-bearing minerals [51]. About a year ago, high-pressure structural and magnetic properties were also reported for $FeCO_3$ (siderite) [52].

However, all presented examples are “classical” magnets, i.e. compounds with well developed magnetic order and high value of the local spin, for which classical (that is, non-quantum) models of magnetism are valid to a good approximation. Despite their abundance in the mineral world, they will not be central for the present review. Here I will focus mainly on “quantum” magnets that exhibit emergent phenomena that cannot be captured by the classical models. In a rather vague definition, this includes spin- $\frac{1}{2}$ systems and higher-spin lattices with strongly pronounced magnetic frustration that tends to suppress conventional long-range magnetic order and promote more exotic magnetic states at low temperatures. At the start of the new millennium, we saw a surge of interest

in low-temperature quantum magnetism, magnetic frustration, and exotic magnetic phases such as spin liquids [53–59]. This stimulated an intensive search for new materials realizing complex crystal structures with specific geometries of magnetic lattices. It was noticed that intricately connected spin- $\frac{1}{2}$ magnetic sublattices are found in many copper-bearing minerals that are difficult or impossible to reproduce artificially in the form of large single crystals. Among such structures are those that realize various spin-dimer and spin-chain models, two- and three-dimensional geometrically frustrated lattices, as well as quasi-isolated frustrated magnetic clusters that are natural archetypes of quantum molecular magnets. The constantly rising number of experimental and theoretical works focusing on low-temperature magnetism in such natural samples and the even broader variety of minerals that could be of potential interest for future studies manifest the emergence of a new interdisciplinary field that bridges mineralogy with solid-state magnetism. To the best of my knowledge, no published review has so far collected and classified low-temperature studies on magnetic minerals. Therefore, the goal of the present article is to fill this niche by summarizing recent experimental and theoretical work performed on natural samples as well as on their very close synthetic analogs that were motivated by the magnetic minerals. The main emphasis of this review will be on magnetic structure and spin dynamics, with the aim of providing a firm standpoint for future developments in this relatively young field of research.

2. Coupled spin dimers

2.1. *Short motivation and physical models*

Dimerized quantum spin systems are among the simplest and best studied physical models that serve as textbook examples for the realization of quantum critical phase transitions [60, 61]. An isolated magnetic dimer consisting of two antiferromagnetically coupled $S = 1/2$ Heisenberg spins with an exchange constant $J > 0$ has an $S = 0$ singlet ground state and an $S = 1$ excited triplet state. Therefore, its magnetic excitation spectrum consists of a triply degenerate singlet-triplet transition at the energy J , which can be split by the application of an external magnetic field. With the introduction of interdimer interactions, the triplet excitation can propagate through the lattice, thereby acquiring a dispersion. Nevertheless, the spectrum remains gapped and no long-range ordered ground state is stabilized until a quantum critical point (QCP) is reached at a certain critical value of the interdimer coupling, $J' = J_c$. The archetypal model materials that realize a quantum-disordered ground state along this scenario (upon neglecting weaker interdimer interactions that are not necessarily unimportant) are coupled-dimer antiferromagnets KCuCl_3 and TlCuCl_3 [62–64], characterized by different values of the alternation ratio $\alpha = J'/J = 1 - |\Delta/J|$ that controls the proximity to the QCP. Here Δ is the spin gap, and the estimates $\alpha \approx 0.3$ and $\alpha \approx 0.8$ were obtained for the KCuCl_3 and TlCuCl_3 systems, respectively [65]. In an applied magnetic field, the triplet excitation splits into three branches due to the Zeeman effect [66, 67], ultimately leading to a field-tuned QCP associated with the Bose-Einstein condensation of the triplet states at a certain critical field B_c where the energies of the lower Zeeman-split triplet component and the ground-state singlet intersect [68]. In TlCuCl_3 , a long-range magnetic order is already induced at 6 T, so that this QCP is easily accessible in an experiment.

A variety of models with different critical alternation ratios α_c arise depending on the specific lattice of interdimer interactions, several of them shown in Fig. 2. For one-dimensional (1D) spin-chain compounds, one arrives at the alternating Heisenberg chain model [73] embodied in the above-mentioned copper chlorides, with a QCP at $\alpha_c = 1$, or various dimerized spin-ladder models [69, 74, 75]. A two-leg spin ladder emerges, for instance, in the famous “telephone number compound” $\text{Sr}_{14}\text{Cu}_{24}\text{O}_{41}$ [76]. Two-dimensional (2D) models include the exactly solvable Shastry-Sutherland lattice model with orthogonal dimers [71], manifested in $\text{SrCu}_2(\text{BO}_3)_2$ [77, 78], which has two quantum-critical transitions at $\alpha_{c1} \approx 0.675$ and α_{c2} that has varying estimates from 0.765 [79] to 0.86 [72]. Numerous theoretical studies exist also for various other dimerized antiferromagnets arranged in a staggered ($\alpha_c \approx 0.397$), columnar ($\alpha_c \approx 0.524$), herringbone ($\alpha_c \approx 0.4$), or bilayer ($\alpha_c \approx 0.397$) dimer lattices (see Ref. [70] and references therein).

From the materials perspective, compounds that can serve as model systems for the realization of these assorted dimer lattices in the proximity to criticality are of the greatest interest. Therefore, the search continues among synthetic compounds as well as natural minerals. Particularly exciting are those systems that exhibit high sensitivity of the exchange constants to external parameters, such as hydrostatic pressure, offering the possibility to vary the alternation ratio experimentally in order to approach the QCP or stabilize new quantum ground states. As will become clear from the following examples, this situation is common in natural copper minerals, where the superexchange coupling sensitively depends on the Cu–O–Cu bond angles that can be tuned by pressure. In addition, some minerals realize less common and more complicated dimer structures that provide a new playground for theorists and serve as real-world challenges for testing the accuracy and reliability of different computational methods beyond simple purist models.

2.2. Malachite: A 2D network of antiferromagnetically coupled dimers

The carbonate mineral malachite, with the formula $\text{Cu}_2\text{CO}_3(\text{OH})_2$, is famous as a gemstone and has been mined as a copper ore since antiquity. It has a monoclinic crystal structure (space group $P2_1/a$) in which pairs of edge-sharing planar CuO_4 plaquettes form Cu_2O_6 dimers that

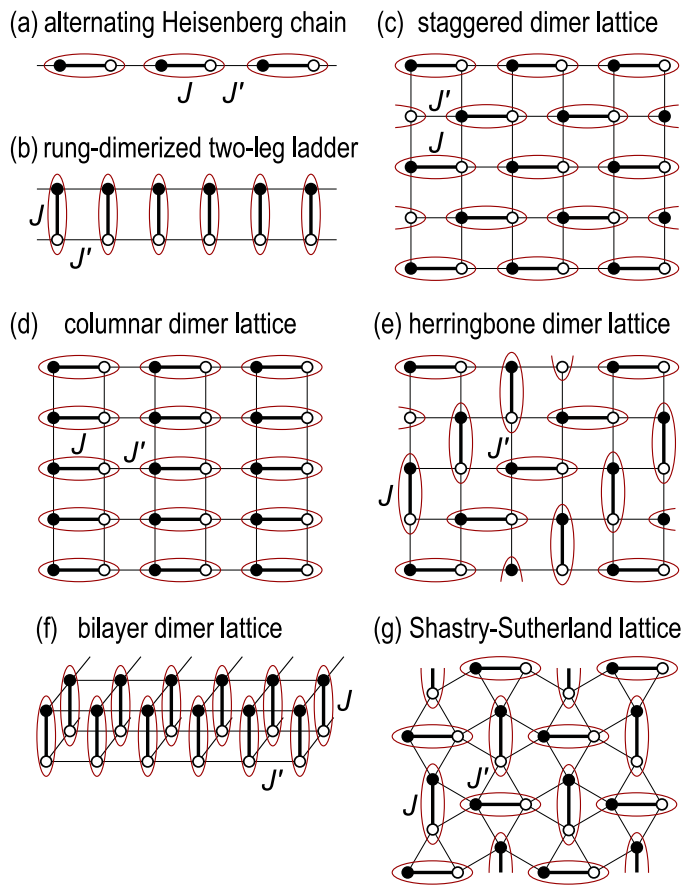


Figure 2. Some of the most commonly studied dimer models [69–72].

are arranged into buckled dimer chains [see Fig. 3 (a)]. The intradimer exchange interaction between the spin- $\frac{1}{2}$ Cu^{2+} ions is AFM with $J_1 \equiv J \approx 190$ K, while the interdimer exchange within the chains is about twice weaker, $J_2 \equiv J' \approx 90$ K, as estimated from susceptibility data that could be well fitted by the alternating Heisenberg chain model [80–82]. While reporting correct values for the leading exchange interactions, the first work by Janod *et al.* misplaced the spin dimers in the lattice, assuming that the strongest J_1 coupling acts between the structural dimers, as one might expect from the larger Cu–O–Cu bridging angle of 122.1° in accordance to the Goodenough–Kanamori–Anderson (GKA) rules [83–85]. Lebernegg *et al.* later demonstrated that malachite is an exception among Cu^{2+} systems, in which structural and magnetic dimers coincide [81]. Thermodynamic measurements reveal no signatures of magnetic order or spin freezing in this system down to temperatures as low as 0.4 K [82]. The value of the spin gap, $\Delta \approx 130$ K (or 11 meV), was estimated from susceptibility data on three natural specimens of malachite [80, 81] and was recently confirmed by direct neutron-spectroscopy measurements on a deuterated powder sample [82] that are shown in Fig. 3 (b), while single-crystal INS measurements are still lacking.

Malachite is a rare example among Cu minerals, for which accurate hydrogen positions in the crystal structure, whose bonding angles have a strong influence on the exchange couplings, are available both from experiments and from structural optimization within density functional theory (DFT). This enabled reliable theoretical calculations of the exchange constants, showing good quantitative agreement with the experimental values [81, 82]. Further, DFT+ U was also used to calculate isotropic interchain interactions $J_3 \dots J_6$, resulting in a value of $J_6 \equiv J_\perp$ along the b axis of similar magnitude to J_2 , while all remaining exchange constants were found to be considerably weaker. Based on their neutron-scattering results, the authors of Ref. [82] come to the conclusion that this coupling scheme places malachite “between strongly coupled alternating chains, square lattice antiferromagnets, and infinite-legged ladders”. They find that a 2D depleted staggered dimer model (in contrast to the 1D spin-chain model originally suggested by Janod

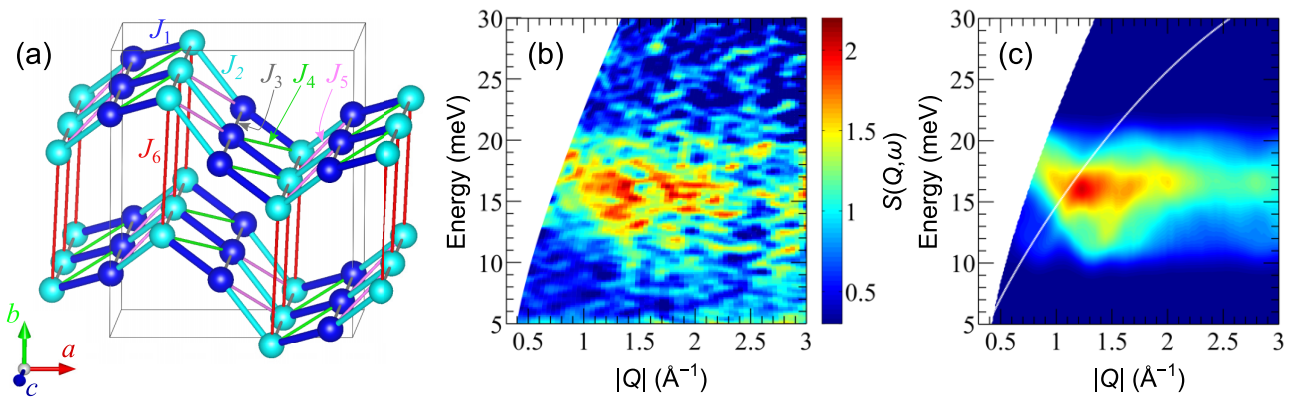


Figure 3. (a) Structure of the magnetic sublattice and the network of exchange pathways in malachite. (b) Background-subtracted neutron scattering intensity, $S(Q, \omega)$, measured on a fully deuterated powder sample of malachite using the MARI time-of-flight spectrometer at ISIS, UK, operated with an incident neutron energy $E_i = 80$ meV. (c) Powder-averaged model calculations that reproduce the experimental data within the harmonic triplon approximation [70]. The figure is reproduced with permission from Ref. [82], copyright by the American Physical Society.

et al. [80]) is well suited for the description of malachite [see Fig. 3 (c)] because of the similar values of interdimer couplings parallel (J') and perpendicular (J_{\perp}) to the chains: $J'/J = 0.34$ and $J_{\perp}/J = 0.26$. These values are smaller than the critical interdimer coupling strength J'_c at the QCP separating a dimer state and AFM order, $J'_c/J = 1/2$, which explains the large size of the spin gap and the absence of a long-range magnetic order in malachite [82].

In addition, full-relativistic calculations show that the lack of inversion symmetry along the exchange pathways gives rise to non-negligible antisymmetric Dzyaloshinskii-Moriya interactions (DMI), which are important for understanding the finite values of the low-field uniform magnetization that are observed in experiments despite the large value of the spin gap [81, 86]. There are two nonequivalent DMI vectors, \mathbf{D}_1 and \mathbf{D}_2 , for the two Cu–Cu bonds within the chain, with the relatively large $|\mathbf{D}|/J$ and $|\mathbf{D}'|/J'$ ratios of 0.11 and 0.26, respectively [81]. The expected influence of DMI on the excitation spectrum is the splitting of the triplets of the order of $10^{-3} J_1 \approx 0.016$ meV, which is too small to be detectable on a polycrystalline sample, but could possibly be resolved in future experiments on single crystals.

Finally, Lebernegg *et al.* took advantage of the experimental high-pressure structural refinement available from XRD data, which they complemented with calculated hydrogen positions optimized within the generalized gradient approximation (GGA), to estimate the expected changes in the individual exchange parameters and the spin gap energy under the application of hydrostatic pressure [81]. They found that the intradimer exchange interaction J_1 tends to decrease, while the interdimer coupling J_2 remains nearly constant within 15%, so that both become approximately equal at pressures of the order of 5 GPa. This implies a nearly twofold increase in the J'/J ratio, which may lead to the stabilization of a long-range magnetic order. At the same time, the dominant interchain coupling J_{\perp} is considerably suppressed by pressure according to the calculations, indicating a crossover from the 2D dimer network to quasi-1D uniformly coupled spin chains. As a result, the calculated value of the spin gap is also suppressed under pressure with an average rate of ~ 1 meV/GPa. The predicted sensitivity of the intradimer coupling to pressure should serve as a motivation for more detailed experimental studies of malachite, in particular to establish its magnetic phase diagram under pressure and to search for low-temperature magnetically ordered phases.

2.3. Callaghanite: Nearly compensated solitary dimers

The empirical GKA rules [83–85] predict how superexchange depends on the ion-ligand-ion bridging angle. According to these rules, a 180° superexchange of two magnetic ions with partially filled d shells is antiferromagnetic, whereas a 90° superexchange is ferromagnetic. At intermediate angles the AFM and FM interactions tend to compensate each other, resulting in very weak coupling even for closely spaced ions. For Cu–O–Cu bonds, this transition occurs in the range of 95°–98° [87] and corresponds to a situation where first-principles calculations become less reliable in predicting not only the absolute value, but even the sign of the magnetic interactions [88]. Moreover, the suppression of the nearest-neighbor exchange through this mechanism enhances the relative importance of further-neighbor exchange paths that could be otherwise neglected. Therefore, systems that realize structures with compensated exchange are expected to show complicated

magnetic behavior as a result of frustration among multiple weak interactions, demonstrate high sensitivity of the ground state to external parameters such as pressure, and represent ideal systems for testing the accuracy and reliability of different computational methods.

According to Lebernegg *et al.*, the dimer compound $\text{Cu}_2\text{Mg}_2(\text{CO}_3)(\text{OH})_6 \cdot 2\text{H}_2\text{O}$, which is found in nature in the form of a violet-blue mineral known as callaghanite (Fig. 4), is a perfect realization of the described scenario [88].

Unlike malachite, this mineral is very rare and has been much less studied by physical methods. Its structure, refined from XRD data apart from the hydrogen positions [89], is characterized by the monoclinic space group $C2/c$ and hosts $\text{Cu}_2(\text{OH})_6$ structural dimers separated by weakly bonded carbonate groups and water molecules. The interdimer interactions are ferromagnetic and very weak, not exceeding 1.5 K (0.12 meV). The lattice symmetry also forbids DMI within the dimers.

However, magnetization and specific-heat measurements reveal that even the strongest AFM intradimer coupling J is very weak in this compound, of only 7 K (0.6 meV), and is therefore difficult to evaluate from first principles [88]. This results in a relatively low value of magnetic field, at which the magnetization saturates, of the order of 14 T.

Such an unusual behavior is a consequence of the Cu–O–Cu bridging angle of 96.14° within the dimers, which falls within the range where the compensation of AFM and FM exchange interactions is expected. At ambient pressure, the system shows quantum paramagnetic behavior and no signs of magnetic ordering down to the lowest measured temperatures. Still, the sensitivity of the Cu–O–Cu bridging angle to pressure may result in a situation when the AFM interaction is reduced even further by very moderate pressures, leading to a magnetic phase transition and a pressure-driven QCP. While experimental investigations of callaghanite under pressure are not yet available, it definitely represents a very interesting model compound for studying the subtle balance of AFM and FM interactions close to compensation. A similar network of dimers is also present in the mineral liroconite, $\text{Cu}_2\text{Al}(\text{AsO}_4)(\text{OH})_4 \cdot 4\text{H}_2\text{O}$ [90], which would deserve a similarly detailed investigation.

2.4. Urusovite: Corrugated honeycomb planes prone to dimerization

A layered structure consisting of corrugated honeycomb layers is realized in the rare copper-aluminium-arsenate mineral urusovite, $\text{CuAl}(\text{AsO}_4)\text{O}$, discovered about 20 years ago on Kamchatka [91, 92]. Its crystal structure is monoclinic, with the space group $P2_1/c$. Synthetic powders of this

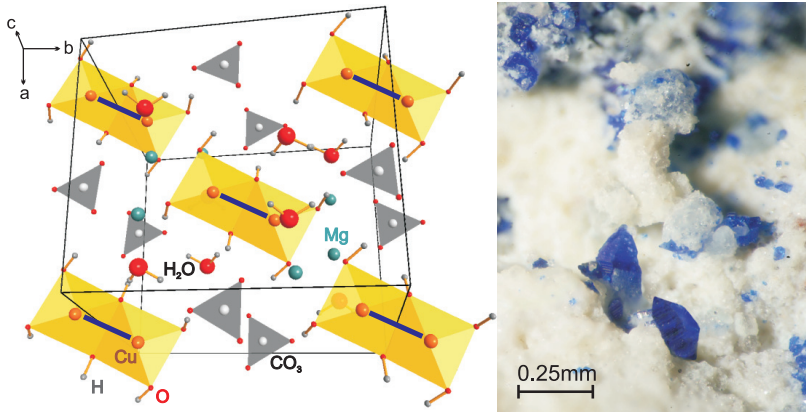


Figure 4. The dimer structure of callaghanite (left) and a photo of natural callaghanite crystals (right). Reproduced with permission from Ref. [88], copyright by the American Physical Society.

compound were recently investigated by magnetization, specific heat, and electron spin resonance (ESR) [93], showing a spin-gap behavior with a gap of about 30 meV. Analysis of the exchange constants derived from DFT calculations revealed that this gap is due to a strong dimerization on one of the bonds in the distorted honeycomb plane. The dominant edge-shared superexchange interaction $J_1 \approx 30$ meV on one of the bonds is mediated by two Cu–O–Cu paths with a bond angle of 102.6° . The corner-shared superexchange paths on two other bonds have a notably larger bond angle of 111.3° , but despite that have a vanishingly small exchange constant $J_2 \approx 0.05$ meV, which is even weaker than the interlayer super-superexchange $J_3 \approx 0.7$ meV. It has been therefore concluded that urusovite realizes a model of very weakly interacting spin dimers with a valence-bond solid (VBS) ground state, schematically depicted in Fig. 5. At elevated temperatures, thermal expansion leads to a gradual modification of the bond angles and, consequently, to a substantial increase in the in-plane exchange parameters. These thermal effects were claimed responsible for the observed deviations of the high-temperature experimental data from the predictions of a simple weakly interacting dimer model [93].

Naturally, the lowest-energy excitation in CuAl(AsO₄)O, observed by ESR, corresponds to the singlet-triplet transition with an energy given by the spin gap, $\Delta \approx 30$ meV. The average effective *g* factor was found to be $g = 2.05$ and remained constant down to ~ 90 K, shifting afterwards to higher values. The latter artefact has been ascribed to paramagnetic impurities, which were also evidenced by the static magnetic susceptibility measurements [93]. Estimates of the *g*-factor anisotropy from the parallel and perpendicular components of the hyperfine structure resulted in the value for $(g_{\parallel} - g_{\perp})/g_{\perp} \approx 0.17$.

2.5. Clinoclase: Nonequivalent dimers with two energy scales

Another example of a system with weakly coupled magnetic dimers is clinoclase, Cu₃(AsO₄)(OH)₃, whose magnetic properties also lack in-depth experimental investigations to date. X-ray structural refinement [94, 95] revealed an intricate structure with the monoclinic $P2_1/c$ space group, in which Cu²⁺ ions occupy three inequivalent Wyckoff positions: Cu(1) and Cu(3) have strongly distorted octahedral coordinations approaching square pyramidal, while Cu(2) is coordinated by 5 anions only [95]. These spin- $\frac{1}{2}$ ions are arranged into two types of structural dimers, Cu(1)–Cu(2) and Cu(3)–Cu(3), which are both built of two edge-sharing CuO₄ plaquettes, but with different geometrical parameters and, consequently, different Cu–O–Cu bridging angles. The Cu(1)–Cu(2) dimers share corners and form zigzag chains along the [001] direction, connected by AsO₄ tetrahedra into layers parallel to the *bc* plane, with Cu(3)–Cu(3) dimers sandwiched in between these layers. According to the DFT+*U* calculations within the local spin-density approximation

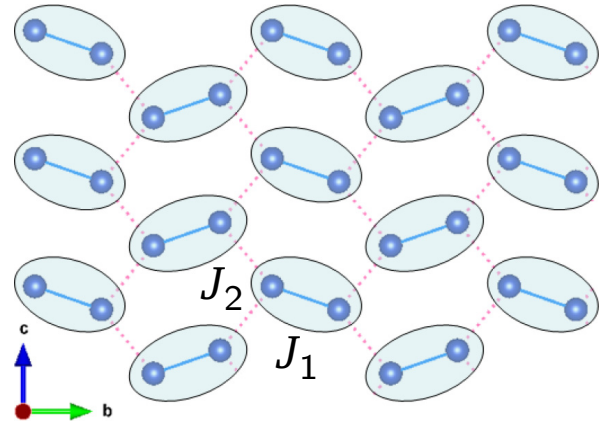


Figure 5. Schematic depiction of the VBS ground state in urusovite. Reproduced with permission from Ref. [93]. Copyright by the American Physical Society.

(LSDA+ U) by Lebernegg *et al.* [96], this complex structure hosts four AFM exchanges that exceed 100 K, of which the two leading interactions operate between the Cu(1)–Cu(2) dimers ($J \approx 700$ K) and within the Cu(3)–Cu(3) dimers ($J_{D2} \approx 300$ K). This situation implies that the spin dimer with the strongest interaction J does not coincide with any of the structural dimers, but acts between the corner-sharing CuO_4 plaquettes that have a much larger Cu–O–Cu bridging angle of 150°. The interaction within the Cu(1)–Cu(2) dimer (J_{D1}) is nearly compensated because of the much smaller Cu–O–Cu bridging angle < 100°, in agreement with the GKA rules. At the same time, contrary to the GKA rules, the second-leading interaction J_{D2} is nearly twice larger than the interaction between the Cu(3)–Cu(3) dimers despite the smaller bridging angle. As a result, the authors of Ref. [96] arrive at the planar network of magnetic interactions in clinoclase that is presented in Fig. 6. It contains two types of AFM dimers defined by the leading exchange terms J and J_{D2} , connected by weaker nonfrustrated AFM exchange paths $J_{\text{id}1}$ and $J_{\text{id}2}$, both of about 160 K.

Susceptibility measurements performed on natural clinoclase crystals [96] show perfect agreement with the output of theoretical calculations summarized above. An attempt to fit the data with a single dimer contribution clearly fails, but they can be perfectly described with the “2+1” dimer model in which strong and weak dimers are included in the 2:1 ratio as in Fig. 6. The experimentally determined intradimer exchange constants of $J_1 = 703.5$ K and $J_2 = 289.3$ K perfectly match with the J and J_{D2} values resulting from the DFT+ U calculation. The inclusion of interdimer interactions in the framework of a Quantum Monte Carlo (QMC) simulation leads to no observable changes in the susceptibility.

The presence of weakly interacting nonequivalent spin dimers in clinoclase implies that its spin-excitation spectrum should consist of two gapped branches of triplet excitations similar to those observed in the prototypical coupled-dimer antiferromagnets KCuCl_3 or TlCuCl_3 [62–64], with characteristic energy scales $J_{1,2}$ that correspond to singlet-triplet transitions of both dimers [65]. The dispersion of triplet excitations, and consequently their spin gaps, would sensitively depend on interdimer interactions. Each of these triply degenerate excitations would then split into three branches in an external magnetic field [66, 67], possibly leading to a field-tuned QCP via the Bose-Einstein condensation of the triplet states [68]. Further, sufficiently strong interdimer interactions may lead to a field-dependent hybridization of propagating triplet excitations from different dimers that would represent an interesting topic for future spectroscopic studies.

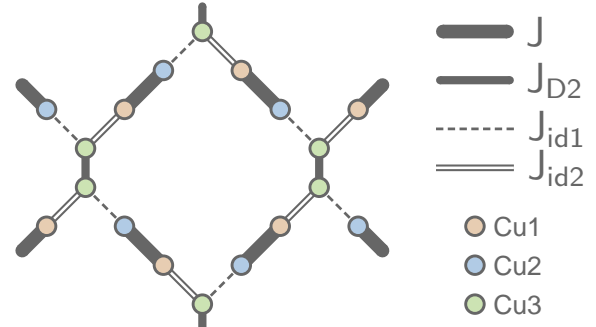


Figure 6. The planar network of exchange interactions in clinoclase. Intra- and interdimer interactions are shown with thick and thin lines, respectively. Reproduced with permission from Ref. [96], copyright by the American Physical Society.

3. Quantum spin chains

3.1. The assortment of spin chains and ladders

Quantum spin chain and ladder models [97, 98] serve for the description of magnetism in a variety of quasi-1D systems that commonly occur in minerals. Of our primary interest are lattice configurations with magnetic frustration realized via the competition of nearest- and further-neighbor exchange interactions. The simplest model of this kind is a uniform spin- $\frac{1}{2}$ chain with a FM nearest-neighbor (NN) coupling $J_1 < 0$ and AFM next-nearest-neighbor (NNN) coupling $J_2 > 0$, which is relevant for the minerals tolbachite (CuCl_2), trippkeite (CuAs_2O_4), linarite ($\text{PbCuSO}_4(\text{OH})_2$), and szenicsite ($\text{Cu}_3(\text{MoO}_4)(\text{OH})_4$) as well as for a number of archetypal low-dimensional cuprates CuBr_2 [99–101], Li_2CuO_2 [102–106], LiCu_2O_2 [107–110], NaCu_2O_2 [111], LiCuVO_4 [112–116], LiCuSbO_4 [117], and $\text{Li}_2\text{ZrCuO}_4$ [118, 119], composed of edge-sharing copper-oxygen chains. The ground state of such a chain depends on the level of frustration that is uniquely determined by the ratio $\alpha = J_2/|J_1|$. In the isotropic exchange case, for $0 < \alpha < 1/4$ a FM ground state occurs, whereas for $\alpha > 1/4$ various exotic quantum states including a chiral nematic spin liquid [121] and a VBS with a hidden topological order [122] have been predicted. In a magnetic field, the lowest-lying excitations represent multimagnon bound states that are subject to Bose-Einstein condensation and may lead to fancy types of quasi-long-range order (nematic, antiferrotriatic, etc.) and novel Tomonaga-Luttinger liquids with multipolar spin correlations [123–125]. The resulting phase diagram in Fig. 7 that was famously presented by Sudan, Lüscher, and Läuchli [120] highlights the sequence of spin-multipolar Luttinger liquid phases (quadrupolar, octupolar, hexadecupolar, etc.) in dependence on the frustration ratio α and the magnetic field. The inclusion of interchain interactions into the model, which cannot be fully excluded in any real material, stabilizes an incommensurate spin-spiral order that is experimentally found in many of the mentioned compounds. The pitch angle of the spiral therefore provides a sensitive measure of the weak interchain interactions, ever more so in the proximity to the QCP at $\alpha = 1/4$ [126].

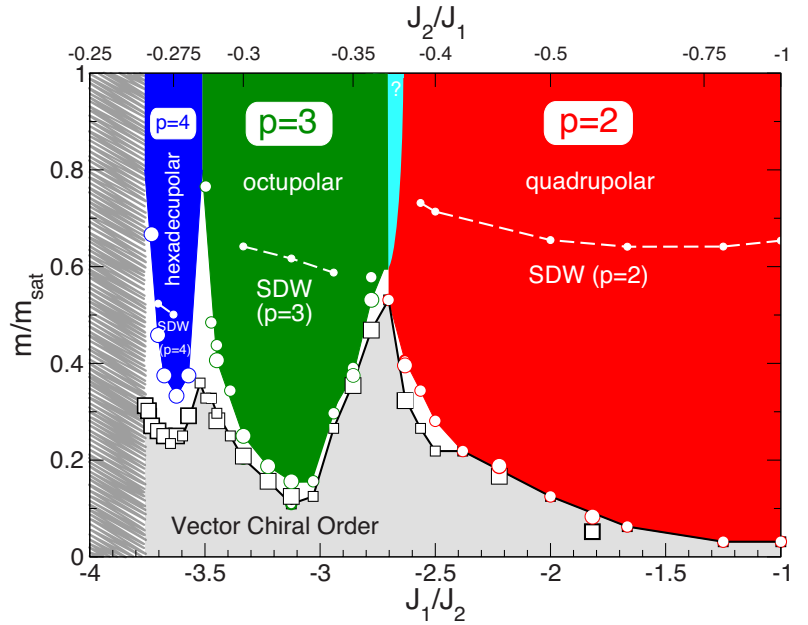


Figure 7. Numerical phase diagram for the frustrated FM spin chain with AFM second-nearest-neighbor interactions. The vertical axis represents the field-induced magnetization normalized to its saturation value. The colored regions denote spin-multipolar Luttinger liquids of multimagnon bound states composed of $p = 2, 3, 4$ spin flips. Below the dashed crossover lines, spin-density-wave (SDW) correlations start to dominate. Reproduced from Ref. [120], copyright by the American Physical Society.

The inclusion of interchain interactions into the model, which cannot be fully excluded in any real material, stabilizes an incommensurate spin-spiral order that is experimentally found in many of the mentioned compounds. The pitch angle of the spiral therefore provides a sensitive measure of the weak interchain interactions, ever more so in the proximity to the QCP at $\alpha = 1/4$ [126].

Magnetic 1D chains with higher values of the local spin can also be found in some Mn- and Fe-based minerals. For example, the borate mineral gaudefroyite, $\text{Ca}_4(\text{MnO})_3(\text{BO}_3)_3\text{CO}_3$, features ferromagnetic linear chains of edge-shared MnO_6 octahedra along [001] that are arranged on a kagomé lattice in the ab plane [127, 128]. These chains can be described by the classical Heisenberg model with a small single-ion anisotropy [129], whereas the AFM coupling between the chains leads to geometric frustration, resulting in a macroscopic ground-state degeneracy and a suppression of long-range magnetic order. It was recently realized that gaudefroyite also has remarkable low-field magnetocaloric properties and could be suitable for refrigeration applications such as liquefaction of hydrogen [130]. These studies have been performed on natural mineral samples, because the synthesis of gaudefroyite even in polycrystalline form represents a challenge due to the presence of the carbonate group that decomposes at high temperatures.

The next level in the hierarchy of simple 1D spin systems is represented by decorated spin chains, where more complicated structural units are inserted in the 1D arrangement. The dimer-plaquette chain [133], its special case the orthogonal-dimer spin chain [134, 135], and the dimer-monomer (diamond) chain [131, 132] can be ascribed to this class of models [see Fig. 8 (a–c)]. The symmetric diamond chain obtained by setting $J_1 = J_3$ is a limiting case of the more general distorted diamond chain model illustrated in Fig. 8 (c) [131], which is relevant for the copper-carbonate mineral azurite. For a symmetric spin- $\frac{1}{2}$ chain, three distinct ground states have been identified by Takano, Kubo and Sakamoto [132] as a function of the parameter $\lambda = J_2/J_1$, namely the ferrimagnetic (FRI) state for negative or positive but small $\lambda < 0.909$, the tetramer-dimer (TD) state for $0.909 < \lambda < 2$, and the dimer-monomer (DM) state for $\lambda > 2$. These states are shown schematically in Fig. 8 (d–f). The dimer-monomer state, representing a kind of spin fluid,

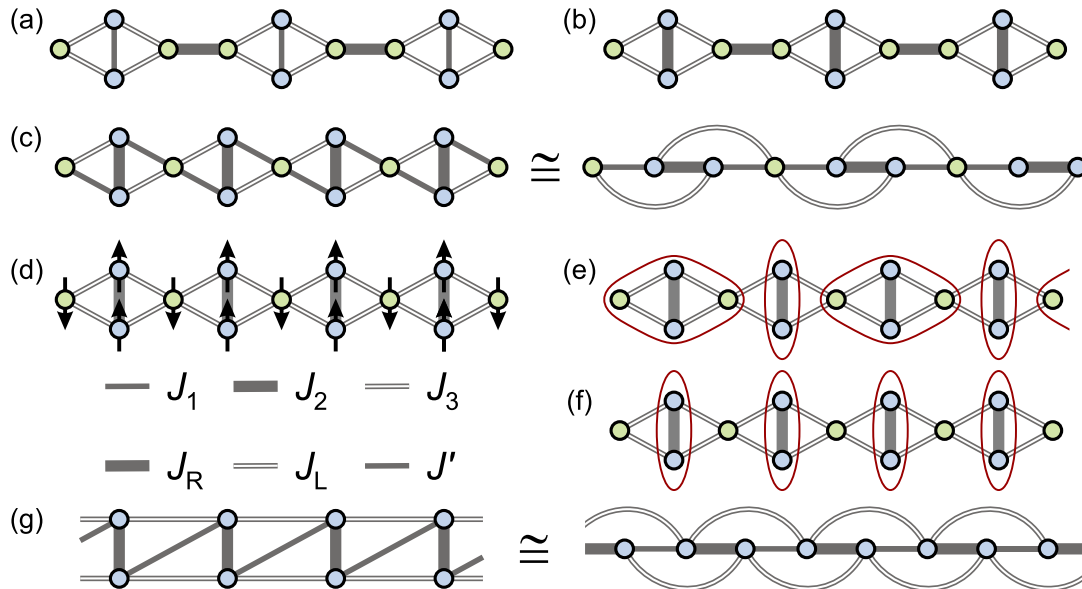


Figure 8. Examples of decorated spin-chain models: (a) dimer-plaquette chain; (b) orthogonal-dimer chain; (c) distorted diamond chain and its equivalent representation as a trimerized linear chain with NNN exchange [131]. (d–f) The three ground states of the symmetric diamond chain after Takano, Kubo and Sakamoto [132]: ferrimagnetic (d), tetramer-dimer (e), and dimer-monomer (f). (g) Zigzag spin ladder and its equivalent representation as an alternating chain with NNN exchange.

is further stabilized by the increased asymmetry between the J_1 and J_3 interactions [131], as seen in the phase diagram in Fig. 14 (b). It is believed to be realized in azurite and in the structurally related compound $\text{Bi}_4\text{Cu}_3\text{V}_2\text{O}_{14}$ [136, 137] above their corresponding 3D ordering temperatures.

Two or more coupled spin chains form a spin ladder, which takes an intermediate position between 1D and 2D spin systems. The principal difference between a solitary spin- $\frac{1}{2}$ chain and a spin ladder is that a spin- $\frac{1}{2}$ ladder with AFM couplings is a spin liquid with a singlet ground state, exhibiting a Haldane-type energy gap due to the dimerization of half-integer spins [138]. It therefore displays the characteristic properties of an integer-spin chain. The same result can be generalized to any half-odd-integer spin ladder with an even number of legs [139]. The simplest spin ladder is governed by only “rung” (J_R) and “leg” (J_L) exchange interactions. This model can be further generalized by considering additional exchange paths as in the case of a zigzag spin ladder, which is supplemented by a diagonal exchange J' between the opposite spins on the neighboring rungs [97]. It can be alternatively viewed as an alternating Heisenberg chain with NNN interactions, as shown in Fig. 8 (g). Along the $J_R = J'$ line, this model reduces to the well-studied uniform Heisenberg chain with NN and NNN interactions, which undergoes a quantum phase transition to the gapped twofold-degenerate dimer-crystal ground state at $J_L/J_R = \alpha_c = 0.2411$. In this regime, one finds the Majumdar-Ghosh point at $J_L/J_R = 1/2$, where the two degenerate ground states can be factorized into a product of singlets formed on NN dimers [140]. By including alternation ($J_R \neq J'$), the degeneracy is removed, but one of the Majumdar-Ghosh states remains the exact ground state of the system along the so-called Shastry-Sutherland lines, $J_L = \frac{1}{2} \min(J_R, J')$ [97, 141]. It was recently realized that the proximity to the Majumdar-Ghosh point, which requires a delicate balance among the exchange parameters, is an essential ingredient of the effective model for the copper-molybdate mineral szenicsite [142].

3.2. Tolbachite: Cycloidal helimagnet with field-driven ferroelectricity

The mineral tolbachite, or anhydrous cupric chloride CuCl_2 , forms brown to golden-brown monoclinic crystals characterized by the space group $C2/m$ [143, 144]. The mineral is unstable in air as it readily absorbs water, becoming hydrated to eriochalcite, $\text{CuCl}_2 \cdot 2\text{H}_2\text{O}$. Its crystal structure contains corrugated sheets of Jahn-Teller distorted $\text{Cu}^{2+}\text{Cl}_6$ octahedra, bonded by weak Van der Waals forces (see Fig. 9). This effectively results in a chemically simple quasi-1D AFM spin- $\frac{1}{2}$ quantum chain system. According to neutron powder and single-crystal diffraction, anhydrous CuCl_2 orders magnetically below a Néel temperature of $T_N = 23.9$ K, forming an incommensurate cycloidal spin-spiral structure [145, 146]. This spiral propagates along the chains (b axis), while the magnetic moments are confined in the bc crystallographic plane, so that the angle between the neighboring moments along the b direction constitutes approximately 81° .

According to DFT calculations [146, 147], the spin spiral results from competing ferromagnetic NN and antiferromagnetic NNN interactions along the spin chains, causing multiferroic behavior. The frustration ratio $\alpha = J_2/|J_1|$ varies between 1.3 and 1.8, depending on the value of U assumed in the GGA+ U calculations [146]. In other words, the NNN antiferromagnetic spin-exchange coupling dominates. Schmitt *et al.* [147] additionally considered the role of crystal water in $\text{CuCl}_2 \cdot 2\text{H}_2\text{O}$ as compared to anhydrous CuCl_2 and showed that it leads to a dramatic change in

magnetic behavior. Eriochalcite was known as a 3D antiferromagnet [148, 149], which can be explained by the relative orientation of the isolated CuCl_2O_2 plaquettes. The loss of water leads to a switch of the magnetically active orbital, thereby causing a dramatic change in magnetic properties between both compounds.

Soon afterwards, the multiferroic properties of CuCl_2 were experimentally investigated by Seki *et al.* [150]. They found ferroelectric polarization emerging along the c axis that sensitively depends on the external magnetic field. For a magnetic field applied along the b axis, a spin-flop transition occurs around 4 T that flips the magnetic moments forming the spiral into the ac plane, resulting in a simultaneous suppression of ferroelectricity. For magnetic fields orthogonal to the b axis, the spin-spiral plane depends on the field direction, and the associated polarization shows a continuous dependence on the field angle. This complex magnetoelectric behavior could be successfully explained using the inverse Dzyaloshinskii-Moriya (IDM) model [151–154], demonstrating that it is applicable even to quantum-spin systems in spite of strong quantum fluctuations. A more recent theoretical work by Tolédano *et al.* [101] analyzed the magnetoelectric effects observed in CuCl_2 and CuBr_2 and worked out their phase diagram in zero and applied magnetic fields. Contrary to the conclusions of Seki *et al.* [150], they suggested that the emergence of ferroelectric polarization is only partly due to DMI, but otherwise results from two distinct AFM spin-density wave order parameters which lead, across a first-order transition, to an incommensurate polar phase with a typical improper ferroelectric behavior.

3.3. Trippkeite: A linear-chain ferromagnet close to criticality

The greenish-blue mineral trippkeite, CuAs_2O_4 , crystallizing in the tetragonal space group $P4_2/mbc$ [155] as shown in Fig. 10, represents another realization of FM spin- $\frac{1}{2}$ chains with frustrated interactions. However, in contrast to tolbachite, where the antiferromagnetic NNN interactions dominate ($\alpha \approx 1.5$), trippkeite is characterized by a small value of the frustration parameter $\alpha \approx 0.24$ and orders ferromagnetically at $T_C \approx 7.4$ K under ambient pressure [156, 157]. It therefore represents a rare example of a FM spin chain close to the QCP at $\alpha_c = 1/4$. As already mentioned above, the ground state of the system in this regime sensitively depends on the weak interchain interactions. In other nearly critical spin-chain systems with similar values of α , such as $\text{Ca}_2\text{Y}_2\text{Cu}_5\text{O}_{10}$ ($\alpha \approx 0.19$) [158] and Li_2CuO_2 ($\alpha \approx 0.33$) [104, 106], the interchain interactions enforce an antiparallel alignment of the spins, resulting in a long-range AFM ordering. In this respect, trippkeite represents an exceptional (and so far possibly unique) case, where the theoretically expected FM ground state for $\alpha < 1/4$ is actually realized [156].

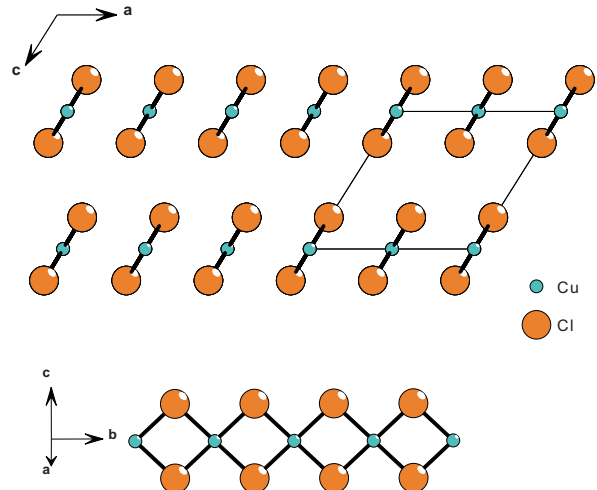


Figure 9. The crystal structure of anhydrous cupric chloride CuCl_2 (tolbachite), featuring one-dimensional frustrated spin chains. Reproduced from Ref. [146], copyright by the American Physical Society.

From measurements of the magnetization, magnetic susceptibility, and electron paramagnetic resonance, a positive Curie-Weiss temperature of $\Theta_{\text{CW}} \approx 40$ K (consistent with the predominantly FM exchange interactions) and a saturated ordered moment of $\sim 1 \mu_B$ have been estimated. Initial measurements under hydrostatic pressure have indicated an increase in the Curie temperature with a rate of 1.35 K/GPa, with no evidence for pressure-induced phase transitions up to 1.2 GPa [156]. However, in a follow-up work, Caslin *et al.* [157] extended their measurements up to 11.5 GPa and detected a structural phase transition at 9.2 GPa into the lower-symmetry tetragonal space group $P\bar{4}2_1c$, associated with an increased twisting in the CuO_2 ribbon chains and accompanied by a large drop in T_C . These changes result from the suppression of the axial Jahn-Teller elongations of the CuO_6 octahedra. According to DFT calculations, the high-pressure phase is actually characterized by a stronger ferromagnetic NN interaction and a reduced frustration ratio of $\alpha \approx 0.17$. Therefore, the drop in T_C cannot be explained within the J_1 - J_2 model only and is most probably associated with subtle changes in the interchain or further-neighbor interactions.

3.4. Linarite: Frustrated spin chains with helimagnetic order

The translucent blue mineral linarite ($\text{PbCuSO}_4(\text{OH})_2$, space group $P2_1/m$) is arguably the most studied natural quantum magnetic system, and for a good reason. The high degree of frustration in this system is evidenced by the large ratio of the Curie-Weiss and Néel temperatures, $\Theta_{\text{CW}}/T_N \approx 10$ [159]. The first studies of linarite's magnetic and thermodynamic behavior at low temperatures date back to the early 2000's [160, 161]. Its monoclinic crystal structure contains magnetically frustrated buckled CuO_2 ribbons controlled by the leading FM nearest-neighbor interaction J_1 and subleading AFM next-nearest-neighbor exchange J_2 (see Fig. 11), while the interchain interaction J_{ic} is at least one order of magnitude weaker than J_1 [159, 162, 163]. In linarite, the ratio $\alpha = J_2/|J_1| \approx 0.27-0.37$ (depending on the source and measurement method [163, 164]) is close to the QCP at $\alpha_c = 1/4$, where in an isolated spin chain the FM interaction takes over and leads to a fully polarized ground state. Consequently, the saturation field is below 10 T, and the entire magnetic phase diagram of linarite is easily accessible with many experimental probes [165-168].

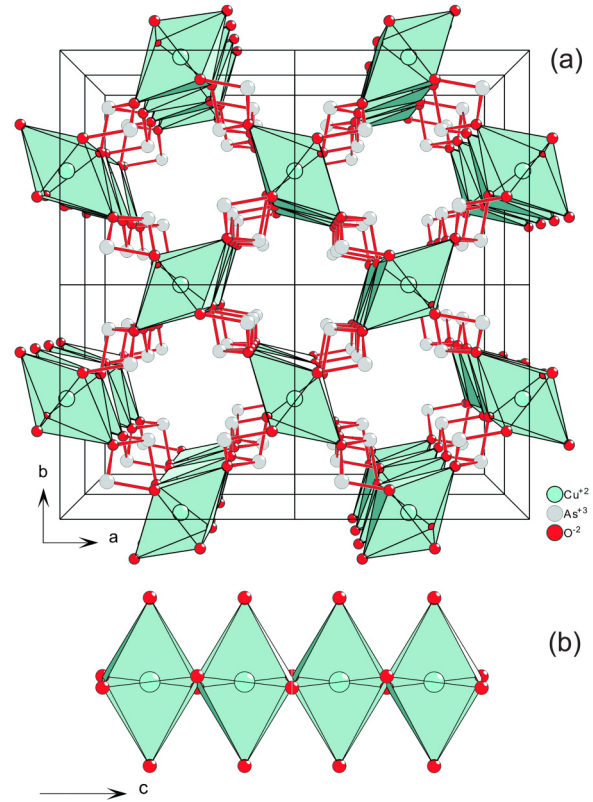


Figure 10. (a) The crystal structure of CuAs_2O_4 (trippkeite), viewed along the c axis. (b) Fragment of a spin chain consisting of edge-sharing CuO_6 octahedra. Reproduced from Ref. [156], copyright by the American Physical Society.

The frustration among J_1 and J_2 leads to a long-range elliptical-spiral ordering below the Néel temperature $T_N = 2.8$ K, which causes electric polarization of the lattice and leads to a ferroelectric behavior [169, 170] manifested in signatures of T_N in the dielectric constant, electric polarizability, and the pyroelectric and magnetoelectric current measurements [168]. Several other multiferroic phases can be stabilized in linarite by the application of magnetic field, resulting in the rich phase diagram depicted in Fig. 12. The distinct thermodynamic phases are represented here by the elliptical spiral (I), a circular helix coexisting with collinear ordering (III), a collinear Néel AFM phase (IV), and a spin-density wave (V) [167]. The small pocket of phase II is supposedly a metastable mixture of phases I and IV.

Most recently, Y. Feng *et al.* [171] also investigated the phase diagram of linarite in tilted magnetic fields applied at an arbitrary angle to the chain axis. According to their orientational phase diagrams, the spiral phase I is nearly isotropic with respect to the field direction. The high-field SDW phase V is also robust against deviations of the field directions away from the b axis. However, the Néel phase IV is destabilized at moderate deflection angles, giving way to a new conical phase that exists in magnetic fields applied perpendicular to the chains.

Recent INS measurements of spin dynamics in linarite [163] have revealed spin-wave excitations below 1.5 meV, dispersing both parallel and perpendicular to the chain direction as shown here in Fig. 13. The low-energy spin-wave branches emanate from the incommensurate (0.0.186 0.5) wave vector that corresponds to the elliptical helical order of phase I established from earlier neutron diffraction data [165]. The presence of dispersion in the direction orthogonal to the chains emphasizes the importance of interchain coupling J_{ic} . How-

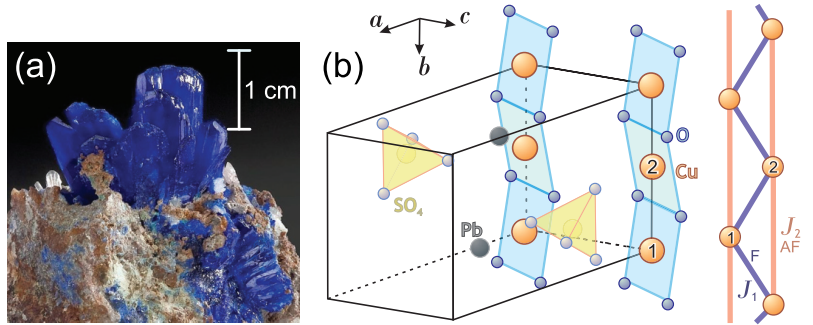


Figure 11. (a) The photographic image of large linarite crystals reproduced with permission from Ref. [166]. (b) The crystal structure of linarite (hydrogen atoms are omitted for clarity) and the diagram of two intrachain interactions: ferromagnetic J_1 and antiferromagnetic J_2 . Reproduced from Ref. [168], copyright by the American Physical Society.

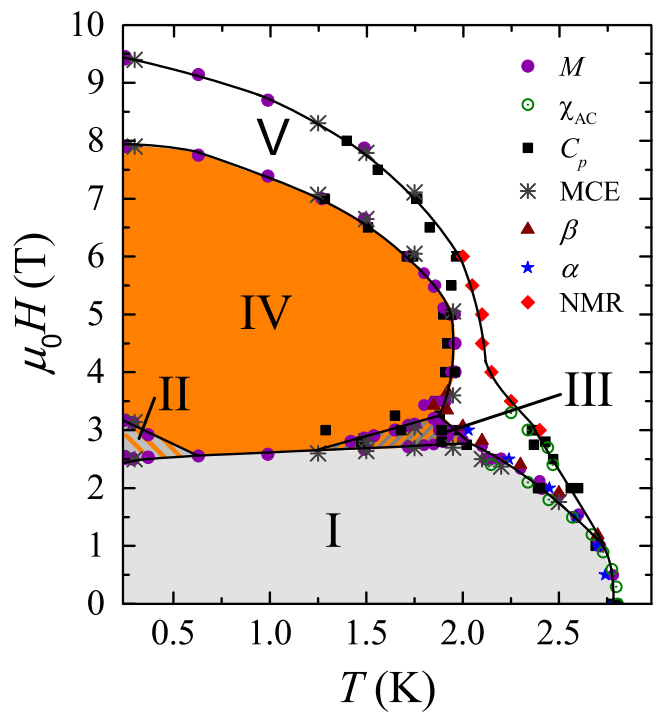


Figure 12. The magnetic phase diagram of linarite after Refs. [165–167], copyright by the American Physical Society.

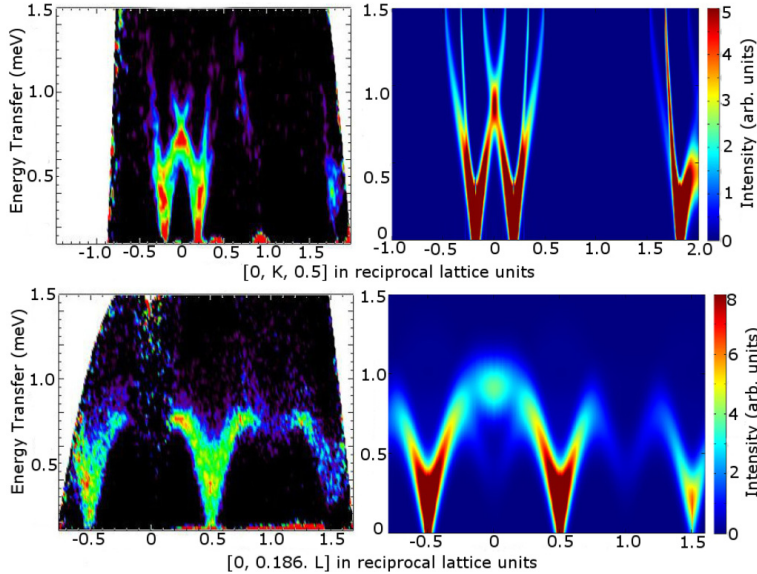


Figure 13. The measured ($T = 0.5$ K, left) and calculated (LSWT, right) magnon spectra of linarite. The figure is reproduced with permission from Ref. [163], copyright by the American Physical Society.

ever, its exact experimental value turned out to be somewhat model dependent. The comparison of INS data with calculations in the framework of linear spin-wave theory (LSWT) presented in Fig. 13 results in $J_{ic} \approx 0.34$ meV, which constitutes only 3.5% of $|J_1|$. On the other hand, a similar comparison with the dynamical density-matrix renormalization group (DDMRG) calculations performed with a 32×2 cluster yields a higher value of $J_{ic} \approx 0.6$ meV and somewhat lower value of $|J_1| \approx 6.7$ meV, thereby increasing the $J_{ic}/|J_1|$ ratio to 9%. The values reported earlier from bulk magnetic susceptibility measurements and LSDA+ U calculations [159] fall within the same range of uncertainty. The authors of Ref. [163] emphasize that the agreement between LSWT and DDMRG approaches should generally improve near the critical point at $\alpha = 1/4$ and below due to the suppression of spin fluctuations that are ignored by LSWT. As linarite falls close to this limit, LSWT can be used for a semi-quantitative analysis of the INS data.

By extending the INS measurements above the saturation field, Cemal *et al.* [164] re-evaluated the magnetic interactions in linarite, including less significant terms such as direct, diagonal, and third-nearest-neighbor interchain exchange couplings. The authors fitted globally the spin-wave dispersions measured along high-symmetry directions at elevated magnetic fields of 10, 11, and 14.5 T applied along the a axis. The resulting ratio of $J_2/|J_1| \approx 0.27$ places linarite even closer to the QCP between the FM state and spin-multipolar phases than anticipated in earlier works. This implies that despite the smallness of all interchain interactions and anisotropy terms, they can be highly relevant in suppressing the higher-order spin-multipolar quantum phases. The new data also demonstrated the sensitivity of the complex magnetic phase diagram and the ordering wave vector itself to the field direction, as entirely different phase sequences were found along the three orthogonal crystal directions [164].

3.5. Azurite: Realization of the generalized diamond-chain model

Frustrated spin chains of a different type are realized in another quantum spin system, $\text{Cu}_3(\text{CO}_3)_2(\text{OH})_2$, known as azurite. This deep-blue copper carbonate mineral, closely associated with green malachite, has a monoclinic crystal structure ($P2_1/c$ space group), and its precise

atomic positions are well known from both x-ray and neutron diffraction experiments [172–174]. The copper atoms are arranged into quasi-1D diamond chains consisting of corner-sharing rhombic plaquettes, schematically depicted in Fig. 14 (a). The chain is dimerized across the rungs that are formed by the dominant AFM exchange interaction J_2 between the nearest Cu(2) sites. Its absolute value was reported to be between 2.1 and 3.8 meV depending on the specific model or measurement method [175, 176]. The dimer-monomer interactions are given by the two nonequivalent Cu(1)–Cu(2) coupling constants $J_1 \approx 0.47J_2$ and $J_3 \approx 0.21J_2$. Further, an additional direct monomer-monomer exchange $J_4 \equiv J_m \approx 0.14J_2$ is often considered as well [175, 177]. The interchain coupling J_{\perp} is usually neglected, except in a recent neutron-scattering study where a weak anisotropic (Ising-type) interchain interaction has been claimed responsible for the multiple spin gaps observed in the magnon spectrum [178].

The symmetric diamond chain obtained by setting $J_1 = J_3$ and $J_4 = 0$ has attracted much attention from the theory side [132] as a limiting case of the more general distorted diamond chain ($J_1 \neq J_3$, $J_4 = 0$) [131]. According to the numerical phase diagram reproduced from Ref. [131] in Fig. 14 (b), the exchange parameters of azurite [175] would place it within the region corresponding to the DM (spin fluid) state above its 3D ordering temperature ($T_N = 1.9$ K). Its characteristic feature is the appearance of the 1/3-magnetization-plateau phase [179], related to the polarization of the monomers by the external magnetic field. The applicability of this model to azurite gained support, in particular, from the $^{63,65}\text{Cu}$ nuclear magnetic resonance (NMR) data [180] that indicate full polarization of the monomer spins within the plateau phase, whereas the local spin polarization of the dimers is limited to a few percent, indicating that they essentially remain in the singlet state. In azurite, the 1/3 plateau is observed in fields between $B_{c1} = 11$ T and $B_{c2} = 30$ T and is characterized by a spin gap opening at the AFM point $\mathbf{q} = (1 \frac{1}{2} 0)$. The excitations are represented by ferromagnons with an approximately cosinusoidal dispersion, originating from the interacting monomers, and a weakly dispersive Zeeman-split singlet-triplet excitation at higher energies, originating from the dimers [177]. These experimental observations at high magnetic fields are well captured by the results of exact diagonalization and DDMRG calculations [175, 176], lending further support to the dimer-monomer model.

Honecker *et al.* also presented simulations of the dynamic structure factor in zero magnetic field using DDMRG on a chain with $N = 60$ sites [176]. The spectrum consists of a gapless two-spinon continuum at

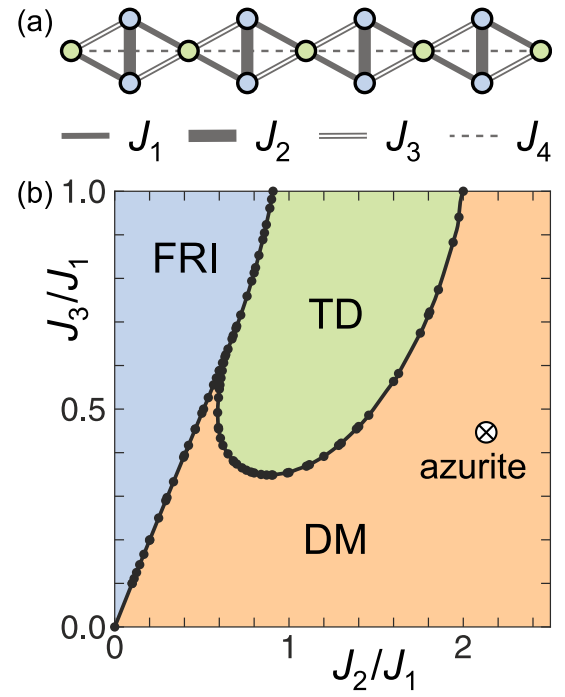


Figure 14. (a) Schematic structure of the generalized diamond chain in azurite with the most important exchange interactions. (b) The location of azurite in the numerical phase diagram of a distorted diamond chain [131] according to the exchange parameters from Ref. [175] (neglecting J_4).

low energies ($E \leq 2$ meV), well separated from a broad band of higher-energy dimer excitations, in qualitative agreement with the earlier neutron-spectroscopy data [177]. More recently, finer details of the magnetic excitation spectrum were revealed below the 3D ordering temperature, where azurite enters an AFM-ordered state. The combination of an anisotropic staggered field with a weak interchain coupling leads to the opening of two spin gaps in the spectrum, $\Delta_1 \approx 0.4$ meV and $\Delta_2 \approx 0.6$ meV. These features are not captured by the diamond-chain model and highlight the significant role of anisotropy terms and interchain interactions in the spin Hamiltonian of azurite [178]. Upon application of magnetic fields up to 7 T (which is below the critical field for the 1/3 plateau phase), the lower gap remains at its commensurate position, whereas the upper gap splits in the longitudinal direction. This effect allowed the authors of Ref. [178] to associate these two contributions with the transverse and longitudinal continua, originating from spin correlations perpendicular, $S^\perp(\mathbf{Q}, \omega)$, and parallel, $S^\parallel(\mathbf{Q}, \omega)$, to the magnetic field direction.

Application of a magnetic field also leads to very notable and rather intricate changes in the energies of the spin excitations. According to the INS data [178], reproduced here in Fig. 15, the zone-boundary mode at 1.2 meV splits into two modes at low fields with a third branch appearing above 3 T, which do not follow a Zeeman-type splitting. At the zone center, the lower gap Δ_1 shows a clear decrease in energy, while the upper gap Δ_2 remains approximately constant with field. This unusual behavior emphasizes that the character of these continuum-boundary excitations is distinct from that of conventional spin waves. The higher-energy mode corresponding to the low-lying $|\uparrow\uparrow\rangle$ triplet branch of the dimers shows a linear-in-field decrease as a function of the magnetic field for $B < B_{c1}$ due to the Zeeman effect. Above B_{c1} , within the 1/3 plateau phase, the linear slope (g factor) changes, and the mode reaches zero energy at $B_{c2} \approx 30$ T. This behavior has been observed consistently both by neutron spectroscopy [178] and by ESR [181–183].

However, more recent ESR experiments [183] identified a number of previously unknown resonances, some of which are likely responsible for the broad unresolved peaks seen earlier by neutron scattering at energies of about 4–6 meV [177]. The complexity of the ESR spectrum indicates deviations from the simple dimer-monomer model, but can be remarkably well explained by an energy-level diagram involving a ground-state doublet, an excited doublet with an energy of $\Delta_{ED} \approx 0.76$ meV (183 GHz), and an excited quadruplet state at $\Delta_{ES} \approx 4.3$ meV (1043 GHz), which undergo a Zeeman splitting in magnetic field. This led Kamenskyi [183] to propose a more elaborate model, consisting of six interacting spins forming a segment of the diamond chain, which likely constitutes the minimal backbone that is required to explain all the experimental observations.

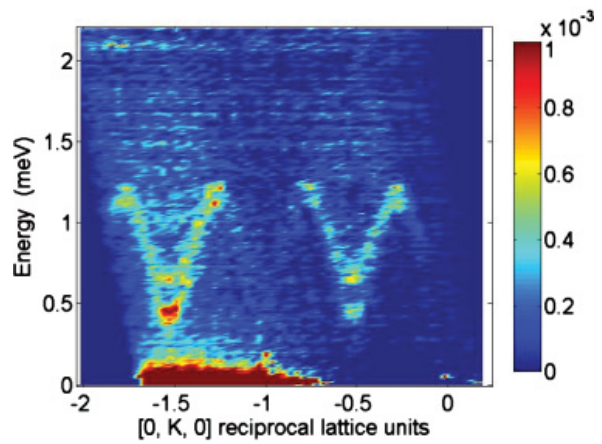


Figure 15. INS data on azurite, measured below T_N at a temperature of 60 mK, revealing two spin gaps due to the 3D interchain interactions. The figure is reproduced with permission from Ref. [178], copyright by the American Physical Society.

3.6. Euchroite: Frustrated sawtooth chains with a spin gap

The quasi-1D Heisenberg AFM spin chains found in the copper arsenate hydroxide mineral euchroite, $\text{Cu}_2(\text{AsO}_4)(\text{OH}) \cdot 3\text{H}_2\text{O}$ (orthorhombic space group $P2_12_12_1$) [184], consist of corner-sharing triangles, as shown in Fig. 16. Such structures are known as sawtooth chains (or Δ chains) and have been previously considered in relationship to the compound $\text{YC}\text{uO}_{2.5}$, derived from a delafossite-type structure by doping additional oxygen atoms that mediate AFM super-exchange interactions in the Cu plane [186–188]. In euchroite, which is essentially a hydrated analog of olivenite [189], magnetic Cu^{2+} ions are surrounded by six oxygen atoms that mediate superexchange interactions. A slight difference in the bond lengths (3.01, 3.06, and 3.17 Å) and, consequently, in the Cu–O–Cu bond angles along the sides of every unit triangle guarantees that the three exchange paths J_1 , J_2 , and J_3 are nonequivalent.

Natural samples of euchroite have been studied by magnetic susceptibility, specific heat, high-field magnetization, and ^1H -NMR measurements [185]. The susceptibility data show a maximum around 85 K, characteristic of a low-dimensional antiferromagnet, and a spin-gap behavior at low temperatures with a small upturn due to impurities. The high-temperature range can be fitted to a Curie-Weiss law with $\Theta_{\text{CW}} \approx -50$ K. The authors of Ref. [185] employed a simple spin-dimer model to extract the approximate scale of the dominant exchange constant, $J \approx 11.6$ meV, by fitting the susceptibility data. A reasonably good quality of the fit suggests that euchroite may form a singlet ground state due to dimerization. The high-field magnetization of euchroite revealed a plateau followed by a steep increase above 40 T, which can be explained by the presence of a spin gap with a magnitude of ~ 5 meV. A more accurate estimate of the spin gap could be obtained from the temperature dependence of the spin-lattice relaxation rate T_1^{-1} , fitted to an Arrhenius-type equation with an activation energy of ~ 8 meV [185]. Further details about this dimerized Δ chain system could be obtained in future high-field magnetization and spectroscopic measurements.

3.7. Fedotovite: Haldane chains of edge-shared tetrahedral spin clusters

In a recent study, Fujihala *et al.* [190] considered the magnetic properties of the sulfate mineral fedotovite, $\text{K}_2\text{Cu}_3\text{O}(\text{SO}_4)_3$. This compound forms emerald-green crystals with a monoclinic crystal structure (space group $C2/c$), in which magnetic Cu^{2+} ions are grouped by six into edge-sharing tetrahedral clusters [191]. These clusters are then connected to each other by SO_4^{2-} ions to form chains along the b axis, as shown in Fig. 17 (a,b), whereas interchain coupling along the a and c axes is negligible. The effective model of the cluster, proposed by Fujihala *et al.* [190], includes

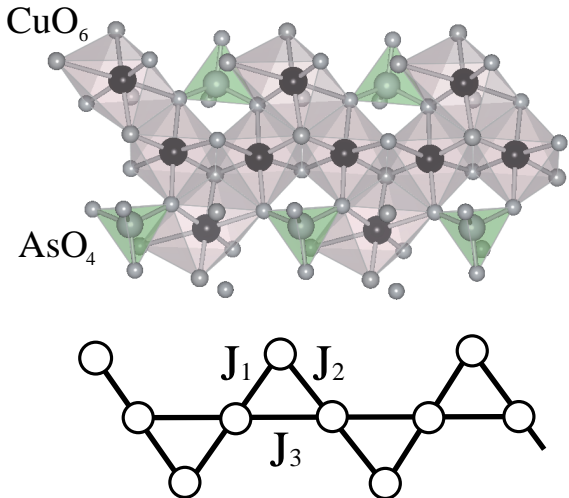


Figure 16. The crystal structure of euchroite (top) and the schematic view of the sawtooth chains with three relevant exchange interactions (bottom). Reproduced with permission from Ref. [185], copyright by IOP Publishing Ltd.

three superexchange interactions: the weakly ferromagnetic rung interaction $J_1 \approx -3$ meV, which acts between the structurally equivalent Cu sites, and two nearly equal diagonal AFM interactions $J_2 \approx J_3 \approx 10.8$ meV. These parameters result in a triplet ground state of the cluster, which has been confirmed by magnetic susceptibility and high-field magnetization measurements. The latter exhibits a $1/3$ plateau above ~ 30 T, which is small compared to the $J_2 \approx J_3$ energy scale. Consequently, an effective $S = 1$ degree of freedom can be associated with every cluster in its ground state. It is therefore expected that such clusters, connected into a 1D chain by an effective intercluster interaction J_{eff} , would realize a Haldane state by analogy with integer-spin chains or AFM spin- $\frac{1}{2}$ ladders [138, 192]. In the same work [190], the authors generalize this case to a more general situation of edge-shared tetrahedral clusters with an arbitrary number of rungs and come to the conclusion that the ground state would alternate between singlet and triplet as the number of tetrahedra is increased. Therefore, any cluster with an even number of tetrahedra (i.e. odd number of rungs) would realize a Haldane state. In this respect, fedotovite can be considered as a generalization of the $S = \frac{1}{2}$ AFM spin-ladder model, where a cluster trivially consists of a single rung.

To estimate the value of the Haldane gap, Fujihala *et al.* also measured the spin excitation spectra of a synthetic $\text{K}_2\text{Cu}_3\text{O}(\text{SO}_4)_3$ powder sample by time-of-flight neutron spectroscopy [190]. The color maps illustrating the distribution of powder-averaged INS intensity in the energy-momentum space are reproduced here in Fig. 17 (c). At low temperatures, the spectrum is fully gapped below ~ 0.6 meV ≈ 7 K, which is consistent with the value of the excitation gap of ~ 6 K that was obtained from magnetization measurements. A relatively small increase in temperature to 4 K is already sufficient to close the energy gap in the INS spectrum.

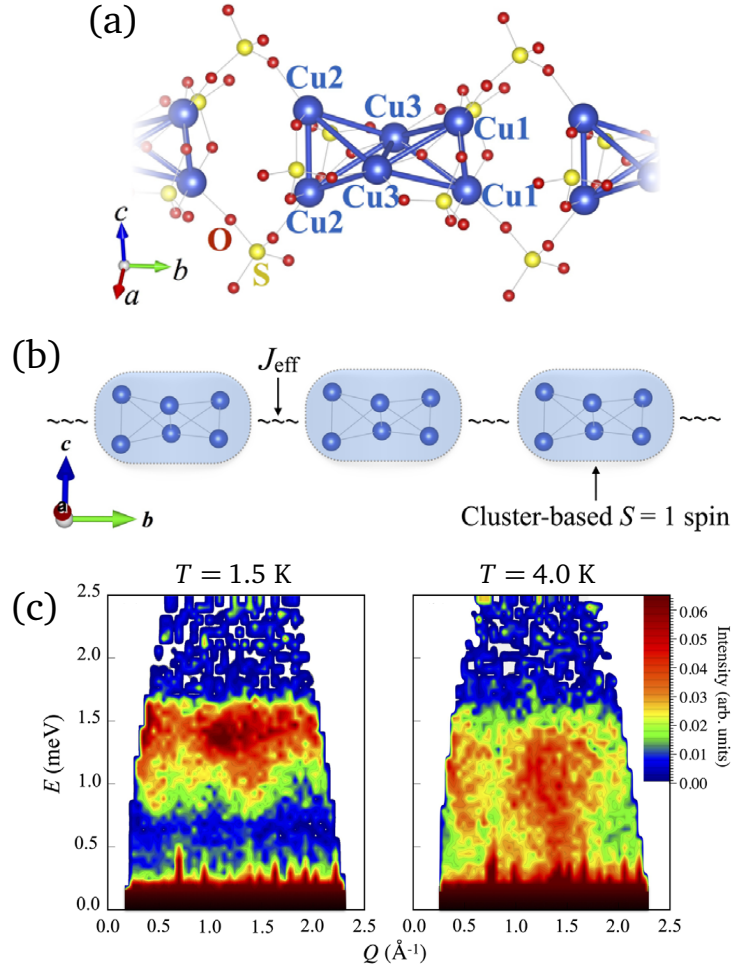


Figure 17. (a) The crystal structure of fedotovite in the vicinity of a spin cluster. (b) An effective model of the cluster-based $S = 1$ Haldane chain. (c) The INS data, measured on a synthetic powder sample of fedotovite at $T = 1.5$ K (left) and 4.0 K (right). Adapted from Ref. [190], copyright by the American Physical Society.

3.8. Dioptase: A hexagonal network of ferromagnetically coupled AFM chains

Another copper mineral that attracted recent attention is the green dioptase, $\text{Cu}_6\text{Si}_6\text{O}_{18} \cdot 6\text{H}_2\text{O}$. Its rhombohedral crystal structure, described by the $\bar{R}\bar{3}$ space group [195, 196], consists of spiral chains running along the c axis, which are arranged into closely packed 12-membered Cu rings in the ab plane, with smaller nonmagnetic beryl-type Si_6O_{18} rings located inside [see Fig. 18 (a)]. It can be therefore classified as a member of the cyclosilicate family of minerals. Despite the seemingly complicated lattice, copper ions occupy a single Wyckoff site and are therefore structurally equivalent. Magnetic interactions are represented by the stronger AFM coupling $J_1 \equiv J_c > 0$ along the chains and weaker FM coupling $J_2 \equiv J_{ab} < 0$ between the chains, as shown in Fig. 18 (b), resulting in a very elegant magnetic Hamiltonian with only one tuning parameter, $\alpha = J_2/J_1$. At the same time, there has been a lot of controversy about the values and even the sign of the interchain interaction until recently.

It has been known since the 1960s that dioptase orders antiferromagnetically at low temperatures, though the reported values of the Néel temperature, T_N , varied widely [197–201]. The magnetic structure has been reported in a number of works and is illustrated here in Fig. 18 (c). It is characterized by the ordered moment of only $0.55 \mu_B$ [201, 202], which is unusually low for a 3D antiferromagnet and can be traced back to the low connectivity of the lattice. For the anhydrous version of the same mineral, known as black dioptase, Wintenberger *et al.* proposed that the intrachain exchange interactions are AFM, $J_1 > 0$, whereas the interchain ones are FM, $J_2 < 0$, and much weaker [201]. Later, it was demonstrated using theoretical calculations that J_2 in black dioptase is weaker than J_1 by two orders of magnitude [203]. On the other hand, it was suggested that in the fully hydrated green dioptase both J_1 and J_2 are AFM and comparable [204], which would place it in the proximity of a QCP at $\alpha_c = 1.86$ that separates an AFM ordered state from a quantum spin liquid. However, recent muon spin relaxation (μSR) experiments revealed no evidence for quantum magnetic fluctuations either above or below T_N [205].

Gross and co-workers [204] parameterized the dioptase Hamiltonian with $\delta = (\alpha - 1)/(\alpha + 1)$, which is equivalent to $J_1 = J(1 - \delta)$ and $J_2 = J(1 + \delta)$ with $J > 0$, and studied the phase diagram of the resulting model in the range $-1 < \delta < 1$ by QMC simulations. They found that for sufficiently

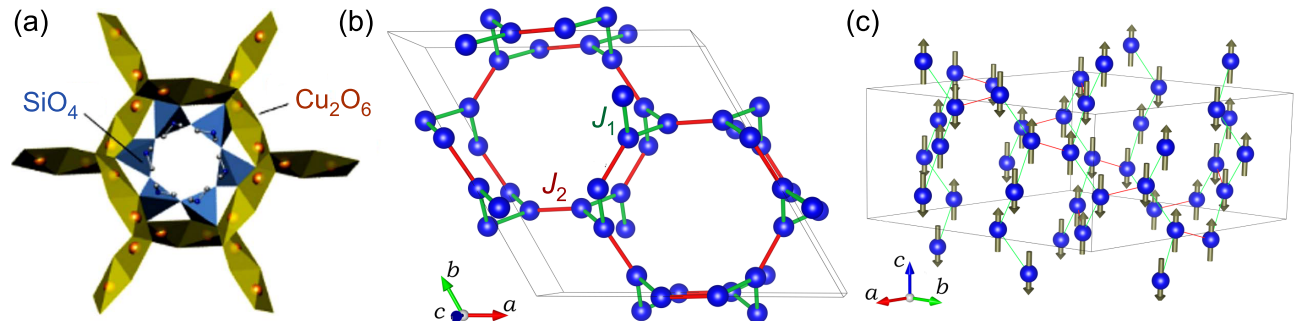


Figure 18. The crystal structure, magnetic interactions, and AFM order in green dioptase. The leading AFM coupling J_1 along the chain direction and the weaker ferromagnetic coupling J_2 between the chains are shown with green and red lines, respectively. Reproduced with permission from Refs. [193] and [194], copyright by the American Physical Society.

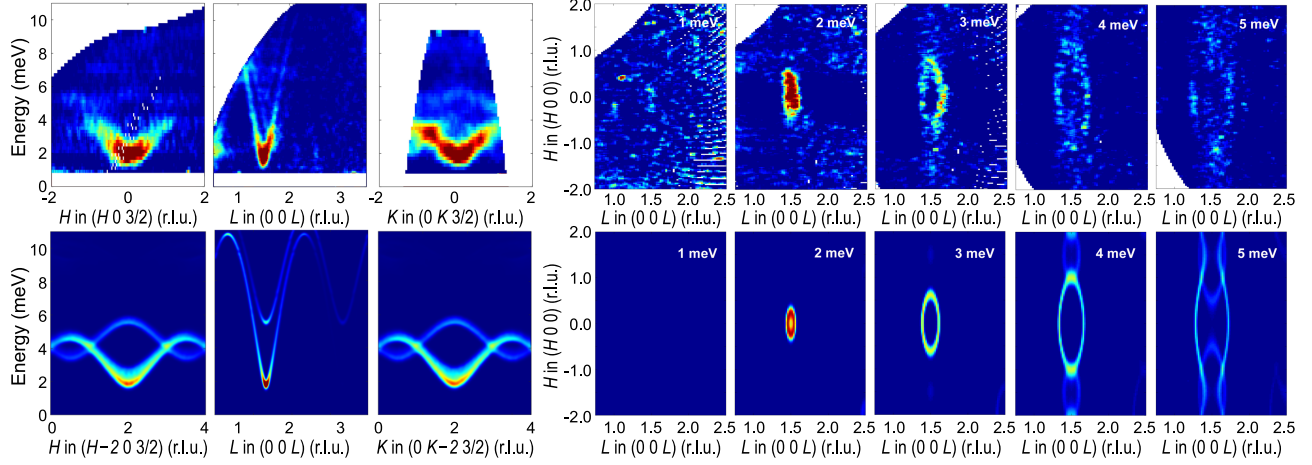


Figure 19. Selected energy-momentum (left) and constant-energy (right) cuts through the INS data measured on a natural sample of green dioptase in the AFM state at $T = 1.7$ K. The experimental data shown at the top are compared with the spin-wave model convoluted with spectrometer resolution, shown for the same cuts below each panel. Reproduced with permission from Ref. [194], copyright by the American Physical Society.

strong J_2 , namely for $\delta > 0.3$, the AFM order is destroyed due to the dimerization on the J_2 bonds, which leads to a gapped singlet-dimer state. As J_2 is reduced, the maximum of T_N is reached near $\delta \approx 0$, but upon approaching $\delta = -1$ the AFM chains become decoupled, which again leads to a suppression of long-range order according to the Mermin–Wagner theorem. Unfortunately, the region of negative δ , which would correspond to FM interchain coupling, was not explored in this work.

More recently, however, full-potential DFT calculations and neutron-spectroscopy measurements consistently demonstrated that the interchain coupling in dioptase is actually ferromagnetic. The theoretical calculations resulted in the exchange parameters $J_1 = 6.72$ and $J_2 = -3.19$ meV [193], whereas the experimental values are $J_1 = 10.6$ and $J_2 = -1.2$ meV [194]. The latter values, which correspond to $\alpha \approx -0.11$, are consistent with the observed reduction of the Néel temperature $T_N \approx 15$ K with respect to J_1 and the reduced ordered moment of $\sim 0.55 \mu_B$ [202] by quantum spin fluctuations expected in the quasi-1D system of weakly coupled chains. The ordering in dioptase could be additionally impeded by the low coordination number of the lattice [193]. The consistency between the INS data and the new model is illustrated by the comparison of the time-of-flight data with the spin-spin correlation function calculated from linear spin-wave theory [194], as shown in Fig. 19. These new results clearly exclude the scenario of an AFM interchain coupling. The uncertainty surrounding the value of interchain interactions is understandable if one considers the intradimer Cu–O–Cu bridging angle of 97.4° , which falls within the range where the FM and AFM contributions tend to compensate each other according to the GKA rules [88]. It is also worth noting that the crystal symmetry allows for DMI between the Cu spins, which have not been typically included in the models, but were claimed responsible for a broad spectral feature observed in ESR [206].

The value of the spin gap in the zero-field AFM state, estimated from the INS data, amounts to ~ 1.5 meV [194], which agrees perfectly with the zero-field AFM gap of $\Delta_{\text{AF}} = 350$ GHz

(1.45 meV) measured by ESR [206], as shown in Fig. 20. The AFM resonance in ESR has been tracked in high magnetic fields up to 35 T for fields applied both perpendicular and along the chains at $T = 4.2$ K. For $\mathbf{B} \perp \mathbf{c}$ (hard axis), the energy of the resonance monotonically increases without any notable anomalies, whereas for $\mathbf{B} \parallel \mathbf{c}$ (easy axis) it initially splits into two branches as expected for the two-sublattice AFM resonance in the presence of a uniaxial anisotropy. At a critical field of $B_{sf} = 12.5$ T, the spin gap closes as the lower branch hits zero energy, and a spin-flop transition occurs [206]. Taking into account that the spin-flop field is within the reach of most experimental probes, the high-field phase would certainly warrant a more detailed investigation by other methods, including neutron scattering, as it could help to pinpoint magnetic interactions in diopptase with higher accuracy.

3.9. Szenicsite and antlerite: Frustrated spin chains near the Majumdar-Ghosh point

Interesting physical aspects of frustrated spin chains were recently revealed in the rare copper-molybdate mineral szenicsite by Lebernegg *et al.* [142]. This system, with the chemical formula $\text{Cu}_3(\text{MoO}_4)(\text{OH})_4$, crystallizes in an orthorhombic structure described by the space group $Pnnm$, in which CuO_4 plaquettes form triple chains that are parallel to the c axis [207, 208]. In this respect, the structure resembles that of the sulfate mineral antlerite, $\text{Cu}_3(\text{SO}_4)(\text{OH})_4$, in which the edge-sharing Cu(1) central chain shows an idle-spin behavior, and only the corner-sharing Cu(2) outer chains order magnetically below $T_N \approx 5.3$ K into a collinear structure characterized by an antiparallel orientation of spins in the opposite FM aligned chains [209–211]. An isostructural synthetic compound $\text{Cu}_3(\text{SeO}_4)(\text{OH})_4$, on the other hand, stabilizes a more complex cycloidal magnetic structure among the FM chains that locks into the commensurate $(\frac{1}{7}00)$ propagation vector at low temperatures [210]. A more recent work has cast doubt on the idle-spin behavior of the central chain, and an alternative model with multiple AFM interactions between the chains was put forward [212]. Despite the structural similarities among these compounds, the magnetic behavior of szenicsite turns out to be very different, as its ground state shows no long-range magnetic order. Its central chain represents a realization of the frustrated AFM J_1 - J_2 chain model with the NN coupling $J_1 \approx 5.86$ meV and a sizable NNN coupling J_2 that is approximately twice weaker, $J_2/J_1 \approx 0.5$ [142]. It was argued that the interchain frustration essentially decouples this central chain from the two side chains that can be in turn described by AFM coupled dimers [142],

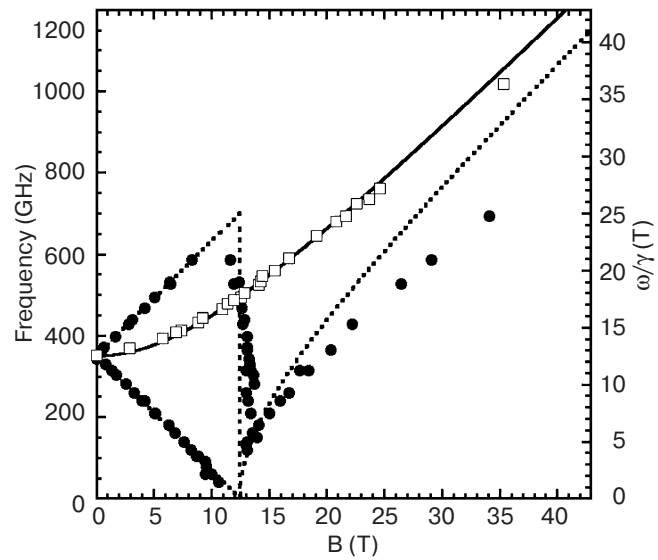


Figure 20. Low-temperature ($T = 4.2$ K) ESR data for diopptase, measured in pulsed magnetic fields applied parallel (\bullet) and perpendicular (\square) to the chains. The solid and dotted lines describe two-sublattice AFM resonances under uniaxial anisotropy for fields along the hard and easy axis, respectively. Reproduced with permission from Ref. [206], copyright by Springer-Verlag.

rather than by the uniform chain model proposed earlier [213, 214].

As discussed in section 3.1 above, the uniform AFM Heisenberg chain with NN and NNN interactions features a gapped dimer-crystal ground state for $J_2/J_1 > \alpha_c = 0.2411$, and the exchange parameters estimated for the central chain in szenicsite certainly place it within this regime. Moreover, its J_2/J_1 ratio is very close to the Majumdar-Ghosh point ($\alpha_{MG} = 0.5$), where two degenerate ground states can be exactly represented by a superposition of spin singlets [140]. A maximum observed in the specific heat divided by temperature, C_p/T , at 1.2 K is an additional indication of the szenicsite's proximity to the Majumdar-Ghosh point, pointing to an α ratio between 0.4 and 0.5 [142]. In total, the microscopic magnetic model derived in Ref. [142] from LSDA+ U calculations combined with susceptibility, high-field magnetization, and thermodynamic measurements includes 8 exchange parameters as shown in Fig. 21. Nevertheless, combining the dimer contribution (J_D) from the outer chains with the uniform-Heisenberg-chain contribution (J_1, J_2) from the inner chain is already sufficient to fit the susceptibility data [142]. Lebernegg *et al.* also analyzed the specifics of the exchange network in szenicsite and its differences as compared to antlerite, which are observed in the absence of long-range order, non-idle-spin behavior, and a large positive Curie-Weiss temperature of 68 K indicating the predominance of AFM interactions. These differences are explained mainly by the J_D and J'_D couplings in the side chains, which in the case of antlerite are both ferromagnetic [209, 212, 215]. At the same time, the interactions within the central chain in both szenicsite and antlerite are similar, and the debated idle-spin behavior (absence of an ordered moment) obtains a natural explanation as a consequence of the gapped spin-singlet state.

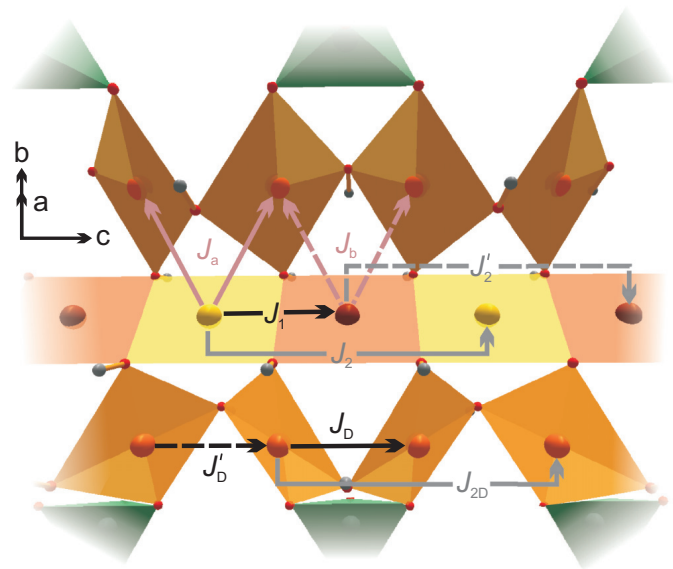


Figure 21. Exchange parameters within the triple copper-oxide chain of szenicsite. Reproduced with permission from Ref. [142], copyright by the American Physical Society.

4. Kagomé systems

4.1. The perplexing magnetism in kagomé layers

Periodic 2D arrangements (tilings) of regular polygons are exemplified by 11 uniform Archimedean lattices, which serve as prototypes of 2D interacting spin systems realized in various crystal structures [216–219]. Among them, the kagomé lattice plays an exceptional role, because it is characterized by the combination of strong frustration (as strong as in the triangular lattice) and low coordination number, $z = 4$. It is composed of corner-sharing triangles and can be obtained by a 1/4 site depletion of the triangular lattice. Along with the more exotic star lattice [220–223],

in which the triangles are additionally separated by a dimer, the Heisenberg model on a kagomé antiferromagnetic (KAFM) lattice has no semiclassical ordered ground state. It is therefore an ideal candidate for realizing a quantum-disordered state or spin liquid. In addition, it is also commonly found in minerals and a variety of crystal structures that have attracted much recent interest and has already become the subject of several dedicated review articles [55–57].

The corner-sharing geometry of KAFM layers supports an extensive classical ground-state manifold that leads to a finite residual entropy at $T = 0$. A coplanar or slightly canted spin configuration is then usually selected by the longer-range Heisenberg couplings [225–228], anti-symmetric DMI [224, 229–232], or via the order-by-disorder mechanism [233]. This classical limit is relevant, for instance, for the $AB_3(SO_4)_2(OH)_6$ jarosites, where the B^{3+} cation can be Fe^{3+} ($S = 5/2$) [231, 234] or Cr^{3+} ($S = 3/2$) [235–237]. The behavior of quantum-spin Heisenberg KAFM systems, however, still represents an open area of research, and even the exact ground state of the $S = 1/2$ Heisenberg KAFM model remains debated [238, 239]. Possible classes of solutions include valence-bond crystals (gapped) and several types of quantum spin liquids (gapped or gapless) [57]. These possible ground states are very close in energy and pose a challenge for their conclusive experimental discrimination in real materials because of the limited number of observables that are accessible in the absence of any long-range magnetic order. That's why the celebrated copper mineral herbertsmithite, $\gamma\text{-ZnCu}_3(OH)_6Cl_2$, with a number of its structural relatives hosting nearly perfect $S = 1/2$ kagomé layers [56] came into the focus of current research in quantum magnetism. Herbertsmithite was the first kagomé-layered compound to feature a perfect equilateral geometry and no order down to $T = 0$, while its metastable polymorph kapellasite with ferromagnetic NN interactions was later shown to host a gapless spin-liquid ground state due to the frustrated further-neighbor interactions [240, 241].

Such quantum-disordered ground states are generally fragile. Even in structurally perfect kagomé layers, the presence of weak magnetic anisotropy and DMI would promote 120° spin structures characterized by the “positive” (PVC), “negative” (NVC), or “staggered” (SVC) vector chirality in the classical limit [224, 232, 242]. These structures are illustrated in Fig. 22. Further, the frustration can be partially relieved by structural distortions [243–245] or disorder [246, 247], precluding a spin-liquid ground state. For instance, a low-temperature ordered state is found in volborthite, $Cu_3V_2O_7(OH)_2 \cdot 2H_2O$ [248–250], and vesignieite, $BaCu_3V_2O_8(OH)_2$ [251], which has been explained by the non-equivalent exchange on the triangles forming a distorted kagomé lattice as a result of orbital ordering [252, 253]. In this chapter, we discuss the specific behavior of various minerals realizing different magnetic models on the kagomé lattice. While most of the

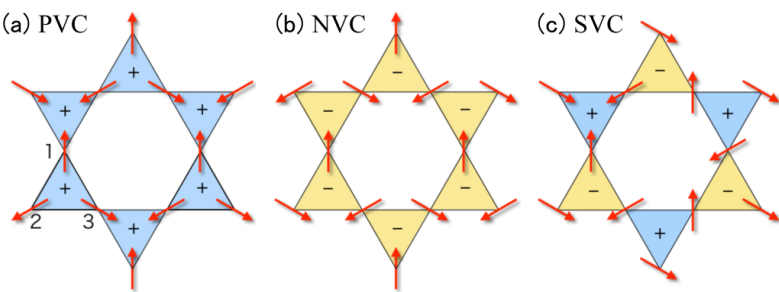


Figure 22. Possible coplanar types of magnetic order on a kagomé lattice, characterized by the positive, negative, and staggered vector chirality. The direction of the vector chirality on each triangle is shown by “+” (up) or “-” (down). Reproduced with permission from Ref. [224], copyright by the American Physical Society.

discussed compounds are found in nature and became known first as minerals, the majority of the experimental results discussed here were obtained on synthetic single crystals. This is explained by the extreme sensitivity of the observed magnetic phenomena to impurities or crystalline defects that are impossible to control in natural mineral samples, which can be in addition extremely rare or small in size.

4.2. Jarosites: Classical spins on the kagomé lattice

The jarosite family of minerals with the general formula $A\text{Fe}_3(\text{SO}_4)_2(\text{OH})_6$ (with A being an alkali metal) are model kagomé antiferromagnets with the classical spin $S = 5/2$ [55]. Their Cr and V analogues with $S = 3/2$ and $S = 1$, respectively, are also well known [235–237, 254–256]. In the naturally occurring iron jarosites, long-range Néel magnetic order is induced by the DMI that are allowed by the low symmetry of the kagomé lattice, according to the classical Monte-Carlo simulations [229–231]. These interactions, in turn, consist of two components: D_z that is orthogonal to the kagomé plane and D_p in the kagomé plane, perpendicular to the NN bonds. Their ratios to the AFM exchange coupling J between the NN spins, D_z/J and D_p/J , parameterize the magnetic phase diagram of jarosites (Fig. 23). For $D_p = 0$, the coplanar NVC and PVC magnetic structures are stabilized for $D_z < 0$ and $D_z > 0$, respectively. For finite values of D_p , the NVC structure remains coplanar, whereas the PVC structure develops an out-of-plane magnetization component and becomes weakly ferromagnetic within each layer [230], with the angle η between the moments and the kagomé plane given by $\tan(2\eta) = 2D_p/(\sqrt{3}J + D_z)$, as illustrated in Fig. 24 (a). The canted components of the magnetic moments are then stacked antiparallel to give a zero net moment in the bulk magnetic structure [236, 257].

On the experimental front, “triangular-spin AFM ordering” was first observed in a synthetic sample of K-Fe-jarosite back in the 1980’s by powder neutron diffraction, Mössbauer, and magnetic susceptibility measurements [235]. However, the exact magnetic structure, and in particular the way in which magnetic layers are stacked in the direction perpendicular to the kagomé planes remained a question of debate and was only settled much later [258, 259]. It is now established that the 120° ordering pattern of the PVC type is realized below $T_N \approx 65$ K, while the estimated Curie-Weiss temperature is $\Theta_{\text{CW}} \approx -800$ K [234, 242, 259]. Both temperatures are practically insensitive to the

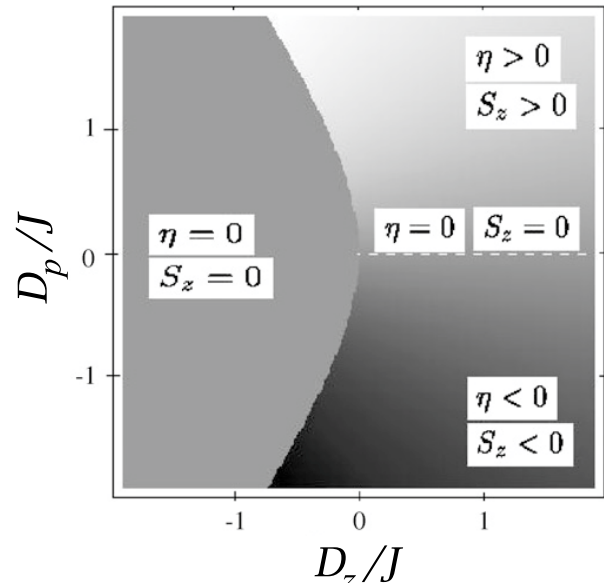


Figure 23. The mean-field phase diagram of the KAFM model with a NN Heisenberg exchange J and a DMI consisting of the in-plane (D_p) and out-of-plane (D_z) components. The gray scale represents the angle η between the magnetic moments and the kagomé plane. Reproduced from Ref. [230], copyright by WILEY-VCH Verlag GmbH.

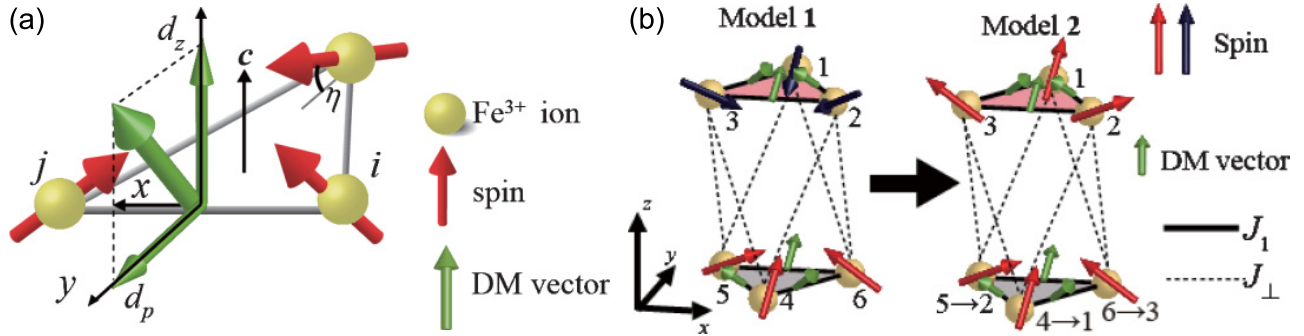


Figure 24. (a) The DMI vectors and the canted spin structure of a K-Fe-jarosite layer. (b) The change in the magnetic structure associated with the spin-flip transition of the weak FM component of the magnetic moments. Reproduced from Ref. [262], copyright by the American Physical Society.

choice of the A cation [231]. Along the c axis, the magnetic unit cell is doubled, suggesting an AFM coupling between the planes. These results are consistent with NMR measurements, which additionally provided an estimate of the spin-wave energy gap of 15 K (1.3 meV) [260]. As expected for the PVC structure, a finite field-dependent out-of-plane magnetization has been measured, resulting in the weakly noncoplanar umbellate spin structure [234]. At high magnetic fields above 16.4 T, the weak ferromagnetic spin component flips, as shown in Fig. 24 (b), causing an abrupt step in the $\mathbf{B} \parallel \mathbf{c}$ magnetization [261, 262].

The quantitative understanding of magnetic interactions in jarosite was enabled by the INS measurements performed independently by two groups in 2006. First, Matan *et al.* reported the spin-wave spectrum measured on a deuterated powder sample and a smaller (100 mg) nondeuterated synthetic single crystal of $\text{KFe}_3(\text{SO}_4)_2(\text{OH})_6$ [263]. In the powder data, they found a peak in the magnon density of states at $\hbar\omega_0 \approx 8$ meV and a second broader peak at about $2\omega_0$. Details of the spin-wave dispersion were then verified from the single-crystal measurement and could be perfectly described using a generic Hamiltonian with NN and NNN exchange terms, $J_1 = 3.18$ meV and $J_2 = 0.11$ meV, and the DMI parameters $D_z = -0.196$ meV and $|D_p| = 0.197$ meV as presented in Fig. 25. An alternative model, which attributes all of the anisotropy to the single-ion crystal field (CF model) [260], resulted in an equally good fit of the magnon dispersion along all principal directions. The strong effect of the spin canting angle due to the umbellate structure on the spin gap and the splitting of spin-wave branches at high-symmetry points enabled an accurate fit of its value to $\eta = 1.9^\circ$ within the DMI model. The weak NNN interaction J_2 was shown to be positive and responsible for the observed

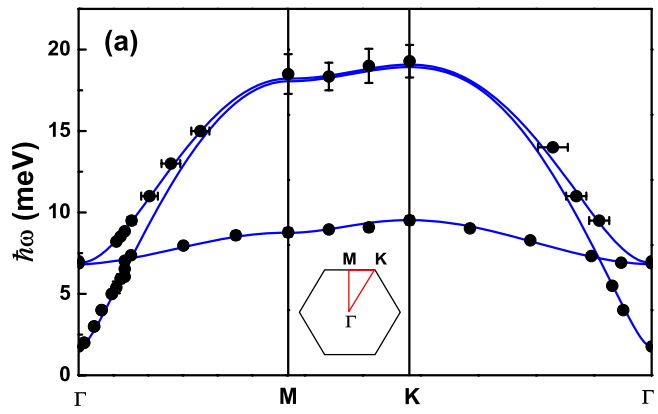


Figure 25. Spin-wave dispersion in potassium jarosite along the high-symmetry directions in the 2D Brillouin zone at $T = 10$ K. The data points from single-crystal INS measurements are fitted to the 4-parameter DMI model (solid lines). Reproduced with permission from Ref. [263], copyright by American Physical Society.

dispersion of the “flat” magnon modes. At the zone center, two spin gaps with energies $\Delta_1 = 1.8$ meV and $\Delta_2 = 6.7$ meV were observed, in reasonable agreement with the previous NMR result [260] and with the subsequent ESR measurements [262]. Motivated by these results, a much more detailed theoretical analysis that compared the spin-wave spectrum measured by Matan *et al.* with numerical calculations for a large number of model Hamiltonians with increasing complexity has been carried out by Yildirim and Harris [242]. They arrived at the slightly modified values of Hamiltonian parameters ($J_1 = 3.225$, $J_2 = 0.11$, $D_z = -0.195$, and $|D_p| = 0.218$ meV) and argued in favor of the DMI model as opposed to the CF model, as one would not expect the single-ion anisotropy D for the Fe^{3+} ion to be as high as 10% of J_1 .

Shortly afterwards, another set of INS measurements on the K-Fe-jarosite has been published by Coomer *et al.* [264]. In this work, both a natural single crystal and a synthetic deuterated powder sample have been used. The dispersion of the “flat” magnon mode in the natural mineral sample from Eureka (Utah, USA) has been identified using the high-flux IN8 triple-axis spectrometer at the Institut Laue–Langevin (Grenoble, France), which is remarkable in view of the very small sample mass of only 14.9 mg. Unfortunately, the small crystal size and the high background from hydrogen in the sample impeded a more complete mapping of other spin-wave excitations. Nevertheless, comparison with the powder data resulted in the interaction parameters that are very close to those listed above, and the results could be also described equally well by the DMI and CF models.

More recent works focused on the origin of spin anisotropy in K-Fe-jarosite, in order to distinguish the effects of single-ion anisotropy from those of DMI. The single-ion anisotropy energy could be first accurately measured using x-ray absorption spectroscopy [265], resulting in a value of $D = 0.5$ meV that is close to those obtained by Matan *et al.* (0.428 meV) and Coomer *et al.* (0.47 meV) within the CF model of Ref. [260]. This important result implies an unusually large easy-plane anisotropy of the Fe^{3+} spins, up to 15% of J_1 . Further evidence arrived from a polarized neutron-scattering study [266], which revealed an out-of-plane gap that is significantly larger than the in-plane gap, and the persistence of the out-of-plane gap above T_N . Therefore, the quasielastic scattering above T_N consists of in-plane-only spin fluctuations that are characteristic of an XY-type spin anisotropy. According to these results, K-Fe-jarosite should belong to the 2D XY universality class of magnetic systems. The debate continues, as the most recent high-field ESR results could not be reconciled with the CF model because it failed to fit the data at high frequencies [262]. The conclusion was that the DMI should still be considered as the dominant perturbation term, and to explain the spin-reorientation transition, an additional interplanar coupling term $J_\perp \approx 8.3 \cdot 10^{-3}$ meV is required. At the same time, some difficulties of the DMI model have also been emphasized.

Finally, magnetization and neutron-diffraction measurements have indicated the possible existence of a multicritical point in the magnetic field – temperature phase diagram of iron jarosites on the spin-reorientation transition line [261]. In the recent work by Freitas and Albuquerque [267], a possible interpretation of these results has been proposed. They investigated the B – T phase diagram for the XY model with DMI using the mean-field theory and suggested the existence of an additional high-field magnetic phase with a nonhelical (collinear) spin structure, forming a narrow wedge between the low- and high-field canted PVC phases. This new phase, which still awaits a

direct experimental confirmation, would persist only at low temperatures and may therefore lead to the appearance of a tricritical point.

4.3. Herbertsmithite and related $S = 1/2$ kagomé-layer antiferromagnets

Herbertsmithite, $\gamma\text{-ZnCu}_3(\text{OH})_6\text{Cl}_2$, is a copper-hydroxychloride mineral [268] that became famous in the physics community as a realization of the structurally perfect spin- $\frac{1}{2}$ kagomé antiferromagnet [269] and a likely candidate of a quantum spin liquid [56]. It derives from the mineral paratacamite, a rhombohedral polymorph of $\text{Cu}_2(\text{OH})_3\text{Cl}$ discussed in section 6.2, in which one quarter of the Cu atoms has been substituted by Zn to stabilize the rhombohedral herbertsmithite structure (space group $R\bar{3}m$) consisting of nearly decoupled undistorted kagomé planes. Although in the perfect herbertsmithite lattice zinc should go solely onto the copper intersite positions, real samples available for magnetic studies vary both in the number of zinc ions sitting on the copper kagomé sites and in the zinc deficiency on the intersites [56]. Synthetic single crystals that became recently available from the hydrothermal growth method [270, 271] may thus show deviations from the perfectly stoichiometric compositions, which are difficult to reveal using standard x-ray diffraction.

The most remarkable property of herbertsmithite is the absence of any long-range magnetic order down to the lowest measured temperatures, despite the large negative Curie-Weiss temperature of $\Theta_{\text{CW}} \approx -314\text{ K}$ [269] and the exchange energy scale of $J \approx 170\text{--}200\text{ K}$ [273–280]. This conclusion has been consistently confirmed down to millikelvin temperatures by μSR [275] and neutron scattering [276, 281], whereas measurements at elevated pressures found a pressure-driven phase transition from the quantum-disordered spin-liquid phase to a long-range ordered AFM phase with $T_N \approx 6\text{ K}$ at 2.5 GPa [282]. The absence of magnetic order at ambient pressures stimulated a considerable experimental effort and raised intense theoretical discussions regarding the true ground state of herbertsmithite—whether it is gapped or gapless, and whether the singlet valence bonds form a solid (valence bond solid, VBS) [283, 284] or fluctuate (resonating valence bonds, RVB) [285, 286]. For a long time, inadvertent magnetic disorder has hindered the detection of a spin gap at low temperatures un-

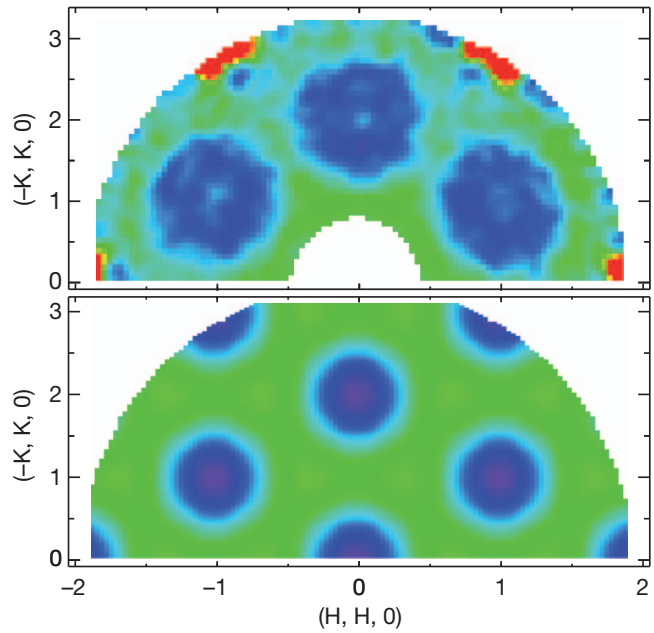


Figure 26. The continuum of fractionalized $S = 1/2$ excitations in herbertsmithite, reproduced with permission from Ref. [272]. The top panel shows INS data in the $(HK0)$ scattering plane, measured at $T = 1.5\text{ K}$ at an energy transfer of 5 meV on a synthetic deuterated single crystal of $\gamma\text{-ZnCu}_3(\text{OD})_6\text{Cl}_2$. The bottom panel shows the calculated magnetic structure factor, $S_{\text{mag}}(Q)$, for a simple model of uncorrelated nearest-neighbor dimers, similar to a short-range RVB state.

til it was finally observed in recent NMR measurements, evidenced by a sharp drop in the nuclear magnetic relaxation rate, $1/T_1$, and in the ^{17}O NMR frequency shift [287, 288]. The resulting value of the spin gap, $\Delta \approx 10$ K, favors theories promoting a \mathbb{Z}_2 (topological) quantum spin-liquid ground state with a spin-gap of order $0.1J$ [289–297], supplanting alternative scenarios like valence-bond solids or gapless (algebraic) spin liquids [283, 298–311].

The momentum-space structure of spin correlations in herbertsmithite was investigated by Han *et al.* using neutron scattering [272]. The experiment on a synthetic deuterated single-crystal sample of $\gamma\text{-ZnCu}_3(\text{OD})_6\text{Cl}_2$ revealed an exceedingly diffuse signal spanning a large fraction of the Brillouin zone at low energies (Fig. 26). It has been associated with a continuum of fractionalized $S = 1/2$ excitations on the kagomé lattice, similar to spinons, in strong contrast to sharp spin-wave excitations in nonfrustrated magnets. Figure 26 compares these INS data with the results of a model calculation for a collection of uncorrelated nearest-neighbor singlets on the kagomé lattice. This model qualitatively captures the magnetic spectral-weight distribution, but overestimates the width of peaks in reciprocal space, indicating that spin-spin correlations beyond the nearest neighbors also play an important role in herbertsmithite [272]. In follow-up theoretical works, the influence of additional Hamiltonian parameters, such as Ising and DMI terms [296, 312], as well as second-neighbor AFM Heisenberg interactions [296], on the magnetic structure factor, $S_{\text{mag}}(Q)$, was also considered.

Another important ingredient influencing the dynamical spin structure factor is chemical disorder, which can lead to a randomness-induced quantum spin liquid behavior (random-singlet state) above a certain critical value [313]. In a more recent work, Han *et al.* [314] argued that the low-energy magnetic fluctuations also contain a considerable contribution from antiferromagnetically correlated magnetic Cu impurities on the nominally non-magnetic Zn intersites. According to single-crystal ^2D NMR [316] and resonant x-ray diffraction measurements [317], the concentration of such weakly interacting Cu^{2+} defect spins reaches 15%. On the other hand, the possibility of Zn^{2+} impurities occupying the kagomé sites can be essentially eliminated in the best of the studied samples. The authors of Ref. [314] indicate a good agreement between predictions of their impurity model and the low-energy neutron data that reveal a small spin gap of ~ 0.7 meV after subtraction of the impurity signal. The same model

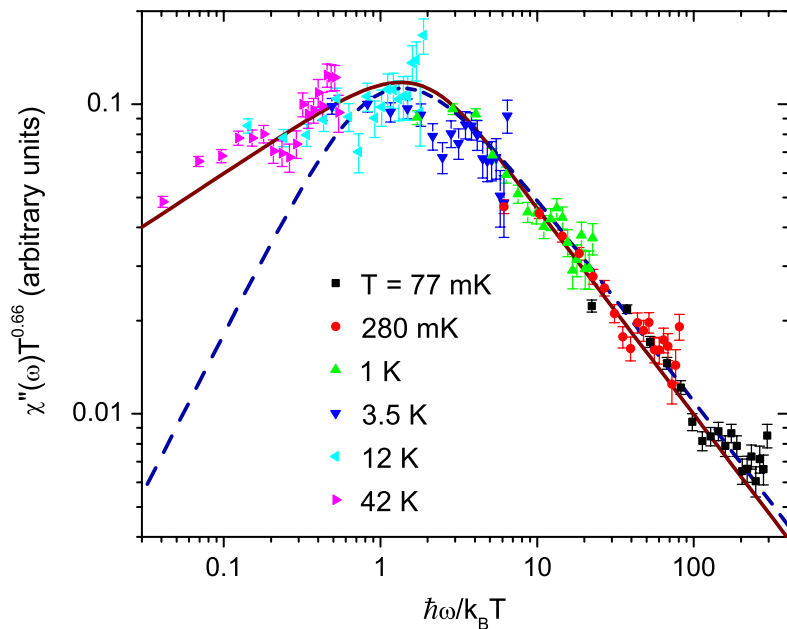


Figure 27. The universal ω/T scaling of the dynamic spin susceptibility in herbertsmithite. The measured values of $\chi''(\omega)T^\alpha$ with $\alpha \approx 2/3$, plotted against $\hbar\omega/k_B T$ on a log-log scale, collapse onto a single curve. Reproduced with permission from Ref. [315], copyright by the American Physical Society.

is also able to explain the divergent response in the dynamic spin susceptibility below 1 meV [315] and is consistent with the NMR and specific-heat data [276].

The bulk ac susceptibility and the dynamic susceptibility measured by neutron spectroscopy show a universal scaling relationship in herbertsmithite that is typical for systems with disorder or in proximity to a QCP [315]. In Fig. 27, the dynamic spin susceptibility extracted from INS data, $\chi''(\omega, T)$, is plotted for various temperatures. The quantity $\chi''(\omega, T)T^\alpha$ with $\alpha \approx 2/3$ collapses on a single curve as a function of $\hbar\omega/k_B T$. It can be well described by the same functional form $F(\omega/T) = (T/\omega)^\alpha \tanh(\omega/\beta T)$ as the one used to fit the dynamic susceptibility in $\text{La}_{1.96}\text{Sr}_{0.04}\text{CuO}_4$ [318] and in some heavy-fermion metals such as $\text{Ce}(\text{Rh}_{0.8}\text{Pd}_{0.2})\text{Sb}$ [319] and $\text{UCu}_{5-x}\text{Pd}_x$ [320] (solid line). On the other hand, an alternative scaling that was successful in the case of $\text{CeCu}_{5.9}\text{Au}_{0.1}$ [321, 322] (dashed line) fails to describe the data. The observed scaling behavior in herbertsmithite could be attributed to a critical spin-liquid ground state [323], but could also be related to disorder. It was pointed out [315] that it shares common features with disordered heavy-fermion metals and random magnetic systems featuring a Griffiths phase [324, 325] or a random-singlet phase [326]. The randomness among valence-bond singlets formed by neighboring Cu spins in the spin-liquid regime was also claimed responsible for the recently observed broadening of an infrared phonon [327], as expected for a VBS state [284].

The situation with understanding the low-temperature magnetism in herbertsmithite is further complicated by the recent results of Zorko *et al.* [328] who observed two distinct types of defects with different magnetic couplings to the kagomé spins in their ESR data. This magnetic response contradicts the threefold symmetry of the ideal kagomé lattice, suggesting a minor deviation from the perfect symmetry due to a structural distortion at low temperatures. To what extent this structural distortion is governed by the presence of impurities, and what is its role in stabilizing the spin-liquid ground state, remains to be seen.

Apart from the most studied herbertsmithite, structurally perfect $S = 1/2$ KAFM lattices are also realized in its isostructural Mg, Ni, and Co analogues tondiite, $\gamma\text{-MgCu}_3(\text{OH})_6\text{Cl}_2$ [329, 330], gillardite, $\gamma\text{-NiCu}_3(\text{OH})_6\text{Cl}_2$ [331], and leverettite, $\gamma\text{-CoCu}_3(\text{OH})_6\text{Cl}_2$ [332]. The lattice parameters of tondiite and leverettite are very close to those of herbertsmithite, whereas gillardite has a smaller c lattice constant due to the smaller radius of the Ni^{2+} ion as compared to the Zn^{2+} ion. Even before the discovery of natural tondiite was reported in 2014 [330], the magnetic properties of this compound were investigated on a synthetic powder sample. Initial characterization revealed a Curie-Weiss temperature of $\Theta_{\text{CW}} \approx -284$ K and a weak ferromagnetic ordering below $T_C \approx 4-5$ K, which was attributed to impurities [329]. The absence of any magnetic ordering or spin freezing down to 20 mK ($\sim 10^{-4} \text{ J}$) was demonstrated with μSR [333]. In the same experiment, the low-temperature relaxation rate exhibited a power-law scaling, $T_1 \propto \omega^\alpha$ with $\alpha \approx 0.63$, pointing to an exotic relaxation channel for intersite defects. This power law can be reconciled with the above-mentioned critical ω/T scaling with $\alpha = 2/3$ in the neutron data on herbertsmithite, shown in Fig. 27 [315].

The magnetic properties of $\gamma\text{-NiCu}_3(\text{OH})_6\text{Cl}_2$ (gillardite) and $\gamma\text{-CoCu}_3(\text{OH})_6\text{Cl}_2$ (leverettite) have been probed by magnetization and susceptibility measurements [334]. In contrast to herbertsmithite, the interlayer sites in these compounds are occupied by magnetic Ni^{2+} ($S = 1$, $\mu_{\text{eff}} = 3.5\mu_B$) and Co^{2+} ($S = 3/2$, $\mu_{\text{eff}} = 4.9\mu_B$) ions, respectively. This opens up new magnetic

interaction paths between kagomé layers that still await a systematic exploration. A much stronger interlayer coupling is evidenced by the reduced Curie-Weiss temperatures ($\Theta_{\text{CW}} = -100$ K and -40 K, respectively), as compared to herbertsmithite, and is expected to alter the low-temperature magnetic behavior substantially in both compounds [334].

4.4. Kapellasite vs. haydeeite: The role of further-neighbor exchange

The mineral kapellasite is a metastable polymorph of herbertsmithite, in which Zn ions occupy positions in the kagomé layers rather than at the intersites [56, 335, 336]. It is described by the space group $P\bar{3}m1$ and is commonly referred to* as $\alpha\text{-ZnCu}_3(\text{OH})_6\text{Cl}_2$. Its isostructural Mg- and Mn-rich analogues haydeeite, $\alpha\text{-MgCu}_3(\text{OH})_6\text{Cl}_2$ [341], and misakiite, $\alpha\text{-MnCu}_3(\text{OH})_6\text{Cl}_2$ [342], are also known. In the first comparative study of kapellasite and haydeeite, Janson *et al.* [226] employed electronic-structure and exact-diagonalization calculations to argue that further-neighbor exchange interactions across the kagomé hexagons, shown in Fig. 28 (a), may play a crucial role in determining the magnetic ground states of both minerals. The corresponding exchange constants, $J_d \approx 0.9$ meV for kapellasite vs. 0.8 meV for haydeeite, are nearly the same. However, the nearest-neighbor AFM interaction J_1 along the sides of the kagomé triangles is 3 times stronger in kapellasite than in haydeeite. At the same time, the second-nearest-neighbor coupling J_2 is negligible. This implies that the ground state is solely determined by the ratio $\alpha = J_d/J_1$ that is very different for the two compounds: $\alpha \approx 0.36$ for kapellasite and $\alpha \approx 1$ for haydeeite. The diagonal coupling lifts the degeneracy of the pure KAFM ground state ($\alpha = 0$) in favor of a complex noncoplanar “cuboc” order with 12 magnetic sublattices similar to the one proposed for the $J_1\text{-}J_2$ kagomé Heisenberg model [343]. For strong J_d , magnetic correlations along the chains built by diagonal bonds dominate, suggesting that low-energy spin dynamics in haydeeite may be represented by fractionalized spinon excitations as in 1D spin-chain models.

Experimental results available to date suggest that kapellasite develops no long-range order, but rather short-range magnetic correlations with the noncollinear “cuboc2” structure [240], whereas haydeeite orders ferromagnetically at $T_C = 4.2$ K [336]. The importance of the diagonal AFM interaction $J_d \approx 1.3$ meV was confirmed by the analysis of susceptibility and specific-heat data [240, 241]. However, in con-

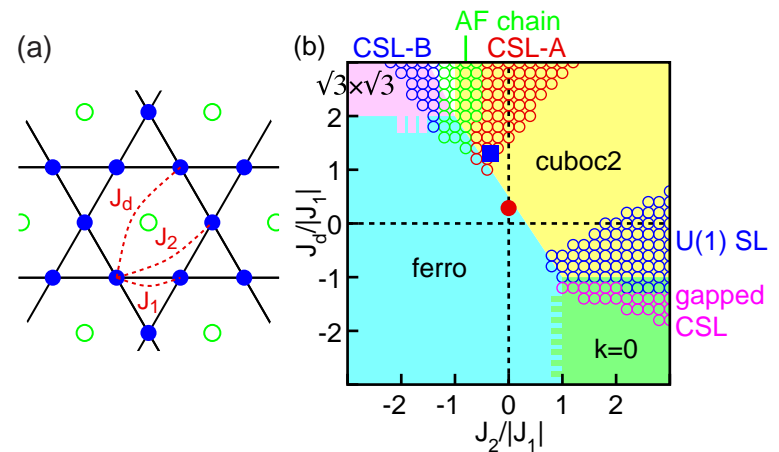


Figure 28. (a) Main exchange interactions on the Cu²⁺ kagomé lattice of kapellasite and haydeeite. (b) Estimated location of kapellasite (square) and haydeeite (circle) on a classical phase diagram of the kagomé lattice with FM J_1 interactions. Reproduced with permission from Ref. [339], copyright by the American Physical Society.

*Alternative naming for polymorphs based on the chronological order of their discovery can also be found in the literature [337], but the one adopted here is by far the most common [329, 336, 338–340].

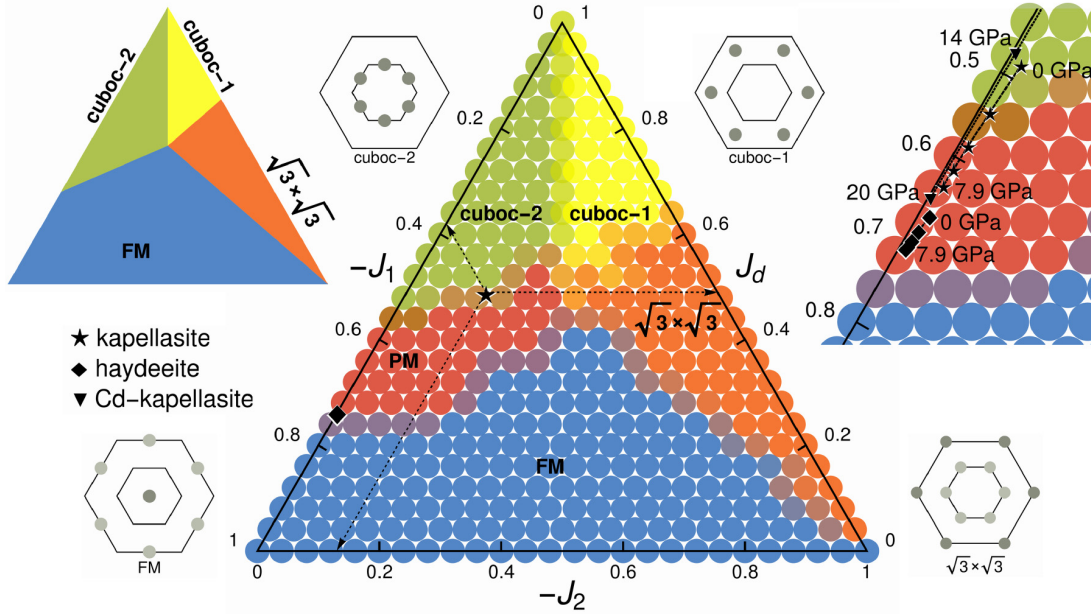


Figure 29. Quantum phase diagram of the J_1 - J_2 - J_d Heisenberg model on a kagomé lattice. The classical phase diagram is shown at the left for comparison. Black symbols mark the experimentally obtained exchange couplings for kapellasite and haydeeite [240, 241, 339]. The dependence of coupling constants in different materials on pressure is shown in the enlarged region on the right. Reproduced with permission from Ref. [228], copyright by the American Physical Society.

trast to the theoretical prediction of Janson *et al.* [226], the NN exchange constant was found to be ferromagnetic, $J_1 \approx -1$ meV for kapellasite [240, 241, 338] and $J_1 \approx -3.3$ meV for haydeeite [339]. Figure 28 (b) shows the phase diagram of classical ground states for a Heisenberg model on the kagomé lattice with $J_1 < 0$ and two further-neighbor couplings J_2 and J_d [228, 240, 339, 344, 345]. According to the exchange constants estimated from neutron-spectroscopy data, kapellasite and haydeeite are located in the “cuboc2” and ferromagnetic phases, respectively, very close to the transition line that separates them [339]. This result is consistent with direct experimental measurements of their magnetic ground states.

A more recent theoretical work by Iqbal *et al.* [228] extended these results to investigate possible regions in the phase diagram traversed by α -(Zn,Mg,Cd)Cu₃(OH)₆Cl₂ compounds as a function of pressure, based on *ab initio* DFT calculations. In the quantum phase diagram shown in Fig. 29, they found an extended region of a paramagnetic domain for intermediate values of J_d that separates the FM and “cuboc2” phases. It has been predicted that kapellasite, located at the onset of the “cuboc2” phase, would enter this region under elevated hydrostatic pressure. An even stronger pressure dependence covering a vast extent along the J_d axis was predicted for the then unknown Cd-kapellasite, α -CdCu₃(OH)₆Cl₂ [228]. Meanwhile, a very similar compound with this structure, CdCu₃(OH)₆(NO₃)₂ · H₂O [346], also termed Cd-kapellasite, has been grown in single-crystal form by the hydrothermal transport method [224]. At ambient pressure, it develops an NVC spin order [as shown in Fig. 22 (b)] below $T_N \approx 4$ K, accompanied by a small spontaneous magnetization. Its origin is related to the DMI, which is considered negligible (with $D/J_1 \approx 3\%$ [338]) for kapellasite and haydeeite. Another important difference lies in the NN exchange constant that was estimated

to be antiferromagnetic, $J_1 \approx 3.9$ meV, whereas further-neighbor interactions J_2 and J_d could not yet be reliably determined from the existing data.

Finally, it is also worthwhile to mention the effect of disorder on the magnetic properties of kapellasite. In a study that employed a combination of ^{35}Cl NMR, ESR, and μSR , Kermarrec *et al.* [338] revealed a severe random depletion of the magnetic kagomé lattice by 27% due to Cu/Zn site intermixing even in high-quality synthetic powder samples. Their surprising finding was that the high-temperature magnetic response of the system remains homogeneous in spite of the structural disorder. The variety of local magnetic environments leads to an appearance of local low-energy excitation modes that broaden the distribution of spin-lattice relaxation times at low temperatures. Due to the metastability of the α - $\text{ZnCu}_3(\text{OH})_6\text{Cl}_2$ polymorph and the proximity of ionic radii of Zn^{2+} and Cu^{2+} ions, it remains a real chemical challenge to decrease the amount of structural disorder in the kagomé layers and thereby improve the quality of synthetic samples.

One possible way to circumvent this problem is to replace Zn^{2+} with another nonmagnetic cation. Such a possibility is offered by the newly discovered mineral centennialite of the atacamite group, $\text{CaCu}_3\text{Cl}_2(\text{OH})_6 \cdot 0.7\text{H}_2\text{O}$ [348], which is also structurally related to kapellasite and haydeeite, but is much less studied. In synthetic samples synthesized by a solid-state reaction method [349], the intersite mixing between Ca and Cu atoms was limited to $< 5\%$, which is a significant improvement in comparison to Zn. According to susceptibility data, centennialite is characterized by a Curie-Weiss temperature of $\Theta_{\text{CW}} \approx -56$ K and orders antiferromagnetically below $T_N \approx 7$ K, implying a moderate frustration parameter of $|\Theta_{\text{CW}}|/T_N \approx 8$ [349]. The successful growth of mm-sized single crystals (Fig. 30) by a hydrothermal reaction in a two-zone tube furnace enabled an estimation of the exchange constants $J_1 \approx 4.5$, $J_2 \approx -0.6$, and $J_d \approx 1.0$ meV from the high-temperature series expansion fitting of the magnetic susceptibility data [347]. *Ab initio* DFT calculations predict that J_1 should change sign at a bond angle of 108.5° in the kapellasite family [228], and therefore the AFM character of the NN exchange constant in centennialite is consistent with the large Cu–O–Cu bond angle of 113.9° that is influenced by the ionic radius of the nonmagnetic cation. The estimated parameters place this compound near the multi-critical point of the $\sqrt{3} \times \sqrt{3}$, “ $q = 0$ ”, and “cuboc1” phases in the magnetic phase diagram for an isotropic classical Heisenberg model with $J_1 > 0$ [241, 345]. This implies that novel magnetic ground states, distinct from those found in other atacamite minerals, can be realized in this new kagomé-lattice compound with practically no disorder.

An alternative possibility to avoid disorder in the $S = 1/2$ kagomé lattice is offered by the telluride mineral quetzalcoatlite, $\text{Zn}_6\text{Cu}_3(\text{TeO}_6)_2(\text{OH})_6 \cdot \text{Ag}_x\text{Pb}_y\text{Cl}_{x+2y}$ [350]. As noticed by Norman [351], its crystal structure contains perfect kagomé layers with an AA stacking, like in

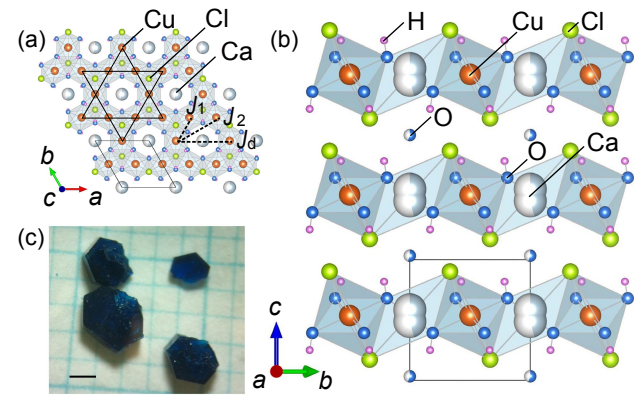


Figure 30. Crystal structure and large synthetic single crystals of centennialite (shown on mm paper). Reproduced with permission from Ref. [347], copyright by the Physical Society of Japan.

kapellasite (as opposed to ABC stacking in herbertsmithite). The tetrahedral coordination of the Zn ions within the $\text{ZnO}_2(\text{OH})_2$ units, located on interlayer positions, should prevent disorder resulting from the Cu ions going to the intersites. One should therefore expect considerable interest to this mineral from both chemists and solid-state physicists.

4.5. Volborthite, vesignieite, and alike: Nonequivalent bonds resulting from lattice distortions

In some of the $S = 1/2$ kagomé minerals, frustration is relieved by structural distortions within the kagomé plane, which leads to non-equivalent exchange on the triangles. Historically, the mineral volborthite, $\text{Cu}_3\text{V}_2\text{O}_7(\text{OH})_2 \cdot 2\text{H}_2\text{O}$ with monoclinic space group $C2/m$, was among the first candidate compounds for the realization of a $S = 1/2$ KAFM model system [352–354]. Its monoclinic distortion was initially considered small enough to keep the essential physics. However, it soon became clear that volborthite orders antiferromagnetically at temperatures near 1 K [248, 249]. In magnetic fields above $B_{s1} \approx 4.5$ T, a second ordered phase (phase II) with a coplanar cycloidal structure forms, persisting to $B_{s2} \approx 25.6$ T, where it gives way to a high-field collinear ferrimagnetic phase (phase III) with a much higher ordering temperature of ~ 26 K [250, 355]. Later, measurements in pulsed magnetic fields up to 68 T [356] revealed an additional transition at $B_{s3} \approx 47$ T. A cycloidal-spiral ground state similar to the phase II of volborthite was theoretically predicted for the spatially anisotropic magnetic model on a distorted kagomé lattice [357].

The first theoretical analysis of the microscopic magnetic model for volborthite by Janson *et al.* [358] revealed that its physics may be largely different from that of the initially assumed kagomé model. An orbital ordering on the Cu^{2+} sublattice leads to a structural distortion and breaks the equivalency between the Cu(1) and Cu(2) sites with the occupied $3d_{z^2-r^2}$ and $3d_{x^2-y^2}$ orbitals, respectively, as illustrated in Fig. 31 (d). The corresponding magnetic model presumably requires three relevant couplings: the nearest-neighbor FM exchange $J_1 \approx -6.9$ meV along the base of the isosceles triangles, the strong AFM coupling $J_{\text{ic}} \approx 8.6$ meV along the two other sides of the triangles, and the NNN

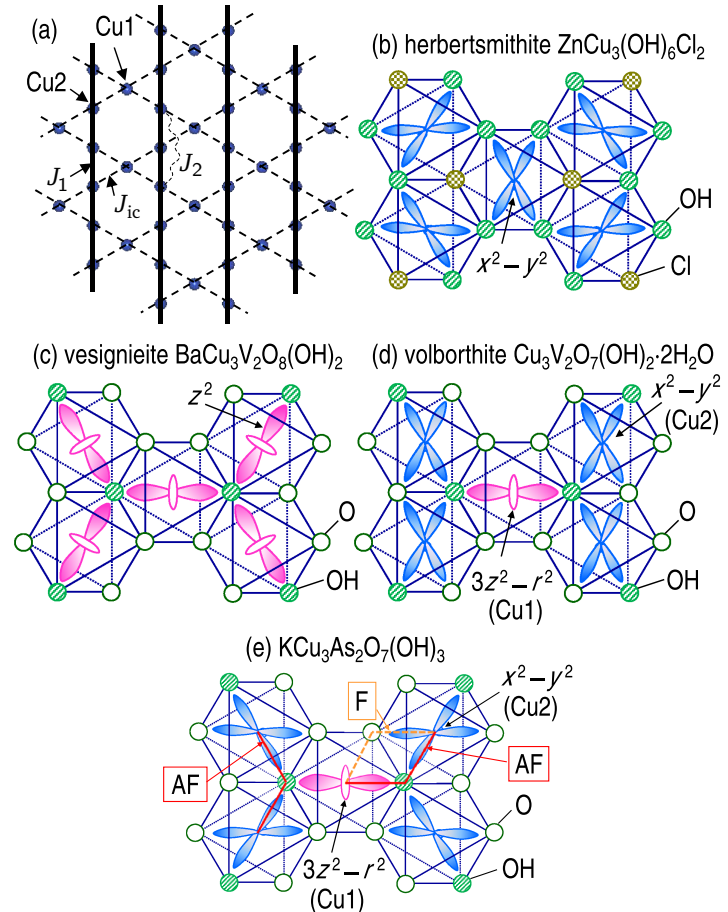


Figure 31. (a) Exchange interactions on a kagomé lattice with an anisotropic distortion. (b–e) Orbital arrangements in various copper minerals. Reproduced from Ref. [252], copyright by the Physical Society of Japan.

exchange interaction $J_2 \approx 3$ meV, as shown in Fig. 31 (a). In the proposed model, both J_1 and J_{ic} with opposite signs supported each other and did not give rise to frustration, hence the only source of frustration came from J_2 . The resulting model was therefore thought to be much closer to frustrated coupled chains than to KAFM lattices.

Powder neutron-scattering measurements that followed shortly afterwards [359] indicated the presence of short-range magnetic order emerging in zero magnetic field below 5 K at two characteristic wave vectors, $Q_1 = 0.65 \text{ \AA}^{-1}$ and $Q_2 = 1.15 \text{ \AA}^{-1}$, two steep spin-wave branches dispersing from these wave vectors, and a flat mode at an energy of 5.0 meV. However, the experimental Q_1 and Q_2 values could not be reconciled with any of the magnetic structures expected for the theoretically predicted J_1 - J_2 - J_{ic} model [357, 358].

The situation cleared somewhat when thermodynamic measurements on volborthite single crystals became available. The specific-heat data of Yoshida *et al.* [360] revealed a first-order orbitally driven structural phase transition at $T_s \approx 300$ K and two successive low-temperature magnetic phase transitions at 1.19 K and 0.81 K instead of a broad kink seen previously in a powder sample [361]. The phase transition at T_s has been associated with an orbital switching [360, 362], as the unpaired electron on the Cu(1) site “switches” from the $d_{z^2-r^2}$ orbital in the high-temperature phase to the $d_{x^2-y^2}$ orbital in the low-temperature phase. Therefore, at low temperatures, the spin-carrying orbital on both Cu²⁺ sites is $d_{x^2-y^2}$, as in herbertsmithite, but the orientations of the orbitals with respect to each other are different between the two compounds. The consequence of this new orbital configuration for the magnetic model is the broken equivalency between the two J_{ic} bonds, as illustrated in Fig. 32. In addition, superlattice reflections were observed below T_s by x-ray diffraction, indicating a doubling of the unit cell along the c axis [360]. Furthermore, a second high-temperature polymorph with a flipped d -orbital orientation on the Cu(1) site and a different $C2/m$ lattice symmetry has been reported [362, 363]. The space group of the low-temperature phase was determined to be $I2/a$, implying that the magnetic model of volborthite had to be modified.

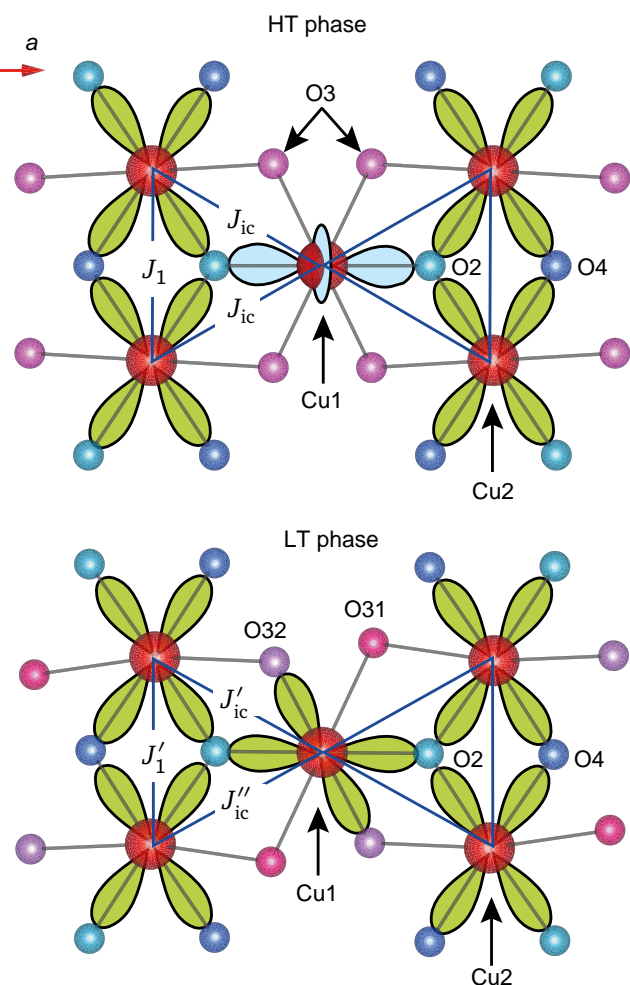


Figure 32. (a) Orbital switching between the high- T (top) and low- T (bottom) phases of volborthite, breaking the equivalency of the J_{ic} bonds. Adapted with permission from Ref. [360], copyright by the Macmillan Publishers Ltd.

Soon after the new data on volborthite single crystals became available, Janson *et al.* [364] updated their magnetic model of volborthite in the framework of DFT+*U*, based on the new single-crystal structural data from Ref. [365]. Their new model involved four leading magnetic interactions: antiferromagnetic J and J_2 and ferromagnetic J' and J_1 , as shown in Fig. 33 (a,b). This model results in a system of coupled trimers, contrary to the previously proposed frustrated chains, and it can explain the $\frac{1}{3}$ -plateau in the magnetization [365] as a result of polarized “up-up-down” states formed on magnetic trimers. Each trimer is connected ferromagnetically to its four nearest neighbors and antiferromagnetically to its two second neighbors, as illustrated in Fig. 33 (d). In no external magnetic field, this model supports a bond-nematic phase due to the condensation of two-magnon bound states.

In the most recent theoretical paper, Chern *et al.* [366] considered a similar model with four leading exchange interactions and argued that it could host 12 distinct \mathbb{Z}_2 spin-liquid phases with fractionalized excitations. The natural candidate for one such phase would be the state that exists in the narrow temperature window between the two low-temperature phase transitions, immediately above the AFM phase, where finite thermal Hall conductivity has been revealed recently [367]. The theory relates it to the existence of a spinon Fermi surface, characteristic of a $U(1)$ spin liquid due to the effective Lorentz force exerted on the deconfined spinons from the $U(1)$ gauge field coupled to the external magnetic field [368].

The understanding of high-field magnetic phases in volborthite also received a second impetus from the successful growth of high-quality single crystals [365]. A wide $1/3$ magnetization plateau has been observed in fields between 28 and 74 T and associated with the ferrimagnetic spin structure of phase III. Below 23 T, ^{51}V NMR measurements evidenced an incommensurate order within phase II. But between ~ 23 T and B_{s2} , a novel intermediate phase (“phase *N*”) with linear field dependence of the magnetization has been found. Judging from the heavily broadened NMR spectrum within this phase, it is characterized by an inhomogeneous distribution of the internal fields, indicative of disorder among static spin moments. This is likely related to the arrangement of the crystal wa-

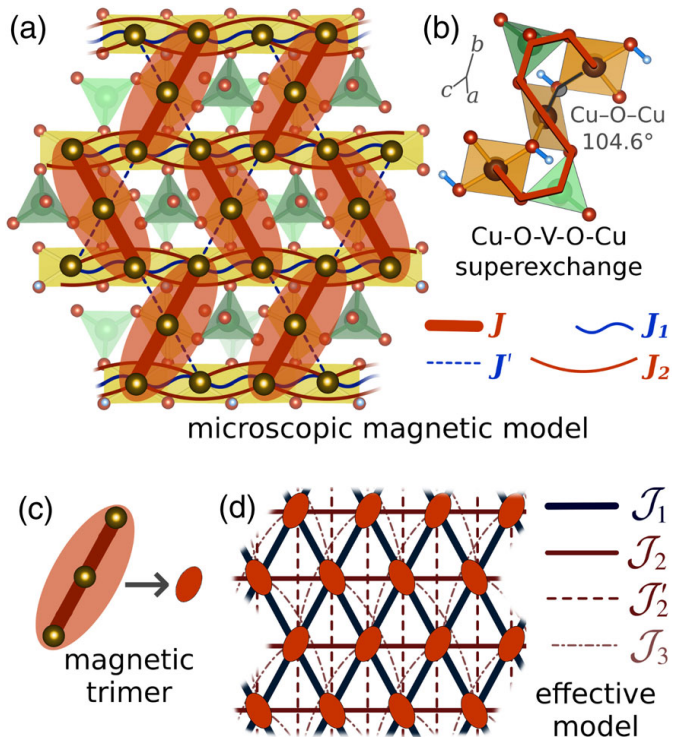


Figure 33. (a) The new microscopic magnetic model of volborthite, featuring magnetic trimers (shaded ovals), formed by the dominant AFM interaction J . (b) The Cu–O–V–O–Cu superexchange paths within the trimer. (c,d) An effective model of interacting trimers with ferromagnetic J_1 and antiferromagnetic J_2 , J_2' , and J_3 . Reproduced with permission from Ref. [364], copyright by the American Physical Society.

ter molecules between the kagomé planes [365]. Finally, the nuclear spin-lattice relaxation rate $1/T_1$, measured by ^{51}V NMR in the ferrimagnetic phase above 28 T, helped to estimate the excitation gap with a large g factor of $\sim 5.5 \pm 0.7$, which the authors associate with a magnon bound state [369]. A possible spin-nematic phase at high fields, evidenced by a slowing down of spin fluctuations due to the condensation of magnon bound states, has therefore been proposed.

The ordering patterns among $d_{x^2-y^2}$ and $d_{3z^2-r^2}$ copper orbitals that attracted so much attention to volborthite over the last two decades also play a role in a number of other kagomé minerals. For instance, an orbital arrangement similar to that of volborthite but with a different orientation of the $d_{x^2-y^2}$ orbitals on the Cu(2) sites has been proposed for $\text{KCu}_3\text{As}_2\text{O}_7(\text{OH})_3$ [252], as illustrated in Fig. 31 (e). This synthetic compound has the same monoclinic space group $C2/m$ as volborthite, implying a structural distortion of the kagomé planes, and orders antiferromagnetically below $T_N \approx 7.2$ K. Here the J_1 interaction between the Cu(2) sites was proposed to be AFM, in contrast to volborthite, and would be therefore frustrated for any sign of the J_{ic} interaction between Cu(1) and Cu(2). Low-temperature magnetic diffraction patterns revealed that below T_N $\text{KCu}_3\text{As}_2\text{O}_7(\text{OD})_3$ develops a complex incommensurate helical structure that leads to multiferroic properties [370]. A follow-up study of the magnetic phase diagram in applied fields up to 20 T found a metamagnetic transition related to the rotation of the helix plane away from the easy plane around $B_c \approx 3.7$ T [337].

In the structurally related mineral vesignieite, $\text{BaCu}_3(\text{VO}_4)_2(\text{OH})_2$ [371, 372] (space group $B2/m$), the spins are carried exclusively by the $d_{3y^2-r^2}$ orbitals, as shown in Fig. 31 (c) [252]. This reduces the spatial anisotropy in the kagomé planes, but in contrast to the highly symmetric trigonal structure of herbertsmithite, the monoclinic distortion still remains finite. A higher-symmetry polymorph of the same compound with structurally perfect kagomé layers, termed β -vesignieite, could also be synthesized [373], but we focus here on the original α -vesignieite that can be found in nature. It has been initially reported to order magnetically and form a “ $\mathbf{q} = 0$ ” type of spin structure with in-plane spin components oriented at nearly 120° with respect to each other [374]. Another study proposed instead a more exotic state below 9 K with a coexistence of dynamical and frozen moments [375]. It has been also suggested that the intrinsic ground state of vesignieite could resemble a spin liquid, similar to herbertsmithite [251, 376, 377]. An important difference, however, comes from the stronger DMI [375, 377]. In the $S = 1/2$ KAFM model with only one NN Heisenberg exchange J , a quantum phase transition to an ordered state has been predicted for the critical value of the DMI, $D_C = 0.1J$ [232]. In herbertsmithite, the estimates fall in the range $0.044 < D/J < 0.08$ [278, 378], placing it on the spin-liquid side of the QCP. In vesignieite, however, this ratio was estimated in the uncertainty range $0.1 < D/J < 0.19$ [377, 379], placing it just on the other side of the QCP. Based on the ESR line width, Zorko *et al.* [379] found that the DMI is highly anisotropic with the dominant in-plane component $D_{\parallel} \approx 0.19J$ and smaller out-of-plane component $D_{\perp} \approx 0.07J$, comparable to herbertsmithite. The large D_{\parallel} parameter suppresses quantum spin fluctuations and promotes long-range ordering below $T_N \approx 9$ K rather than a spin-liquid state.

A realistic magnetic model that considers the anisotropic DMI in addition to the two inequivalent exchange constants J and J' along the sides of isosceles triangles, as illustrated here in Fig. 34, has been studied theoretically by Owerre [380]. He proposed that the application

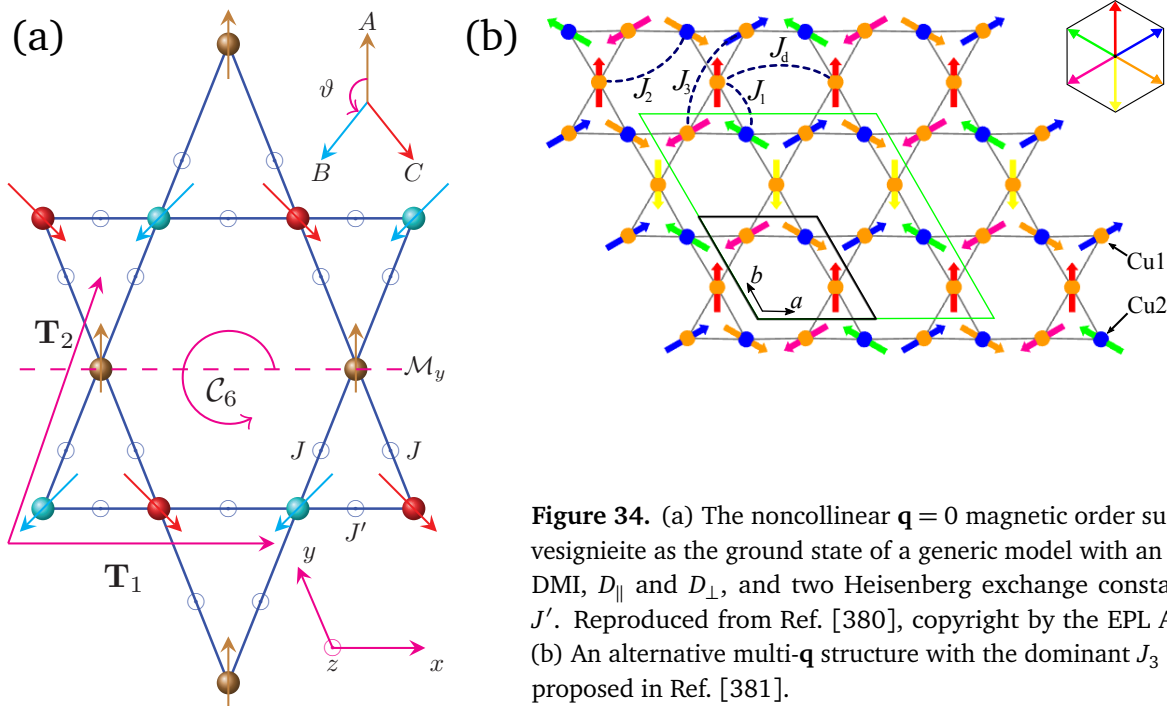


Figure 34. (a) The noncollinear $\mathbf{q} = 0$ magnetic order suggested for vesignieite as the ground state of a generic model with an anisotropic DMI, D_{\parallel} and D_{\perp} , and two Heisenberg exchange constants, J and J' . Reproduced from Ref. [380], copyright by the EPL Association. (b) An alternative multi- \mathbf{q} structure with the dominant J_3 interaction, proposed in Ref. [381].

of magnetic field to such a system in the out-of-plane direction would result in a noncoplanar chiral spin texture with Berry curvature and nontrivial topological magnetic excitations. This can explain why the thermal Hall effect in volborthite was observed only in high magnetic fields [367]. The author suggests that similar effects can be expected in volborthite and another distorted kagomé mineral edwardsite, $\text{Cd}_2\text{Cu}_3(\text{SO}_4)_2(\text{OH})_6 \cdot 4\text{H}_2\text{O}$ (space group $P2_1/c$) [382], which orders with a canted AFM structure below 4.3 K and has the same orbital arrangement as herbertsmithite [383]. However, high-field magnetization measurements on edwardsite showed a saturated value of only 1/3 of the full expected moment up to 50 T, and the analysis of specific heat suggests that only 1/3 of the spins contribute to the magnetic order, while the other 2/3 form singlets and are therefore magnetically inactive [384]. The DMI in edwardsite may be even larger than in vesignieite, and the presence of 4 inequivalent Cu sites results in a rather complex magnetic model consisting of approximately isosceles J - J' - J' triangles that are arranged to form linear trimers with J , which can explain the weakly ferromagnetic canted $\sim 120^\circ$ spin structure [384].

Contrary to the previously suggested models, most recent INS measurements, carried out on a synthetic deuterated powder sample of vesignieite, indicate that the magnetic model is actually dominated by the third-nearest-neighbor AFM Heisenberg exchange J_3 [381]. The contributions from NN and NNN interactions turned out to be much smaller, to an extent that the experimental spin-wave spectrum is well described by a J_3 -only model with a small symmetric exchange anisotropy. According to the proposed classification of ordered states on the kagomé lattice [385], this model should lead to another type of a 120° magnetic order, shown in Fig. 34, which is characterized by a star of propagation vectors equivalent to $\{\frac{1}{2}00\}$. In this rather unusual triple- \mathbf{q} structure, the Fourier components of a given \mathbf{q} vector are nonzero for only one site, as suggested by the coloring of arrows. This substantially reduces the coupling between the ordered moments on different sites, as the dominant J_3 interaction acts within each of the three sublattices

individually, which are then coupled by much weaker frustrating interactions $J_1 = J$ and $J_2 = J'$. In the same work [381], a small spin gap of ~ 0.5 meV was observed in the spin-wave spectrum of vesignieite, which was attributed to a symmetric exchange anisotropy on J_3 , which amounts to $\delta/J_3 \approx -0.006$.

Finally, just as it was in the case of volborthite, an improvement in sample quality allowed Boldrin *et al.* [253] to observe an additional lowering of the lattice symmetry in recent synchrotron powder diffraction experiments on vesignieite. The x-ray data could be described by the trigonal $P3_121$ space group with additional weak Bragg reflections that are absent in the initially proposed structure. An isostructural compound with Sr instead of Ba, now known as Sr-vesignieite, has also been synthesized [386]. One exciting implication for both compounds, suggested by these results, is the orbital frustration on the Cu(2) site, where the $d_{x^2-y^2}$ and $d_{3z^2-r^2}$ orbitals are degenerate. Therefore, the Cu(2) spin fluctuates between two orbital arrangements, leaving all oxygens available to mediate superexchange with neighboring Cu(1) ions. This nontrivial coupling among the spin and orbital degrees of freedom, evidenced by the crystallographic signatures of the dynamic Jahn-Teller effect [386], appears to be an essential ingredient of the magnetic Hamiltonian that has never been previously considered. Future studies on single crystals of vesignieite may prove essential for unraveling the details of its low-temperature physics. While they are difficult to prepare via direct chemical reactions, it was recently reported that a topochemical transformation from the volborthite to vesignieite structure can be used to obtain mm-sized single crystals of high quality [387].

Among the less-studied copper minerals with a deformed kagomé lattice, one can also mention bayldonite, $\text{PbCu}_3(\text{AsO}_4)_2(\text{OH})_2$ (space group $C2/c$) [388], for which the importance of dynamic Jahn-Teller effects was already emphasized [389]. Another recently discovered mineral engelhauptite, $\text{KCu}_3(\text{V}_2\text{O}_7)(\text{OH})_2\text{Cl}$, space group $P6_3/mmc$ [390], can be viewed as an analogue of volborthite resulting from the replacement of water molecules by the equal amounts of K^+ and Cl^- ions. To the best of my knowledge, their magnetic properties have not been systematically investigated so far.

4.6. Francisite: buckled kagomé planes with bond frustration

Another type of distortion that can be found in kagomé compounds is the 3D buckling of magnetic kagomé planes. It is particularly pronounced in the layered cuprate mineral francisite, $\text{Cu}_3\text{Bi}(\text{SeO}_3)_2\text{O}_2\text{Cl}$ [391]. It has the orthorhombic space group $Pmmn$ at ambient conditions [392, 393], but undergoes a structural phase transition at $T^* = 115$ K to a lower-symmetry $Pcmm$ phase due to a distortion that doubles the unit cell along the c direction [394, 395] and leads to the appearance of multiple additional infrared phonon modes [396]. The physical origin of this transition has been attributed to an antiferroelectric distortion and is reportedly absent in the Br analogue, $\text{Cu}_3\text{Bi}(\text{SeO}_3)_2\text{O}_2\text{Br}$ [395, 397, 398]. The spin 1/2 is carried by Cu^{2+} ions on two inequivalent sites: Cu(1) that forms structural chains at the center of the magnetic layer and Cu(2) that occupies positions alternately above and below the Cu(1) plane, so that a kagomé-like quasi-2D structure is formed as a result (see Fig. 35). Weak interlayer interactions stabilize a long-range noncollinear magnetic order below $T_N = 25$ K [393, 394], which is shown in Fig. 36.

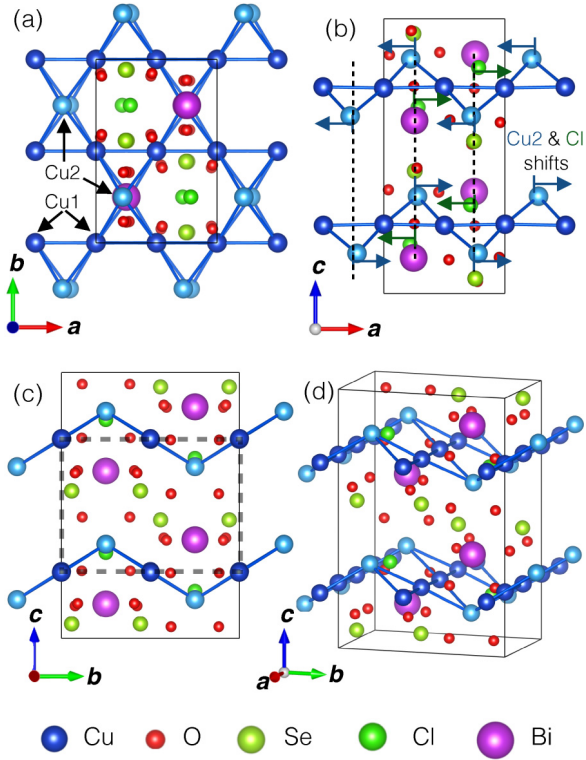


Figure 35. The crystal structure of francisite with buckled kagomé planes. Reproduced from Ref. [394], copyright by the American Physical Society.

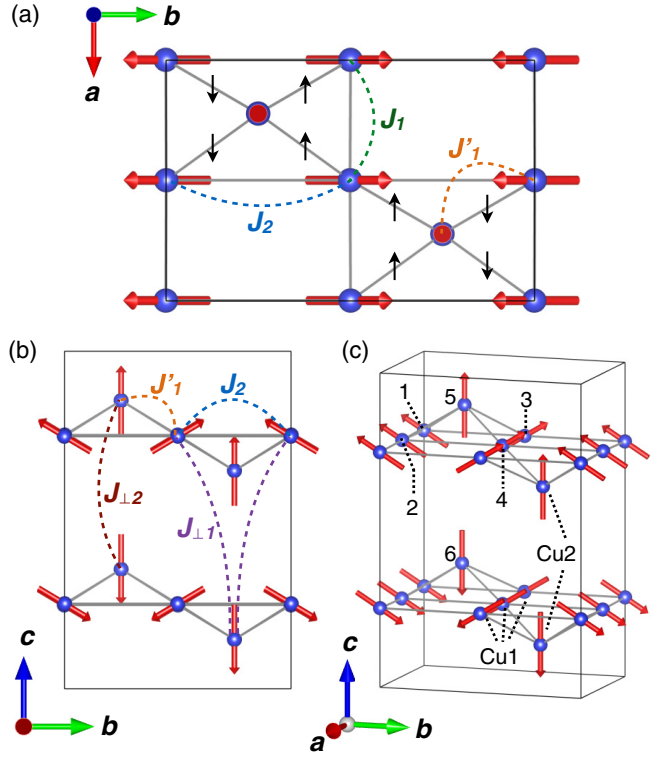


Figure 36. The refined magnetic structure and the microscopic magnetic model proposed for francisite. Reproduced from Ref. [394], copyright by the American Physical Society.

The microscopic magnetic model for francisite has been addressed in a number of recent theoretical and experimental works [397–400]. In an attempt to explain the canted AFM structure determined from single-crystal neutron diffraction [397], Rousouchatzakis *et al.* argued that the minimal model must include anisotropic DMI, in addition to the in- and out-of-plane Heisenberg exchange, which they estimated from DFT calculations [399]. Later, Nikolaev *et al.* [400] elaborated on their spin Hamiltonian, replacing it with an electronic one, with the advantage that the individual anisotropic terms no longer had to be separated, but were treated implicitly in the electronic Hamiltonian. This alternative *ab initio* approach based on the Hartree-Fock mean-field approximation for the electronic Hamiltonian resulted in a slightly different set of parameters for the effective magnetic model by taking into account hybridization effects and the spin-orbit interaction. In this model, the canted zero-field ground state arises from a competition among ferromagnetic NN and antiferromagnetic NNN interactions within the kagomé planes, whereas weaker anisotropic terms fix the spin directions and contribute to the anisotropic behavior of the magnetization. Therefore, the interaction regime in francisite can be considered similar to that of kapellasite in terms of the bond frustration imposed by the competition among the FM and AFM interactions, while the network of interactions is altered by the stronger buckling of kagomé layers.

It has to be noted that both theory papers treated francisite in its high-temperature $Pmmn$ structure, neglecting the lattice distortion present in the $Pcmn$ low-temperature phase that was

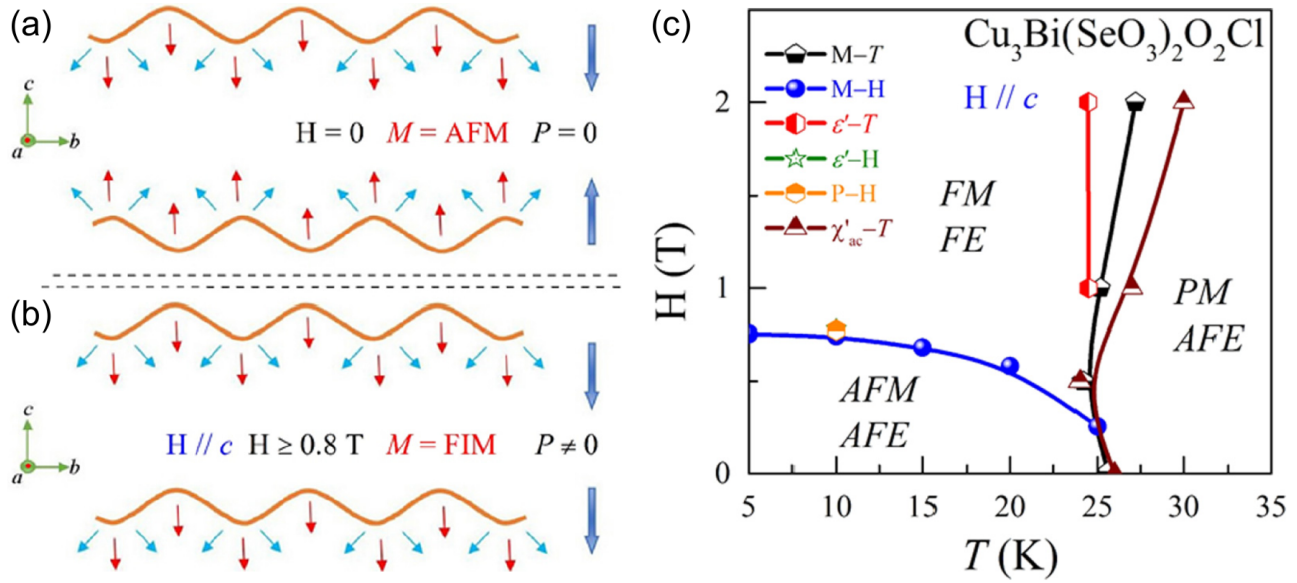


Figure 37. The field-induced metamagnetic transition in francisite from an AFM state (a) to a ferrimagnetic structure (b). The magnetic phase diagram (c) shows both phases in the temperature–magnetic-field plane. Reproduced with permission from Ref. [401], copyright by the American Physical Society.

only understood a year later [394, 395, 398]. In particular, the observation of a weak ferroelectric polarization loop below T^* led to a suggestion that the low-temperature structure is more likely characterized by the polar $P2_1mn$ than the originally proposed nonpolar $Pcmn$ space group [395]. However, direct structural refinement based on synchrotron x-ray diffraction measurements did not confirm this hypothesis [398]. Most likely, only a small fraction (about 10%) of the sample adopts the polar structure, which is only 3 meV/f.u. higher in energy, depending on the local pattern of Cl and Cu(2) displacements due to residual disorder [395]. The Br analogue of francisite, which avoids this structural transition, might be therefore a cleaner example for realization of the proposed theoretical models.

The most recent works focused on the multiferroic behavior of francisite and the field-induced metamagnetic spin-flip transition to a ferrimagnetic structure, which has been observed at the critical field $B_c \approx 0.8 \text{ T}$ applied along the c axis [401]. The spins within every Cu plane are arranged in a commensurate noncollinear structure with a net FM polarization. In zero magnetic field, these planes are arranged antiferromagnetically along the c direction, so that the FM moments are compensated, as shown in Fig. 37 (a). Above the critical field, all planes align with their moments parallel to the field direction as a result of a spin-flip transition seen as a clear step in the magnetization curve, and the ferrimagnetic structure shown in Fig. 37 (b) is realized above B_c . The ordering temperature remains nearly unchanged across the transition. The high-field ferrimagnetic phase of francisite showed interesting ferroelectric behavior in magnetodielectric and pyroelectric current measurements [401]. The phase diagram showing both phases as a function of temperature and magnetic field is reproduced in Fig. 37 (c).

In recent years, a group from Moscow State University systematically investigated the possibility of replacing Ba atoms in the francisite structure with Y or nonmagnetic lanthanides

[402–404] and with magnetic Sm [405]. All investigated $\text{Cu}_3R(\text{SeO}_3)_2\text{O}_2X$ ($R = \text{Y}, \text{La}, \text{Eu}, \text{Lu}$; $X = \text{Cl}, \text{Br}$) compounds with nonmagnetic R ions showed the same type of magnetic structure as francisite, with only slightly higher Néel temperatures between 31 and 38 K. A single metamagnetic transition was found at a higher critical field that varied between 2.4 and 3.0 T depending on the composition. This signifies different strengths of the interlayer exchange interaction, while the essential physics is qualitatively preserved. Unsurprisingly, the magnetic behavior of the Sm compound with the large Sm^{3+} spin and orbital magnetic moments turned out to be much more complex. This compound develops AFM order below $T_N = 35$ K and shows a spin-reorientation transition at $T_C = 8.5$ K. In magnetic field, the system undergoes multiple metamagnetic phase transitions before the magnetization saturates in moderate fields of several teslas [405].

4.7. Brochantite and Zn-brochantite: A new route to a kagomé spin liquid

One more kagomé compound that deserves to be mentioned here derives from the copper-sulfate mineral brochantite, $\text{Cu}_4\text{SO}_4(\text{OH})_6$, which crystallizes in the monoclinic $P2_1/a$ space group [406]. While the parent brochantite orders magnetically below 7.5 K with a weakly canted AFM structure, most interest in the field of quantum magnetism is attracted to its synthetic modification known as Zn-brochantite, in which 1/4 of the Cu atoms have been replaced with non-magnetic Zn. It was immediately recognized that this compound is a promising candidate for the realization of a quantum spin liquid, because it displays no magnetic ordering down to 50 mK despite a much higher Weiss temperature of -79 K [408]. From the T dependence of the susceptibility, a gapless RVB spin-liquid ground state with a spinon Fermi surface has been suggested [407–410]. However, Rietveld refinement of synchrotron powder x-ray diffraction data revealed that the kagomé layers in this system are both highly distorted and strongly buckled [408].

The assumption about the spin-liquid state of Zn-brochantite has been recently corroborated in a se-

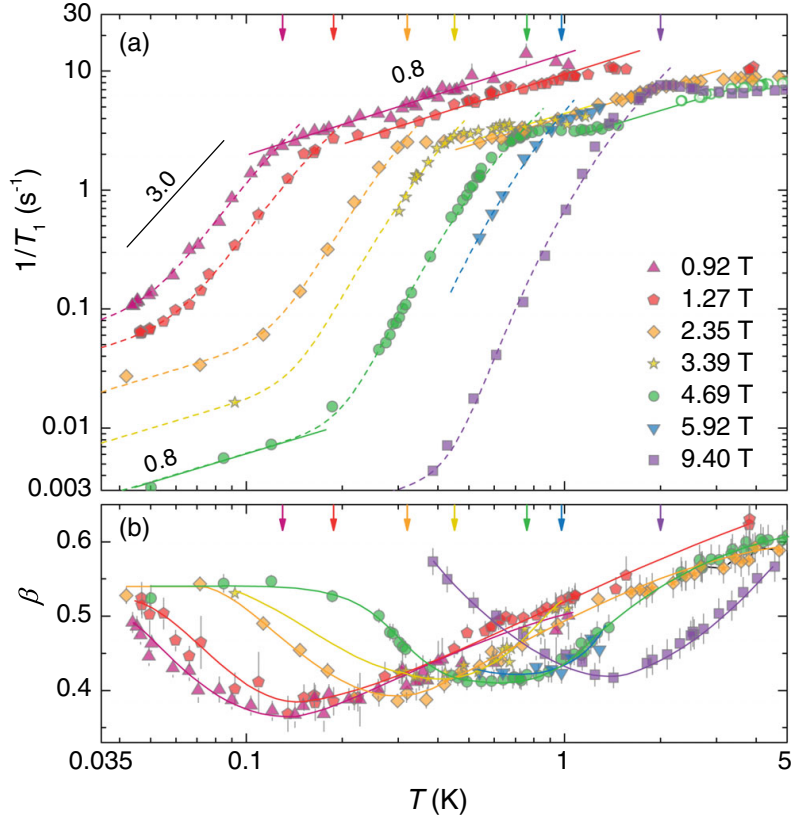


Figure 38. (a) Temperature dependence of the ${}^2\text{D}$ NMR spin-lattice relaxation rate $1/T_1$ in Zn-brochantite for various applied magnetic fields. The data show a gradual opening of a gap in the spinon excitation spectrum. (b) Stretching exponents β from the magnetization recovery curves, characterizing the distribution of relaxation times in the NMR experiment. Reproduced with permission from Ref. [407], copyright by the American Physical Society.

ries of experiments by M. Gomilšek *et al.* that combined local-probe techniques with neutron scattering [407, 409, 410]. Their μ SR measurements, performed down to 21 mK, revealed a considerable increase in the $1/T_1^\mu$ relaxation rate and the μ^+ Knight shift below ~ 5 K with a saturation below 0.6 K. In the ^2D NMR data, a nonmonotonic behavior of $1/T_1^{\text{NMR}}$ with anomalies around 15, 5, and 0.76 K and a power-law dependence at higher temperatures was observed. This led to a conclusion that two spin-liquid regimes, SL1 and SL2, are realized at different temperatures [409]. Neutron spectroscopy revealed an ω/T scaling behavior of the dynamic susceptibility at high temperatures [409], which can be explained by the proximity to a QCP driven by the magnetic anisotropy, as in the case of herbertsmithite. Additional NMR measurements, presented in Fig. 38, suggested that the gapless spin liquid is intrinsically unstable against spinon pairing (similar to Cooper pairing in superconductors) under the application of arbitrary small magnetic field, which opens a full or partial spin gap seen in the temperature dependence of the spin-lattice relaxation rate [407].

4.8. Claringbullite and barlowite: Three-dimensionally coupled kagomé planes

Mineral claringbullite, $\text{Cu}_4(\text{OH})_6\text{FCl}$ [411, 412], and its isostructural Br analogue barlowite, $\text{Cu}_4(\text{OH})_6\text{FBr}$ [413, 414], crystallize in a hexagonal structure (space group $P6_3/mmc$) in which 3/4 of the Cu atoms on the Cu(1) positions form structurally perfect kagomé planes with AA stacking, whereas the remaining 1/4 goes to the Cu(2) intersites. The presence of Cu^{2+} ions at interlayer positions determines the magnetic behavior of this systems at low temperatures by providing paths for ferromagnetic interlayer couplings [415]. The resulting 3D network of interactions, which is shown in Fig. 39, stabilizes a canted AFM ground state with the ordering temperature $T_N = 15.4$ K and a weak FM moment $\mu < 0.1\mu_{\text{B}}/\text{Cu}$. Several other phase transitions were reported at higher temperatures from specific-heat data. Magnetic susceptibility gives the Curie-Weiss temperature of $\Theta_{\text{CW}} = -136$ K [416].

The ferromagnetic coupling between the kagomé layers was initially assumed to be weak [416]. However, exchange parameters obtained from DFT and GGA+ U calculations indicate that the dominant interlayer exchange constant J_1 is either slightly larger or comparable to the nearest-neighbor AFM exchange on the kagomé triangles, $J_3 \approx 15.3$ meV [415]. A controversy exists about the magnitude of the DMI in barlowite and about the role played by the Cu(2) magnetic moments. At first, from the observed difference between the experimentally determined spin canting angle of $\sim 4.5^\circ$ and the orientation of the basal plane of the Cu octahedra, a substantial in-plane DMI of the order of $0.1J_3$ has been estimated [415]. The ferromagnetic moment, evidenced by a hysteresis in the magnetization, could be therefore naturally explained by the canted

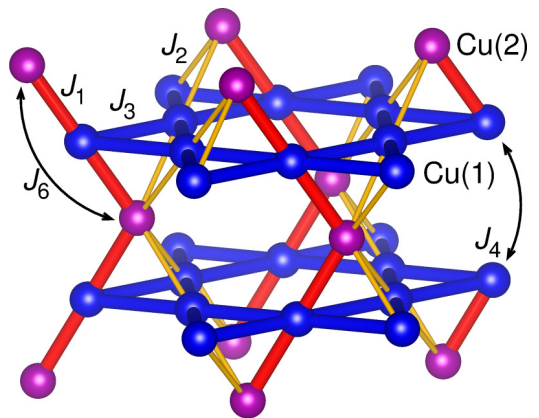


Figure 39. The model of 3D coupled kagomé planes that was proposed for barlowite. Reproduced with permission from Ref. [415], copyright by the American Physical Society.

AFM structure in the kagomé layers [229]. Another group, however, re-estimated the canting angle to a much smaller value $\leq 0.2^\circ$, which resulted in a vanishingly small DMI $\lesssim 0.006J$ [417]. They concluded that the ordered moment at $T \leq 15$ K might actually come from the interlayer spins, not excluding the possibility that the kagomé-lattice physics remains practically unaffected. Correspondingly, signatures of persistent spin dynamics within the ordered state were observed in the weak temperature dependence ($\propto T^{0.5}$) of the spin-lattice relaxation rate $1/T_1$, measured using $^{79,81}\text{Br}$ NMR [418].

While the details of the microscopic magnetic model of barlowite and claringbullite may require additional work to be settled, the main interest to these systems is motivated by the possibility to substitute nonmagnetic ions onto the Cu(2) sites [416, 419–423]. This should suppress the interlayer coupling and result in a system similar to herbertsmithite, but with much less structural disorder. If the interpretation of Han *et al.* [417] about the smallness of DMI is correct, one would end up with a KAFM compound that offers better conditions for the realization of a spin-liquid ground state. The feasibility of such a selective substitution of Cu(2) ions with Mg or Zn, as well as with larger Cd and Ca ions, has been systematically verified using first-principles calculations [419, 420]. The Mg- and Zn-substituted compounds were suggested as the best candidates due to the higher site selectivity and smaller lattice distortion. The first successful synthesis of Zn-barlowite, $\text{ZnCu}_3(\text{OH})_6\text{FBr}$, was soon demonstrated by Feng *et al.* [421], and the synthesis of Zn-claringbullite followed shortly afterwards [422]. These new compound show no magnetic order down to 50 mK and exhibit clear signatures of a spin gap in the uniform spin susceptibility obtained from ^{19}F NMR measurements. The magnetic-field dependence of the gap energy shows signatures of fractionalized spin- $\frac{1}{2}$ excitations, as one would expect for a topological quantum spin-liquid state. Most recently, Feng *et al.* [423] systematically investigated the evolution of magnetism in $\text{Cu}_{4-x}\text{Zn}_x(\text{OH})_6\text{FBr}$, bridging the two limiting cases of the 3D antiferromagnetism in barlowite ($x = 0$) and the spin-liquid physics in Zn-barlowite ($x = 1$). They found that the bulk AFM order is destroyed already around $x \approx 0.4$, while remnant magnetic correlations with a reduced transition temperature survive up to $x \approx 0.8$. This provides an opportunity to tune the system to a QCP that separates magnetic order from a spin-liquid phase.

5. Other layered quasi-2D lattices

5.1. The variety of two-dimensional crystal structures

The vast majority of quasi-2D crystals form regular periodic structures known as Archimedean lattices [216–218]. The simplest and most symmetric of them, built from identical regular polygons, derive from the well known triangular (T1), square (T2), and honeycomb (T3) tilings. Together with the kagomé (T8) lattice discussed in the previous chapter, they constitute the only four Archimedean tilings in which all NN bonds are equivalent. Triangular lattice, found in the minerals delafossite and mcconnellite, is an emblem of geometric frustration, where it occurs already in the simplest model with just a single AFM interaction on all NN bonds. In contrast, square and honeycomb lattices with only NN interactions are not geometrically frustrated, yet bond frustration may arise upon inclusion of further-neighbor exchange couplings [219, 238]. This

statement can be generalized to all 11 Archimedean lattices, shown in Fig. 40, of which only four are bipartite (i.e., consist of only even-sided regular polygons): square, honeycomb, square-hexagonal-dodecagonal (T10), and CaVO (T11). A magnetic square lattice is found, for example, in the mineral diaboleite, $\text{Pb}_2\text{Cu}(\text{OH})_4\text{Cl}_2$ [424]. The T10 lattice consists of squares, hexagons and dodecagons (hence the name, SHD) and has only been investigated theoretically [425], because no real material with this structure is known [216]. The name CaVO derives from the compound CaV_4O_9 , in which the T11 lattice, consisting of squares and octagons, is realized [426]. Some non-Archimedean periodic bipartite lattices, in particular the so-called dice lattice [427, 428], which is dual to the kagomé [283], have also been theoretically considered.

The remaining 7 lattices contain triangles and are therefore geometrically frustrated. The trellis (T5) lattice with its pronounced unidirectional structure can be considered as an arrangement of coupled two-leg spin ladders, which tend to dimerize across the rungs by forming singlets, if the exchange interactions on the rung bonds are sufficiently strong. This model is realized in the AV_2O_5 vanadates and in hollandite-type compounds [429] that are isostructural to the mixed-valent manganese mineral hollandite, $\text{BaMn}_8\text{O}_{16}$ [430]. The T6 lattice got its name from the layered material $\text{SrCu}_2(\text{BO}_3)_2$ [77, 78] and is essentially equivalent to the Shastry-Sutherland lattice discussed in chapter 2. As it was already mentioned in section 4.1, the kagomé (T8) and star (T9) lattices with only Heisenberg-type AFM interactions on NN bonds have no semiclassical ordered ground states because of a combination of strong frustration with low coordination number. In contrast, the triangular AFM lattice and all other Archimedean lattices order in the classical limit [216, 217]. Among them, the maple-leaf (T4) lattice, which results from a 1/7 site depletion of the triangular lattice, is intermediate from a frustration viewpoint between the triangular and kagomé lattices and is thought to be very close to the classically disordered ground state [431]. In spite of its complexity, this lattice is realized in synthetic iron phosphonates [432] and in the naturally occurring copper minerals spangolite, $\text{Cu}_6\text{Al}(\text{SO}_4)(\text{OH})_{12}\text{Cl} \cdot 3\text{H}_2\text{O}$ [433]; sabelliite, $\text{Cu}_2\text{ZnAsO}_4(\text{OH})_3$ [434]; fuettererite, $\text{Pb}_3\text{Cu}_6\text{TeO}_6(\text{OH})_7\text{Cl}_5$ [435]; and the most recently discovered bluebellite, $\text{Cu}_6\text{IO}_3(\text{OH})_{10}\text{Cl}$, and mohaveite, $\text{Cu}_6\text{TeO}_4(\text{OH})_9\text{Cl}$ [436] (for a review, see Ref. [351]).

Finally, the bounce (T7) lattice can be seen as a bond-depleted modification of the maple-leaf lattice. Indeed, the two lattices can be considered as limiting cases of a more general spin model with unequal J_1 and J_2 interactions on bonds that

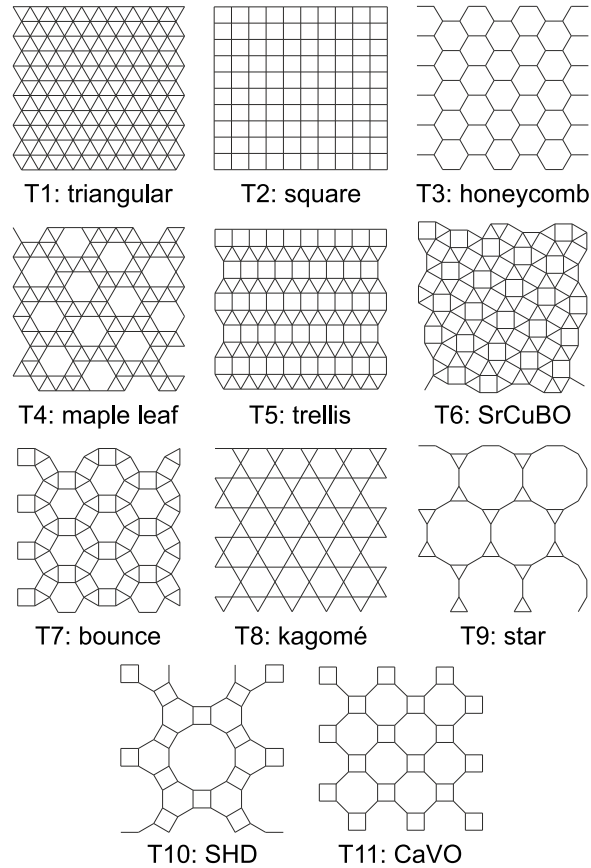


Figure 40. The 11 Archimedean tilings, after Refs. [216, 217].

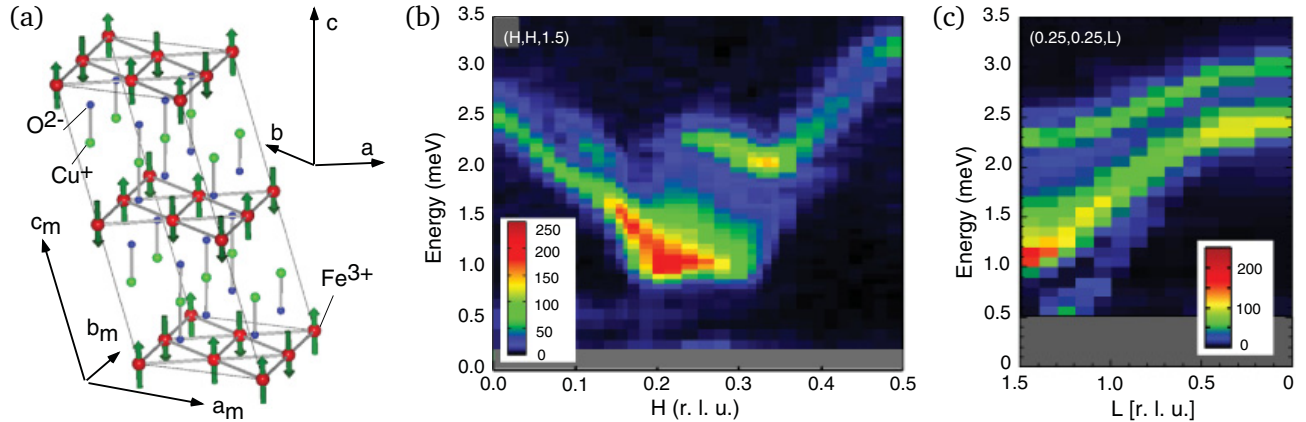


Figure 41. (a) The four-sublattice magnetic structure of delafossite, CuFeO₂ [445, 446]. (b, c) INS intensity maps along the $(HH\frac{3}{2})$ and $(\frac{1}{4}\frac{1}{4}L)$ directions in momentum space [456]. Reproduced with permission from Ref. [457], copyright by the American Physical Society.

separate neighboring triangles [216, 437]. The maple-leaf limit is realized for $J_2/J_1 = 1$, while the bounce lattice corresponds to $J_2/J_1 = 0$. Although these “pure” limits both have magnetically ordered ground states, the generalized model exhibits a quantum-critical transition at $\alpha_c = J_2/J_1 \approx 1.45$ to a quantum orthogonal-dimer singlet state without magnetic long-range order [437]. In this regime, application of magnetic field would result in magnetization plateaus, similar to those found in the Shastry-Sutherland or triangular-lattice models [216].

5.2. Delafossite and mconnellite: Classical spins on the triangular lattice

The delafossite group of minerals serves as a perfect realization of the triangular magnetic lattice. The hexagonal delafossite structure (space group $R\bar{3}m$) derives from the cubic rocksalt (NaCl) structure, if two different cations statistically distributed on the cation site undergo an order-disorder transition, segregating into alternate (111) planes to form a layered structure [438, 439]. In the minerals delafossite, CuFeO₂ [440], and mconnellite, CuCrO₂ [441], that share this crystal structure, the magnetic Fe³⁺ ($S = 5/2$) and Cr³⁺ ($S = 3/2$) ions form a perfect triangular lattice separated by nonmagnetic monovalent Cu⁺ layers. The magnetic order in CuFeO₂ and CuCrO₂ has been known since several decades [442–447]. In CuFeO₂, two magnetic transitions at $T_{N1} \approx 16$ K and $T_{N2} \approx 11$ K were observed in neutron diffraction, and a collinear up-up-down-down AFM ground state with spins parallel to the c axis, as shown in Fig. 41 (a), was proposed [445–447]. Two magnetic phase transition at $T_{N1} \approx 24.2$ K and $T_{N2} \approx 23.6$ K are also observed in CuCrO₂. However, this compound exhibits a noncollinear incommensurate spin helix below $T_N \approx 24$ K, propagating in the $[HH0]$ direction, with moments lying in the $[HHL]$ plane [448, 449]. The formation of this spin-spiral structure is associated with magnetoelectric effects [450–453]. In CuFeO₂, similar noncollinear order and ferroelectric behavior can be induced by partial Al substitution on the Fe site [454, 455].

In high magnetic fields applied parallel to the c axis, delafossite undergoes a sequence of first-order metamagnetic phase transitions at $B_{c1}^{\parallel} \approx 7$ T, $B_{c2}^{\parallel} \approx 13$ T, $B_{c3}^{\parallel} \approx 20$ T, and $B_{c4}^{\parallel} \approx 34$ T, seen as sharp magnetization steps with a hysteretic behavior [458, 459]. The nearly flat plateau

regions in between correspond to different magnetic phases, labeled I_{\parallel} , II_{\parallel} , III_{\parallel} , IV_{\parallel} , and V_{\parallel} . In particular, the $1/5$ magnetization plateau, corresponding to the phase III_{\parallel} , is consistent with the $\uparrow\uparrow\downarrow\downarrow$ type of magnetic order, while the $1/3$ magnetization plateau in phase IV_{\parallel} can be attributed to an $\uparrow\uparrow\downarrow$ (up-up-down) spin arrangement [459, 460]. The intermediate phase II_{\parallel} is a noncollinear incommensurate spin spiral [461]. As noted by Haraldsen *et al.* [462], these metamagnetic transitions, driven either by magnetic field or chemical substitution, can arise from spin-wave instabilities that are preceded by the softening of spin-wave modes at the would-be ordering wave vectors. Indeed, neutron-spectroscopy measurements in the collinear AFM state of CuFeO_2 revealed two local minima in the spin-wave dispersion that coincide with the incommensurate ordering wave vectors of its $\text{CuFe}_{1-x}\text{Al}_x\text{O}_2$ daughter compound [463–465]. These soft modes can be also recognized in Fig. 41 (b).

The spin model that was initially proposed to describe the magnetic interactions in CuFeO_2 included four Heisenberg-type exchange interactions and a single-ion anisotropy term [466]. From a global fit of this model to the INS data, Ye *et al.* [465] obtained the experimental estimates for the in-plane AFM interactions $J_1 \approx 1.14$ meV, $J_2 \approx 0.50$ meV, $J_3 \approx 0.65$ meV, the out-of-plane coupling $J_z \approx 0.33$ meV, and the single-ion anisotropy $D \approx 0.17$ meV. In the theoretical phase diagram of an Ising-spin triangular-lattice antiferromagnet [468], these parameters fall within the region of the 4-sublattice $\uparrow\uparrow\downarrow\downarrow$ phase, which is consistent with the ground state of CuFeO_2 . However, follow-up single-crystal neutron scattering data measured in a single-domain AFM state, obtained by “detwinning” a single crystal under a small uniaxial pressure [456, 457], revealed considerable deviations from this model. A selection of these INS data is reproduced in Fig. 41. This discrepancy has been attributed to the effect of spin-lattice coupling, manifested in the weak trigonal-to-monoclinic lattice distortion that takes place below T_N [469, 470]. In particular, the low-energy spin-wave mode at the AFM zone center is split into two branches that were observed previously in ESR studies in zero magnetic field [458, 471]. Moreover, the higher-energy branch cannot be reproduced by spin-wave calculations and was attributed to an electromagnon excitation [472]. To describe the dispersion of this electric-field-active magnon mode, coupling to lattice or charge degrees of freedom must be considered. This led T. Nakajima *et al.* [457] to propose a more elaborate spin model that takes into account the spin-driven lattice distortion and can successfully de-

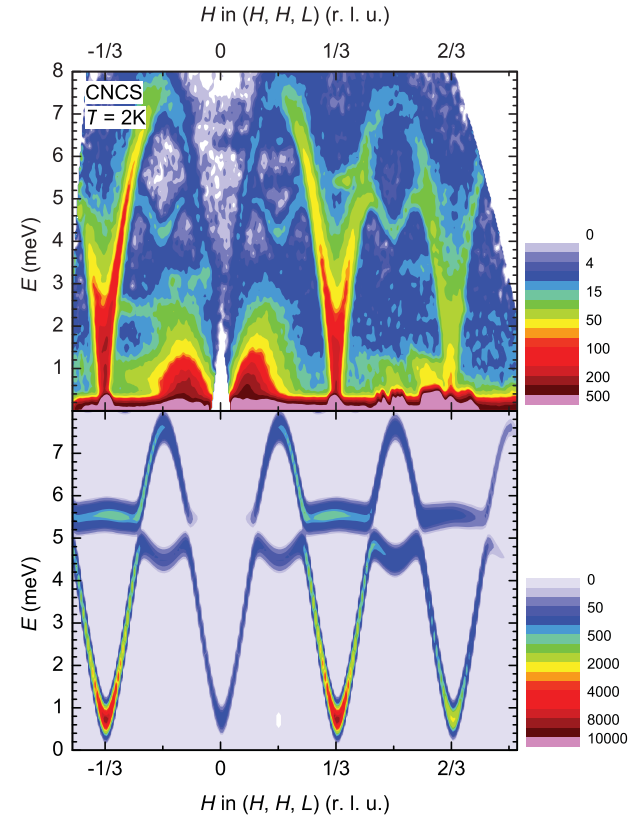


Figure 42. Spin waves in mcnellite, measured on a synthetic single crystal, in comparison to the results of a spin-wave calculation. Reproduced with permission from Ref. [467], copyright by the American Physical Society.

scribe the available INS measurements. In this model, every exchange interaction J_i is split into J_i and J'_i , and the NN interaction J_1 into J_1 , J'_1 , and J''_1 , to account for a distortion of the triangular lattice that arises as a result of the structural transition. In addition to the single-ion anisotropy D , a small in-plane anisotropy $E \approx 0.035$ meV has been also included. From a fit to the experimental data, the largest effect that the monoclinic distortion has on the splitting of exchange constants was observed for the NN interaction, with $J_1 \approx 0.455$ meV, $J'_1 \approx 0.422$ meV, and $J''_1 \approx 0.150$ meV. This example illustrates that even a slight structural distortion of less than 0.4% [469, 470] can cause a threefold difference in the initially equivalent exchange parameters, effectively lifting the vast degeneracy of the strongly frustrated triangular lattice.

In the isostructural CuCrO_2 , the spin-wave spectrum has been also mapped out on synthetic single crystals by Poienar *et al.* [473] and Frontzek *et al.* [467]. In contrast to CuFeO_2 , this ferroelectric compound undergoes no structural phase transition across T_N , hence the J_1 - J_2 - J_3 - J_z model, supplied with D_x and D_z anisotropy terms, can successfully describe the whole excitation spectrum, as shown in Fig. 42. The much larger NN interaction $J_1 \approx 2.8$ meV, as compared to CuFeO_2 , reduces the D/J_1 ratio and the influence of further-neighbor interactions, stabilizing a proper-screw magnetic structure with a nearly commensurate $(\frac{1}{3}-\delta \frac{1}{3}-\delta 0)$ propagation vector [448, 449] that became known as the incommensurate “Y state” [474]. Application of high magnetic fields leads to the appearance of multiple field-induced magnetic phases in CuCrO_2 that have been investigated both experimentally and theoretically [453, 474]. For an in-plane magnetic field, $\mathbf{B} \perp \mathbf{c}$, a transition from a proper-screw to a cycloidal-spiral phase occurs at $B_f \approx 5.3$ T. For fields applied parallel to the c axis, a sequence of metamagnetic transitions has been observed at much higher fields exceeding 40 T. These high-field phases include a noncoplanar umbellate spin structure, a commensurate Y state, and a collinear up-up-down phase [474].

In a more recent neutron-spectroscopy work, Park *et al.* [475] investigated the high-energy part of the spin-wave spectrum of CuCrO_2 , above the energy range covered in previous studies [467, 473]. They found an additional collective mode around 12.5 meV that has a mixed magnon-phonon character. As in the case of CuFeO_2 , the spin-lattice coupling has a substantial influence on the magnetic excitations, and the inclusion of exchange-striction effects in the theoretical model can accurately capture the new features of the INS data [475]. Kajimoto *et al.* [476] also pointed out the presence of a diffusive quasielastic component in the neutron-scattering spectrum with a characteristic momentum dependence. This component appears only at elevated temperatures and presumably originates from scattering on uncorrelated triangular clusters that persist both above and below the magnetic ordering temperature. This feature could be generic for triangular-lattice antiferromagnets.

Finally, it is worth noting that the mineral crednerite, CuMnO_2 [477], is the $S = 2$ analog of delafossite. However, it crystallizes in a lower-symmetry monoclinic ($C2/m$) structure that undergoes a spin-driven transition to a triclinic $C\bar{1}$ phase as magnetic order sets in at $T_N \approx 65$ K. The monoclinic symmetry of the lattice is due to a Jahn-Teller distortion of the Mn^{3+} ($t_{2g}^3 e_g^1$) cation that lifts the e_g orbital degeneracy [478, 479], deforming the lattice so that it forms isosceles-triangle layers with reduced frustration. Upon the formation of the collinear AFM order with propagation vector $(-\frac{1}{2} \frac{1}{2} \frac{1}{2})$, strong magnetoelastic coupling [480, 481] relieves the remaining frustration through the monoclinic-to-triclinic transition. Damay *et al.* [478] therefore argued that

the magnetism in CuMnO_2 , with largely different exchange interactions on the sides of isosceles triangles, is better considered in the framework of a frustrated square-lattice model with a nearest-neighbor coupling J_1 and a diagonal interaction J_2 . For $J_2/J_1 > 1/2$, this model is known to stabilize the collinear AFM phase, assisted by any arbitrarily weak coupling to the lattice [482]. Powder neutron-spectroscopy measurements revealed a large low-temperature spin-wave gap of about 6 meV, comparable with the ordering temperature, and persistent 2D short-range magnetic correlations [483].

For the sake of completeness, it should be noted that a triangular lattice of $\frac{5}{2}$ -spins is also realized in the mineral yavapaiite, $\text{KFe}(\text{SO}_4)_2$ [484, 485]. However, in this particular mineral the exchange coupling along one side of the triangles (J') is larger than along the two others (J) due to a monoclinic distortion, so that it actually represents a realization of the so-called row model [486]. Nevertheless, instead of the theoretically expected helical spin structure, predicted for the row model with $J'/J > 1/2$ in zero magnetic field, yavapaiite realizes a more complex sine-wave modulated phase with the same wave vector as a result of substantial magnetic anisotropy. In contrast, its synthetic analogs $\text{RbFe}(\text{SO}_4)_2$ and $\text{CsFe}(\text{SO}_4)_2$ that crystallize in the trigonal structure (space group $P\bar{3}$) have equal magnetic bonds and were studied as realizations of classical-spin triangular lattices with the expected 120° helical spin structure [485, 487–489].

5.3. Devilline: Distorted spin- $\frac{1}{2}$ triangular lattice

Among the quasi-2D layered compounds, the monoclinic copper sulphate-hydroxide mineral devilline, $\text{CaCu}_4(\text{SO}_4)_2(\text{OH})_6 \cdot 3\text{H}_2\text{O}$ [490], represents a remarkable realization of somewhat distorted and corrugated triangular-lattice layers, well separated by nonmagnetic spacers. Each copper ion, in a 4+2 coordination, is linked by six edges to its neighbors, forming $[\text{Cu}_2(\text{OH})_3\text{O}]^\infty$ sheets parallel to (100), as shown in Fig. 43. Adjacent sheets are connected by calcium ions in sevenfold coordination, by SO_3^{2+} tetrahedra, and by a system of hydrogen bonds. The large unit cell of devilline contains eight inequivalent Cu sites, and the distortions within the sheets lead to a variation in the Cu–Cu distances ranging from 3.04 to 3.27 Å. This mineral has a Pb analogue lautenthalite, $\text{PbCu}_4(\text{SO}_4)_2(\text{OH})_6 \cdot 3\text{H}_2\text{O}$ [491], along with several other close structural relatives: $\text{Cu}_5(\text{SO}_4)_2(\text{OH})_6 \cdot 4\text{H}_2\text{O}$ (kobyashevite) [492], $\text{Cu}_4\text{Mn}^{2+}(\text{SO}_4)_2(\text{OH})_6 \cdot 4\text{H}_2\text{O}$ (campigliaite) [493], $\text{Cu}_4\text{Cd}(\text{SO}_4)_2(\text{OH})_6 \cdot 4\text{H}_2\text{O}$ (niedermayrite) [494], $\text{Cu}_4\text{Zn}(\text{SO}_4)_2(\text{OH})_6 \cdot 6\text{H}_2\text{O}$ (ktenasite) [495], and $\text{Cu}_4\text{Ca}(\text{SO}_4)_2(\text{OH})_6 \cdot 3\text{H}_2\text{O}$ (serpierite) [496]. For a comparative analysis of the structure and crystal chemistry of sulfate minerals, an interested reader can refer to recent reviews [497, 498].

So far, experimental realizations of the quantum spin- $\frac{1}{2}$ triangular lattice have been proposed only in $\text{Ba}_3\text{CoSb}_2\text{O}_9$ [500–503] or in rare-earth compounds, such as YbMgGaO_4 [504–511] or Yb-delafoissites [512, 513], where due to a large crystal-field splitting, the ground-state Kramers doublet is well separated from higher-energy multiplets and can be considered as an effective $S = 1/2$ state at sufficiently low temperatures. The high current interest in spin- $\frac{1}{2}$ triangular-lattice magnets is dictated by the reports proposing that it may support a quantum spin-liquid ground state [514, 515]. It is therefore highly desirable to find an implementation of the real spin- $\frac{1}{2}$ triangular lattice in cuprates, and devilline-group minerals can be a perfect starting point in this search. Some of them, e.g. niedermayrite or ktenasite, have more symmetric crystal structures, and

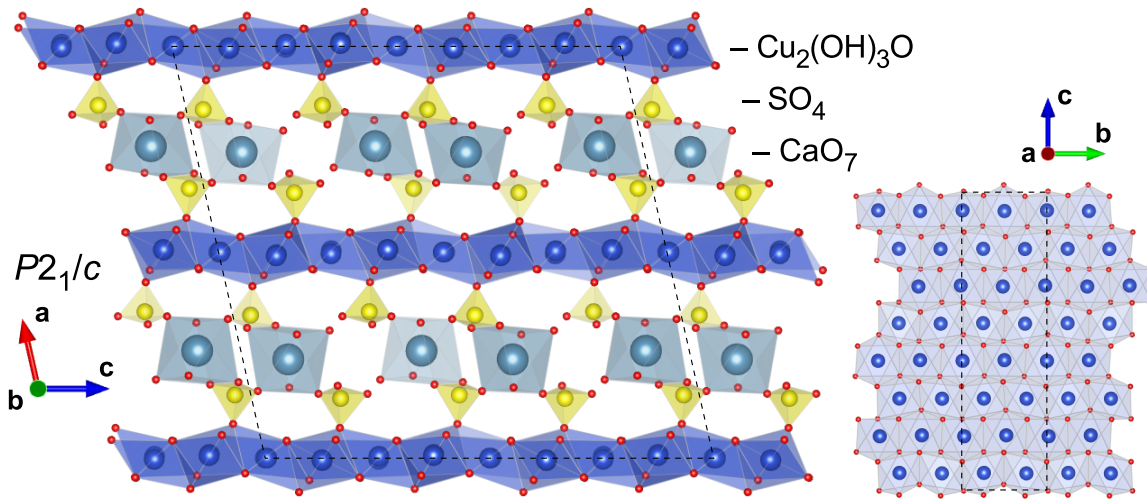


Figure 43. The crystal structure of devilline, visualized according to the results of structural refinement from Ref. [490] using VESTA software [499]. A fragment of the $\infty^2[\text{Cu}_2(\text{OH})_3\text{O}]^-$ sheet, viewed along the a axis, is shown at the right. The dashed lines outline the unit cell.

the unavoidable distortions in the copper planes vary depending on the composition. It would be worthwhile to estimate numerically, to what extent the interaction network in these compounds is affected by the distortions of the triangular-lattice copper layers, and whether these distortions are sufficiently weak to preserve the underlying physics. Low-temperature magnetic characterization measurements on these minerals would also be highly desirable.

A very similar triangular-lattice layered structure has been reported in two polymorphs of the copper hydroxyl nitrate $\text{Cu}_3(\text{NO}_3)(\text{OH})_3$, gerhardtite and rouaite. These compounds have been successfully synthesized [517], which should hopefully enable their low-temperature investigations in the near-future. The hydrated version of the same compound, known as the mineral likasite, $\text{Cu}_3(\text{NO}_3)(\text{OH})_5 \cdot 2\text{H}_2\text{O}$, can also represent interest as a realization of frustrated one-dimensional chains consisting of corner-sharing tetrahedra of Cu^{2+} ions [518].

Another highly symmetric layered structure with a triangular motif in the copper planes is realized in the trigonal sulphate mineral schulenbergite, $\text{Cu}_7(\text{SO}_4)_2(\text{OH})_{10} \cdot 3(\text{H}_2\text{O})$ [516]. Here the layers represent strongly distorted triangular-lattice planes, in which every unit cell contains equilateral triangles of different sizes, which are expected to be the source of geometric frustration. Cu atoms occupy two inequivalent Wyckoff sites: Cu(1) is shared by two larger triangles and one smaller triangle, whereas Cu(2) sits in the center of the hexagon formed by six larger triangles, as shown in Fig. 44.

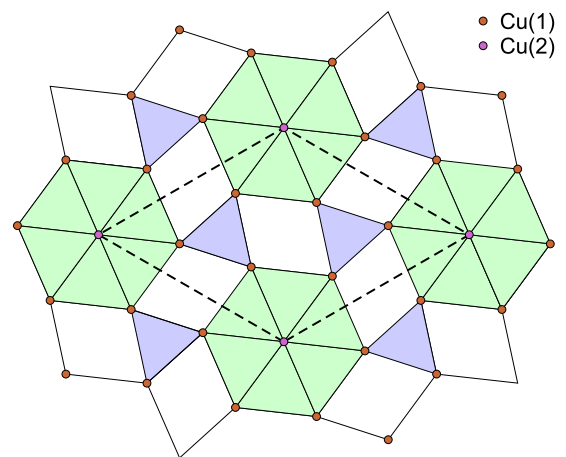


Figure 44. The structure of magnetic copper layers in schulenbergite, viewed along the trigonal axis, after Ref. [516]. Circles represent Cu atoms, two types of equilateral triangles are highlighted with color. The dashed lines outline the unit cell.

5.4. Spangolite: A maple-leaf lattice antiferromagnet

As already mentioned previously, there is a handful of naturally occurring copper minerals, some of them discovered only recently, that realize the spin- $\frac{1}{2}$ magnetic maple-leaf (T4) lattice [351]. Surprisingly, this complex lattice appears to be more common in the mineral world than its prototype triangular (T1) lattice. However, none of these minerals has been so far grown artificially in the form of single crystals, and the number of published low-temperature studies of their magnetic properties remains very limited. In 2011, Fennell *et al.* [519] presented the results of a structural and basic magnetic characterization of the layered hydrated copper sulfate mineral spangolite, $\text{Cu}_6\text{Al}(\text{SO}_4)(\text{OH})_{12}\text{Cl} \cdot 3\text{H}_2\text{O}$, which is found in the form of finely grained thin turquoise plates. For the purpose of physical characterization, they chose a natural specimen from the Blanchard mine, Socorro, Colorado. The refinement of both powder and single-crystal x-ray diffraction data resulted in a structure with the trigonal space group $P3_1c$, consisting of well separated slightly distorted triangular-lattice layers in which 1/7 of the Cu^{2+} ions are replaced with nonmagnetic Al^{3+} . The resulting magnetic superlattice is very close to a maple-leaf lattice with a small distortion that separates the magnetic ion positions into two structurally inequivalent sites, arranged in two sets of pure trimers as shown in Fig. 45.

The application of GKA rules to the spangolite structure suggests that the superexchange interactions J_1 and J_2 within both trimers must be antiferromagnetic, resulting in a strong frustration [519]. The trimers are coupled with AFM interactions J_3 , J_4 , and a FM interaction J_5 along different exchange paths shown in Fig. 45 (b).

Measurements of the magnetic susceptibility show a broad maximum around 50 K that is typical of a spin-dimer system. No signs of magnetic ordering were seen down to 0.1 K, despite the high Curie-Weiss temperature of $\Theta_{\text{CW}} = -38$ K. The effective magnetic moment obtained from the susceptibility was $4.55 \mu_{\text{B}}/\text{f.u.}$, that is significantly reduced from the anticipated value of $10.39 \mu_{\text{B}}/\text{f.u.}$ for one formula unit with six Cu^{2+} spins. From the low-temperature Curie tail, a $\sim 7.5\%$ population of defective spins in the natural spangolite specimen could be estimated. The existing experimental evidence strongly suggests that spangolite has a singlet ground state, yet the microscopic details of its formation still await to be clarified.

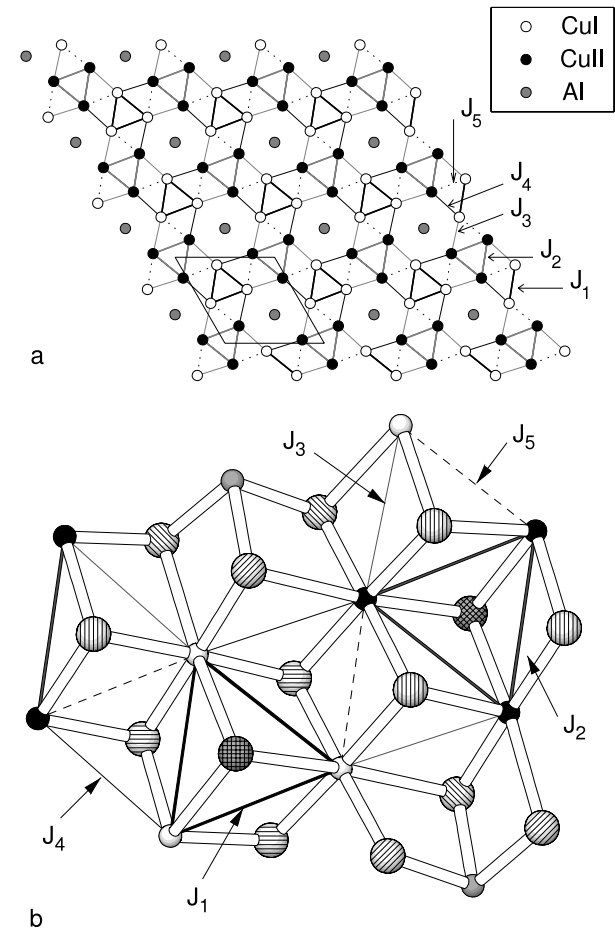


Figure 45. (a) The structure of distorted maple-leaf layers in spangolite. (b) The five magnetic interactions acting within (J_1 , J_2) and between (J_3 , J_4 , J_5) the trimers. Reproduced with permission from Ref. [519]. Copyright by IOP Publishing Ltd.

The presence of two inequivalent sublattices in spangolite certainly represents an unnecessary complication that may prevent this mineral from playing the desired role of the model system for the realization of theoretically proposed models on the perfect maple-leaf lattice [431, 437]. It has been noted [519] that the emerald-green mineral sabelliite, $\text{Cu}_2\text{ZnAsO}_4(\text{OH})_3$, with a single-sublattice maple-leaf lattice of Cu^{2+} ions [434] could be a better candidate for this role. Other minerals with the same structural motif are fuettererite [435], bluebellite, and mojaveite [436], whose detailed magnetic characterization would be definitely desirable.

5.5. Diaboleite: A spin- $\frac{1}{2}$ square lattice without frustration

The tetragonal mineral diaboleite, $\text{Pb}_2\text{Cu}(\text{OH})_4\text{Cl}_2$ [520], forms a defect perovskite-related structure of quasi-2D Cu^{2+} square-lattice planes with the dominant AFM coupling, $J_1 \approx 3.3$ meV, on the NN bonds and a much weaker NNN coupling, $J_2 \approx 0.04$ meV [424]. The layers are weakly interacting via two interlayer exchange constants, $J_\perp \approx 0.086$ meV and $J'_\perp \approx 0.034$ meV, which stabilize an AFM-ordered state below $T_N \approx 11$ K. The material is therefore analogous to the layered perovskite PbVO_3 , which is also characterized by AFM interactions, yet with a much larger J_2/J_1 ratio of ~ 0.35 , close to the critical region of the J_1 - J_2 frustrated square lattice [521, 522]. In contrast, the negligibly small J_2 in diaboleite essentially deprives it of magnetic frustration.

Application of high magnetic fields leads to a monotonic increase in the ordering temperature, as shown in Fig. 46, which is typical among square-lattice antiferromagnets [522–524]. A recent theoretical study [525] also estimated the g factors of $\text{Pb}_2\text{Cu}(\text{OH})_4\text{Cl}_2$ for fields parallel and perpendicular to the planes, which showed a sizeable anisotropy in the g factor of about 14%.

In natural diaboleite crystals, powder x-ray diffraction and chemical analysis revealed the presence of stacking faults and about 5–10% of copper vacancies [424]. They lead to local structural distortions, but do not disrupt the couplings between the remaining Cu sites. While the magnetic transition remains sharp, the vacancies influence the low-temperature behavior of the magnetic susceptibility below the broad hump seen around 30 K.

As one can see, in spite of the model character of diaboleite that serves as an example of the textbook square-lattice model with just a single dominant AFM interaction J_1 , the low-temperature physical measurements on this mineral remain limited. One can therefore expect that it will draw more interest in future as a subject for more detailed studies using neutron spectroscopy and local magnetic probes.

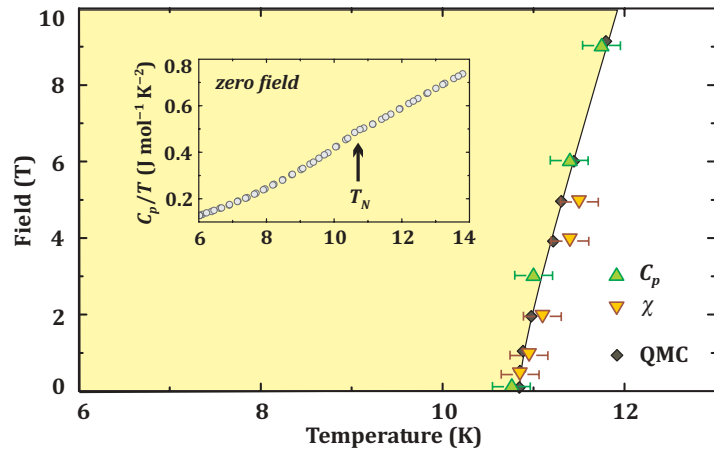


Figure 46. Magnetic-field dependence of the Néel temperature in diaboleite from QMC simulations, specific heat, and magnetic susceptibility measurements. Reproduced with permission from Ref. [424]. Copyright by the American Physical Society.

5.6. Shattuckite: A combination of CuO_2 planes and ribbons

Another layered mineral that fell under recent scrutiny is shattuckite, $\text{Cu}_5(\text{SiO}_3)_4(\text{OH})_2$ [526]. It forms blue translucent crystals with an orthorhombic structure (space group $Pcab$) that contains corrugated CuO_2 planes separated by twisted CuO_2 ribbons. This combination of 2D and 1D structural motifs results in a complex weakly frustrated network of magnetic interactions. Below the magnetic ordering temperature, $T_N = 7$ K, an AFM order with a weak FM canting has been reported. The spin canting results in hysteresis loops in the magnetization with a small spontaneous magnetization of $0.075 \mu_B/\text{f.u.}$ [527]. At higher magnetic fields, no evidence for a spin-flop transition was evidenced up to 9 T. The AFM transition can be also seen in specific heat as a rounded maximum, which broadens and shifts to slightly higher temperatures in magnetic field.

From the temperature dependence of the magnetization in the paramagnetic state, the Curie-Weiss temperature of -13.5 K and the Curie constant of 2.23 emu K/mol have been estimated [527]. An electron paramagnetic resonance characteristic of Cu^{2+} ions with a weakly anisotropic g -factor, $(g_{\parallel} - g_{\perp})/g_{\perp} \approx 0.06$, was observed on a powder sample obtained by grinding a natural shattuckite mineral from Kaokoveld Plateau, Namibia [527]. A higher value of the g -factor anisotropy, $(g_{\parallel} - g_{\perp})/g_{\perp} \approx 0.18$, was reported in an earlier study on a sample from Ajo, Arizona, USA [528]. These results suggest that the ground state of the Cu^{2+} ion corresponds to the unpaired $d_{x^2-y^2}$ orbital in a tetragonal crystal field imposed by the distorted square planar environment of oxygen ligands. The experimental crystal-field parameters calculated from the positions of optical absorption bands can be found in Ref. [528], where they are compared to those of azurite, malachite, chalcanthite, and plancheite. The optical and ESR spectra of shattuckite have been later calculated theoretically [529], yielding a satisfactory match to the experimentally measured g -factors and optical absorption transitions.

To estimate the relevant magnetic interactions in shattuckite, A. V. Koshelev *et al.* performed electronic-structure calculations in the framework of a self-consistent spin-polarized DFT [527].

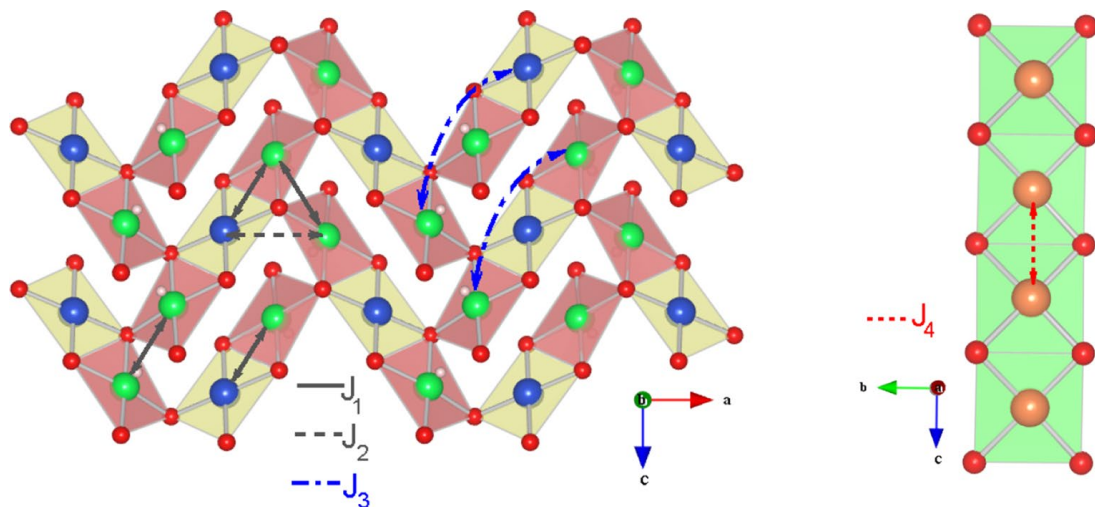
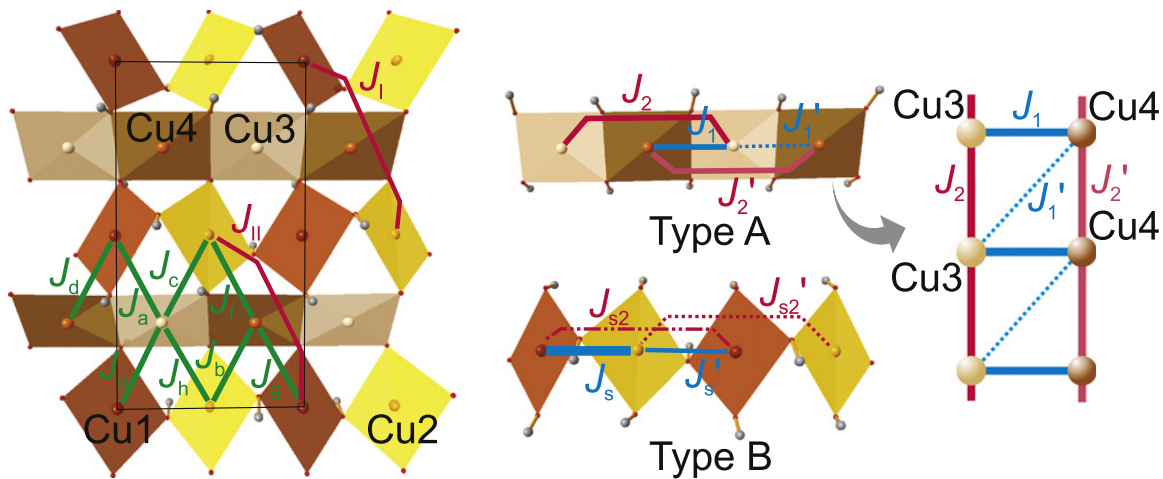


Figure 47. Exchange paths for magnetic interactions within the CuO_2 square planes (left) and twisted CuO_2 ribbons (right) in shattuckite. Reproduced with permission from Ref. [527], copyright by Springer-Verlag.

Their spin model is illustrated in Fig. 47. There are three structurally inequivalent magnetic Cu sites in the crystal structure, of which Cu(1) and Cu(2) form a corrugated layer of edge-sharing and corner-sharing CuO₄ plaquettes, while Cu(3) ions form edge-sharing ribbons running along the **c** direction that are connected by nonmagnetic SiO₄ tetrahedra along the **b** axis. All dominant exchange interactions within the planes are reportedly antiferromagnetic: $J_1 \approx 14$ meV, $J_2 \approx 6$ meV, and $J_3 \approx 3$ meV. On the other hand, the NN interaction $J_4 \approx -1$ meV within the ribbons is ferromagnetic and weak, comparable with the $J_5 \approx -1$ meV coupling between the chains and the layers. However, the mutual cancelation of J_5 interactions due to symmetry considerations virtually decouples the chains from the layers. Similarly, the interchain Cu(3)–Cu(3) interaction was estimated to be very small (beyond the accuracy limit of DFT), but could tentatively stabilize a long-range AFM order on the Cu(3) sublattice. The presented hierarchy of exchange parameters allows us to classify the shattuckite mineral as a quasi-2D magnetic system with weak frustration. The competing J_2 interaction between Cu(1) and Cu(2) ions in the neighboring corner-sharing plaquettes and the further-neighbor interaction J_3 are too weak to introduce significant frustration to the system. As a result, the AFM structure resulting from these interactions alone would remain collinear. The most likely origin of the weak ferromagnetism at $T < T_N$ is due to the DMI along the Cu(1)–O–Cu(1) and Cu(1)–O–Cu(2) pathways within the planes that are allowed by symmetry and may lead to a small spin canting, according to Ref. [527].

5.7. Langite and Wroewolfeite: Coexistence of magnetic order and quantum disorder

There are two naturally occurring polymorphs of the layered hydrated copper hydroxyl sulphate mineral Cu₄(OH)₆SO₄ · 2H₂O: langite (space group *Pc*) [531, 532] and wroewolfeite (space group *Pm*) [533, 534]. Both consist of weakly coupled two-dimensional magnetic layers composed of alternating edge- and corner-sharing copper chains, separated by sulphate groups and water molecules. The structure is therefore similar to that of brochantite, but with a larger interlayer separation that determines the quasi-2D magnetic behavior. The same structural layer units



are also found in the mineral posnjakite, $\text{Cu}_4(\text{OH})_6\text{SO}_4 \cdot \text{H}_2\text{O}$ [535], to which wroewolfeite is converted upon loss of water. Wroewolfeite has been synthesized artificially [536], but its magnetic properties were not yet systematically investigated. This may be partly due to the metastability of both posnjakite and wroewolfeite phases, which readily lose water and are converted to brochantite under unfavorable conditions [536, 537].

Meanwhile, the langite structure has been recently addressed by Lebernegg *et al.* [530]. Its magnetic layers contain four structurally inequivalent Cu sites, of which Cu(1) and Cu(2) form slightly buckled corner-sharing CuO_4 chains, whereas Cu(3) and Cu(4) form linear edge-sharing CuO_4 chains. Langite orders antiferromagnetically below a Néel temperature of $T_N \approx 5.7$ K as a result of a complex frustrated network of exchange interactions shown in Fig. 48. On the one hand, the edge-sharing (type A) chains are formed by four AFM interactions: the NN couplings $J_1 \approx 3.3$ meV and $J'_1 \approx 0.8$ meV between Cu(3) and Cu(4) ions and two nearly equal NNN interactions $J_2 \approx J'_2 \approx 3.1$ meV on the Cu(3)–Cu(3) and Cu(4)–Cu(4) bonds. This makes this chain equivalent to an AFM ladder model with legs formed by Cu(3) and Cu(4) ions, connected by J_1 rungs and a much weaker diagonal exchange interaction J'_1 , as shown schematically in Fig. 48 (right panel). On the other hand, the corner-sharing (type B) chains are characterized by FM interactions $J_s \approx -6.4$ meV and $J'_s \approx -2.0$ meV. In addition, there are multiple interchain interactions $J_a \dots J_h$ with different signs, so that the chains are not independent, but form part of a complex 2D magnetic network. Specific-heat and magnetization data indicate that the spin lattice of langite splits into two sublattices with predominantly FM and AFM couplings at low temperatures [530]. The former develops long-range magnetic order with a saturation field of ~ 12 T, whereas the latter evades long-range magnetic order due to frustration. Lebernegg *et al.* argue that this separation into two magnetic sublattices must be generic for magnetic minerals that combine edge- and corner-sharing CuO_4 chains in their crystal structure.

6. Three-dimensional frustrated lattices

6.1. Magnetic frustration on 3D crystal lattices

While the majority of 3D spin systems tend to develop magnetic order at sufficiently low temperatures, signatures of magnetic frustration can be seen in the unusual behavior of their spin fluctuations, which are expected to be stronger than in the case of conventional ferro- or antiferromagnets. A separate matter of present-day interest in quantum magnetism is the search for magnetic systems that would display magnon fractionalization, resembling the emergence of spinon excitations in spin chains, but in a 3D network of magnetic interactions [59, 538–543]. One example of an actively studied 3D spin-liquid candidate with fractionalized excitations, $\text{PbCuTe}_2\text{O}_6$ [543–545], mimics the hyperkagomé structure of the natural mineral choloalite [546].

In three dimensions, the pyrochlore lattice plays a similar role to the triangular lattice in 2D, serving as the emblem of geometric frustration for AFM interactions between the nearest neighbors [547, 548]. It can be viewed as an arrangement of corner-sharing tetrahedra or as an alternating sequence of stacked kagomé and triangular layers. It is realized, for instance, in materials with the cubic pyrochlore or spinel (AB_2X_4) crystal structure, if the magnetic ion occupies

the *B* site [549]. In naturally occurring minerals, distorted pyrochlore lattices are realized, for instance, in atacamite and melanothallite, which will be discussed in the following. For isotropic Heisenberg interactions between the spins, magnetic frustration can arise either due to the AFM nearest-neighbor exchange coupling or because of the competition of nearest- and further-nearest-neighbor interactions. Inclusion of multiple exchange terms in the Hamiltonian may stabilize various ordered ground states, such as ferro- or antiferromagnetism, single- or multi- \mathbf{q} spin spirals, nematic order, or some more exotic phases [550–552]. In the presence of considerable single-ion anisotropy, noncollinear 2-in-2-out, 3-in-1-out or all-in-all-out spin configurations can be realized in every tetrahedron, resulting in AFM or spin-ice ground states [538, 553], among other possibilities. This field of research is definitely too broad and goes beyond the scope of the present review.

A regular 1/4 site depletion of the pyrochlore lattice can lead to the formation of the 3D hyperkagomé, apart from 2D kagomé or kagomé-staircase lattices [57, 554]. The hyperkagomé lattice and its relationship to the parent pyrochlore lattice are illustrated in Fig. 49. The spin- $\frac{1}{2}$ AFM nearest-neighbor Heisenberg model on the hyperkagomé lattice has been studied by various authors [556–561], who showed that it hosts a valence-bond crystal state due to geometric frustration. Inclusion of various anisotropic interactions or weak further-neighbor coupling terms lifts the massive degeneracy of the ground state and stabilizes various noncollinear and noncoplanar magnetic phases that compete in the phase diagram [562–567].

In many other 3D crystal structures, even in the absence of structural motifs supporting geometric frustration, bond frustration can still be present as a result of competing interactions. Moreover, frustration may arise due to anisotropic compass-type interactions [568], prominently manifested in the Kitaev-Heisenberg models [569–571] that were recently generalized to various tricoordinated 3D lattices [572–575].

6.2. Atacamite and other polymorphs of $\text{Cu}_2(\text{OH})_3\text{Cl}$: Distorted pyrochlore structure

Copper hydroxychloride, $\text{Cu}_2(\text{OH})_3\text{Cl}$, has multiple polymorphs and plays a central role in the field of quantum magnetism as the parent compound of the famous kagomé antiferromagnet herbertsmithite, $\text{ZnCu}_3(\text{OH})_6\text{Cl}_2$, and its relatives. These compounds, in which Zn replaces one quarter of the Cu atoms to stabilize the rhombohedral structure featuring kagomé planes [56], were discussed in chapter 4. Multiple polymorphic crystal forms of $\text{Cu}_2(\text{OH})_3\text{Cl}$ are known, including atacamite (orthorhombic, space group $Pnma$), paratacamite (rhombohedral, space group $R\bar{3}$), clinoatacamite, and botallackite (both monoclinic, space group $P2_1/n$). The structure of paratacamite was shown to be Zn-stabilized [268], so in fact it does not belong to the sequence

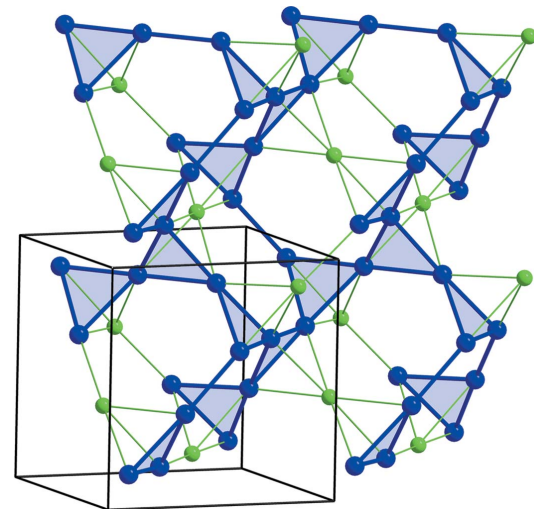


Figure 49. The hyperkagomé lattice (thick blue lines) and its relationship to the pyrochlore lattice (thin green lines). The cubic unit cell is shown in black. Reproduced from Ref. [555].

of pure copper-hydroxychloride phases according to the present consensus. The other three polymorphs form the so-called Ostwald cascade of metastable phases: botallackite–atacamite–clinoatacamite [576], whose relative stability is now well understood [577, 578]. Botallackite, or $\alpha\text{-Cu}_2(\text{OH})_3\text{Cl}$, represents an “ephemeral” phase that crystallizes first under most conditions, but quickly recrystallizes to the more stable polymorphs unless the solutions responsible for its crystallization are removed or dried out. It therefore represents the rarest of the naturally occurring $\text{Cu}_2(\text{OH})_3\text{Cl}$ minerals. Atacamite, or $\beta\text{-Cu}_2(\text{OH})_3\text{Cl}$, is a much more common metastable phase, which has been known as a mineral since the 18th century. Finally, the γ -polymorph clinoatacamite, discovered only in 1996 by Jambor *et al.* [579], is the thermodynamically stable phase at ambient temperatures. The crystal structures of these two phases are similar, as illustrated in Fig. 50. In some of the earlier works, including Ref. [577], before clinoatacamite became known as a separate mineral species, it was sometimes confused with paratacamite [576].

As the most common and well known mineral, atacamite attracted considerable attention of the solid-state physics community, yet its magnetic properties are still a subject of debate. Its crystal structure contains two crystallographically independent Cu atoms in the Jahn-Teller distorted octahedral coordination. The first one is bonded to two Cl atoms, forming a $\text{Cu}(\text{OH})_4\text{Cl}_2$ octahedron, while the other one is bonded to a single Cl atom to form a $\text{Cu}(\text{OH})_5\text{Cl}$ octahedron. This difference leads to a highly distorted pyrochlore structure that can be alternatively viewed as a set of Cu–O–Cu chains connected by CuO ladders [580]. It has been argued based on first-principles DFT calculations that the magnetism in both atacamite and botallackite is quite similar and could be described by an effective quasi-1D uniform AFM chain model with spin frustration arising from the NNN interactions [581]. The similarity of these two polymorphs is also indicated by the similar Néel temperatures of 9.0 and 7.2 K, respectively [580]. On the other hand, the experimental situation with respect to the low-temperature magnetic properties of these minerals remains controversial. Synthetic atacamite was previously reported to exhibit spin-glass behavior [582], whereas AFM behavior was observed in both natural and synthetic samples in more recent studies [580, 583, 584]. In particular, a proton NMR study found no evidence of the disordering or spin-glass moments, but rather suggested an “all-in all-out” type of long-range order [584]. Contrasting results were obtained from μSR measurements, which pointed towards a

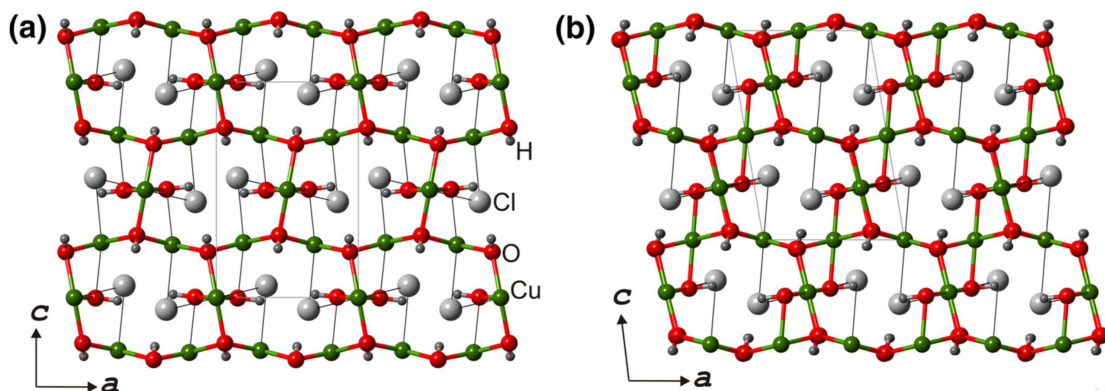


Figure 50. Comparison of the crystal structures of atacamite (a) and clinoatacamite (b), viewed along the b axis. Reproduced with permission from Ref. [576], copyright by Springer-Verlag.

disordered ground state in atacamite and a long-range ordered state in botallackite [580]. On the other hand, a very recent neutron-diffraction study on natural atacamite single crystals originating from the Poona Mine in Australia revealed long-range magnetic order described by the propagation vector $\mathbf{q} = \left(\frac{1}{2} 0 \frac{1}{2}\right)$ [585]. However, the magnetic structure could not be solved unambiguously, and it is still unclear if the magnetic structure proposed by Zenmyo *et al.* [584] is consistent with the observed ordering vector. The final conclusion about the magnetic ground state of atacamite will therefore remain open to debate until a conclusive magnetic structure determination by means of neutron diffraction on pure synthetic crystals becomes available.

Interestingly, a similar controversy also exists about the spin-1 analogue of atacamite, the synthetic frustrated antiferromagnet $\text{Ni}_2(\text{OH})_3\text{Cl}$ with a distorted-pyrochlore structure [586, 587]. It exhibits a clear AFM transition at $T_N = 4$ K seen both in magnetic susceptibility and specific heat, and a long-range magnetic order was evidenced by neutron diffraction. Nevertheless, no signature of an order was detected by μSR [586]. Proton NMR revealed a significant broadening of the spectra below T_N , signalling the development of static internal fields at the ^1H sites, yet a fraction of frozen spins with slow dynamics was found to coexist with the paramagnetic state up to 20 K [587]. Other hydroxyhalides of transition metals, in particular $\alpha\text{-Cu}_2(\text{OH})_3\text{Br}$ and $\alpha\text{-Cu}_2(\text{OH})_3\text{I}$, have also been synthesized [588]. Similar to botallackite, which orders magnetically below $T_N \approx 7.2$ K, its Br- and I-analogs exhibit long-range AFM order with $T_N \approx 10$ and 14 K, respectively.

Finally, magnetic characterization of clinoatacamite [589, 590] and some other compounds of the $M_2(\text{OH})_3\text{Cl}$ ($M = \text{Mn, Fe, Co, Ni}$) transition-metal series [591–593] revealed a co-existence of long-range magnetic order with disordered or fluctuating moments. Results of the magnetization, specific-heat, and μSR experiments have shown that the magnetic order, which occurs in clinoatacamite below $T_{c1} \approx 18.1$ K, is responsible for a surprisingly small entropy release of only $0.05R \ln 2/\text{Cu}$ [589, 590]. Then, another abrupt transition into a metastable spin-glass-like state occurs at $T_{c2} \approx 6.5$ K, accompanied by a large specific-heat anomaly. After that, partial long-range order coexists with fluctuating or disordered moments due to strong frustration, causing a partial depolarization of muon spins down to 20 mK. This kind of coexistence is seen as a common feature of the $M_2(\text{OH})_3\text{Cl}$ compounds, as it also occurs likewise in the case of antiferromagnetic $\text{Fe}_2(\text{OH})_3\text{Cl}$ and ferromagnetic $\text{Co}_2(\text{OH})_3\text{Cl}$ [591, 592]. On the other hand, such coexistence is absent in the isostructural hydroxybromides [593].

More recently, the nature of the successive magnetic transitions in $\gamma\text{-Cu}_2(\text{OH})_3\text{Cl}$ was readdressed by Raman spectroscopy [594]. Both transitions at T_{c1} and T_{c2} have prominent signatures in the Raman response as a result of the spin-phonon coupling. Moreover, the new data point towards the existence of spin fluctuations in the intermediate phase on a picosecond time scale, which falls out of the μSR time window. These fluctuations give rise to a broad continuum in the Raman spectra, providing a reasonable explanation for the previously reported small entropy release across the upper transition. The authors conclude by stating that future NMR and single-crystal neutron studies should further clarify the magnetic structure and the nature of the partial order in clinoatacamite [594].

6.3. Melanothallite: A pyrochlore-lattice antiferromagnet with multiferroic properties

Another cuprate mineral with a pyrochlore-like structure of the magnetic sublattice is the oxychloride Cu_2OCl_2 , known as melanothallite [596]. It crystallizes in an orthorhombic structure with the space group $Fddd$, in which Cu^{2+} occupies a single Wyckoff position, octahedrally coordinated by oxygen and chlorine ions. The copper ions form a 3D network of corner-sharing distorted tetrahedra that can be seen as a deformed pyrochlore lattice, shown in Fig. 51. This mineral first came to attention because of the anomalous negative thermal expansion along the b axis above room temperature [596]. The first low-temperature study revealed an AFM transition in specific heat and magnetic susceptibility at $T_N \approx 70$ K and some signatures of a low-dimensional behavior at higher temperatures [597, 598]. Immediately afterwards, a μ SR study was reported [598], in which clear oscillations of the muon polarization were observed below T_N , evidencing a long-range magnetically ordered state. However, the μ SR spectra showed an excessive damping that had been initially attributed to the effects of frustration.

The first attempt to determine the spin structure in the ordered state of Cu_2OCl_2 was based on Cu-NMR measurements. The study of Nishiyama *et al.* [595] suggested that melanothallite realizes a commensurate all-in-all-out type of magnetic ordering. This conclusion follows from rather indirect evidence, namely from the comparison of the electric field gradient estimated from the measured quadrupolar-resonance frequency with that calculated within a point-charge model, combined with the knowledge about the AFM nature of the NN interaction, resulting from a susceptibility measurement. Moreover, the spin-lattice relaxation rates, measured with ^{35}Cl - and ^{63}Cu -NMR below T_N , are proportional to the first power of temperature, $T_1^{-1} \propto T$, in contrast to the power-law behavior T^α with $\alpha \geq 2$ that is expected for a conventional ordered magnet with spin-wave excitations. This indicates that large spin fluctuations due to geometric frustration must be present in the system [595].

More recent direct measurements of the spin structure in melanothallite by neutron diffraction [599] have discarded the assumption about the commensurate all-in-all-out ground state, proclaiming instead an incommensurate spiral-like phase with a propagation vector $(0.827\ 0\ 0)$. As in many other helimagnetic materials [154, 600], this type of incommensurate noncollinear order leads to multiferroic properties [599]. Thus, synthetic melanothallite exhibits ferroelectricity in measurements of the dielectric constant and pyroelectric polarization as functions of temperature. It therefore represents the first known transition-metal oxyhalide with a multiferroic behavior that persists up to relatively high temperatures.

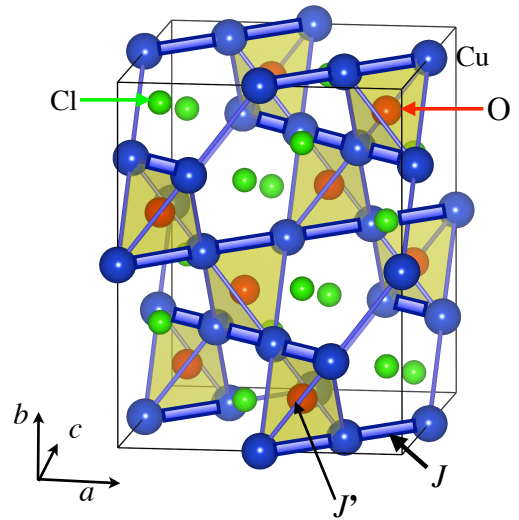


Figure 51. The crystal structure of melanothallite with two dominant magnetic interactions. Reproduced with permission from Ref. [595]. Copyright by the Physical Society of Japan.

A similar lattice with a structure approximating the pyrochlore lattice of $\frac{1}{2}$ -spins is also found in the mineral paramelaconite, Cu_4O_3 . Alternatively, its structure can be seen as alternating chains of edge-shared CuO_4 plaquettes. In contrast to Cu_2OCl_2 , this compound has a more pronounced difference between the interchain and intrachain interactions, which reduces the frustration and places it closer to a low-dimensional spin-chain antiferromagnet [597, 601]. Paramelaconite develops long-range AFM order around 40 K, which has been described as a commensurate noncollinear spin structure with a reduced ordered moment of $\sim 0.46 \mu_B$ and the propagation vector $\mathbf{q} = (\frac{1}{2} \frac{1}{2} \frac{1}{2})$, which is rather unusual for a pyrochlore lattice [601].

6.4. Choloalite: A 3D quantum spin liquid on a hyper-hyperkagomé lattice

A rich variety of minerals is represented by tellurium oxycompounds, some of them realizing unique crystal structures, as summarized in a recent review article by Christy, Mills, and Kampf [602]. Among them, the mineral choloalite, $\text{PbCuTe}_2\text{O}_6$ [546, 603], has a cubic structure with the chiral space group $P4_132$. Its magnetic sublattice of Cu^{2+} ions represents a complex 3D network consisting of two kinds of corner-sharing triangles with different Cu–Cu bond lengths of 4.37 and 5.60 Å. The larger triangles form a hyperkagomé lattice, to which individual smaller triangles are attached, as shown in Fig. 52. Several years ago, it was realized that this mineral could represent a new candidate compound for hosting a 3D quantum spin-liquid state, as it does not order magnetically down to subkelvin temperatures [544, 545], unlike its sibling compound $\text{SrCuTe}_2\text{O}_6$ that shows two magnetic transitions at $T_{\text{N}1} \approx 5.5$ K and $T_{\text{N}2} \approx 4.5$ K [604, 605]. The magnetic specific heat of high-purity synthetic choloalite shows a broad maximum at 1.1 K, followed by a weak kink at 0.87 K of unknown origin [544].

The dominant AFM interactions among the Cu^{2+} ions generate a strongly frustrated hyper-hyperkagomé network of $S = 1/2$ spins, but the magnetic connectivity is additionally enhanced by weaker interactions that partially relieve this frustration. Through a combination of magnetization measurements with NMR and μSR , it was shown that spin fluctuations persist down to 20 mK without spin freezing [545]. Further, the sublinear power-law dependence of the spin-lattice relaxation rate, $T_1^{-1}(T)$, evidences a nonsinglet ground state with a gapless excitation spectrum. From the NMR perspective, anomalies that were observed around 1 K can be related to the dramatic slowing down of the spin dynamics, possibly arising from some kind of instability of the spinon Fermi surface [545].

Inelastic neutron scattering measurements, performed on both powder and single-crystal samples in the group of B. Lake [543], also present strong evidence for the manifestation of a quantum spin liquid in $\text{PbCuTe}_2\text{O}_6$. This is seen, first of all, in the presence of a diffuse continuum

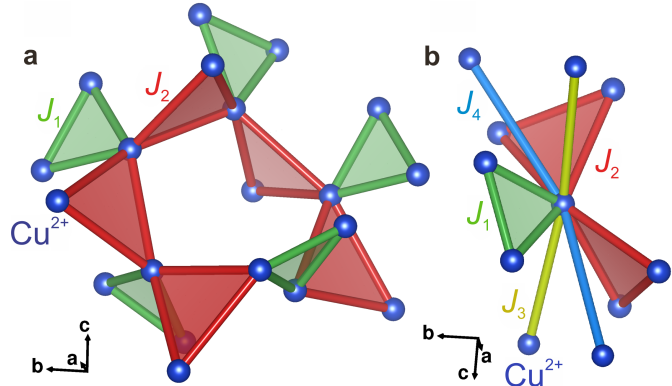


Figure 52. Magnetic sublattice and the model of frustrated magnetic interactions in $\text{PbCuTe}_2\text{O}_6$. Reproduced from Ref. [543].

suggestive of fractionalized spinon excitations. In zero magnetic field, the scattering is concentrated on a sphere with a radius $|\mathbf{Q}| \approx 0.8 \text{ \AA}^{-1}$ in momentum space, dispersing towards lower $|\mathbf{Q}|$ at higher energies. In the same work, DFT calculations have been used to re-estimate exchange interactions, and the results suggest that the two leading frustrated interactions, J_1 and J_2 , are of almost equal strength. This is at variance with the original results of Koteswararao *et al.* [544], where the hyperkagomé interaction J_2 was found to be much stronger than all other interactions. However, the new set of parameters can be well reconciled with the experimental observations. By applying the pseudo-fermion functional renormalization group (PFFRG) approach to the spin model with four exchange parameters, $J_1 \approx J_2 > J_3 > J_4$, the absence of long-range magnetic order could be confirmed for the J_1/J_2 ratios between 0.975 and 1.08, and the calculated value of $J_1/J_2 \approx 1.056$ for $\text{PbCuTe}_2\text{O}_6$ falls within this range [543]. Although infinite classical ground-state degeneracy is strictly present only for vanishing J_3 and J_4 couplings, it has been suggested that these interactions are sufficiently weak in $\text{PbCuTe}_2\text{O}_6$, so that even in the full model considering further-neighbor interactions, long-range magnetic order is fully suppressed by quantum fluctuations.

6.5. Magnetic minerals of the perovskite group

It would be an inexcusable omission not to mention the perovskite-group minerals with their rich and complex structural hierarchy that was recently summarized by Mitchell, Welch, and Chakhmouradian [606]. While the studies of synthetic perovskite-structured compounds have been definitely too extensive to be covered in the scope of the present review, I would like to concentrate here only on some naturally occurring compounds, having no pretensions of comprehensiveness. The classical perovskite has a formula ABX_3 , where A and B are cations, arranged in two interpenetrating simple-cubic sublattices, and X is the anion arranged on an fcc sublattice. In the inverse-perovskite (or antiperovskite) compounds, the cations are replaced by anions, and vice versa, resulting in an A_3BX structure [607]. In spite of their diversity, the majority of the naturally occurring perovskite-group minerals are either nonmagnetic or include magnetic cations only as impurities. Nonetheless, magnetism can occur whenever a magnetic transition-metal or rare-earth ion occupies a cation site. This leads to a simple-cubic lattice of magnetic ions in the case of perovskites, that lacks geometric frustration, or to a geometrically frustrated fcc lattice in the case of antiperovskites. Additional interesting physics can then result from the lowering of crystal symmetry due to the cation or vacancy ordering.

For example, magnetic properties of the anion-deficient compounds that correspond to the minerals of the brownmillerite sub-

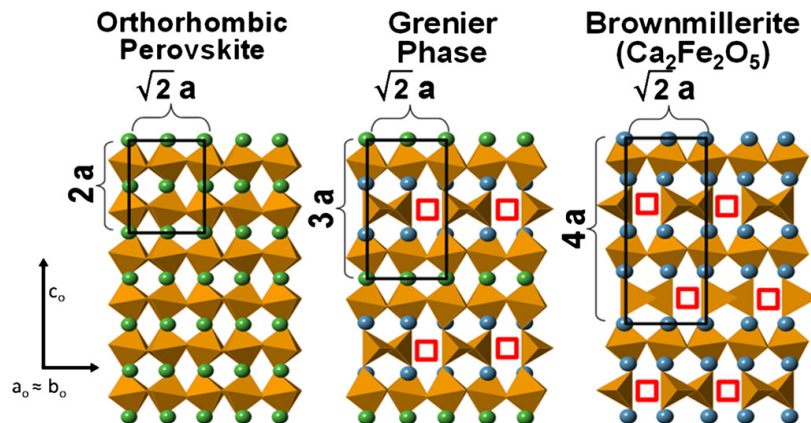


Figure 53. Relationship between the orthorhombic perovskite, Grenier, and brownmillerite crystal structures. The red squares represent ordered oxygen vacancies. Reproduced with permission from Ref. [608].

group, such as $\text{Ca}_2\text{Fe}_2\text{O}_5$, attracted recent attention [609, 610]. The mineral $\text{Ca}_2\text{Fe}_2\text{O}_5$ has an orthorhombic vacancy-ordered structure (see Fig. 53) and orders magnetically far above room temperature, below $T_N \approx 730$ K. The magnetic structure is slightly canted, resulting in weak ferromagnetism [609]. This canting is evidenced by the results of the Mössbauer spectroscopy measurements and can be explained by the presence of DMI that are allowed due to the lowered crystal symmetry. The magnetic properties can be tuned by substituting La for Ca in $\text{Ca}_{2-x}\text{La}_x\text{Fe}_2\text{O}_5$, which tends to destabilize the brownmillerite structure in favor of the Grenier phase, $\text{LaCa}_2\text{Fe}_3\text{O}_8$ [610]. The ferromagnetic hysteresis loops tend to get larger upon La doping, showing a monotonic increase in the coercivity field between $x = 0$ and $x = 1$.

Magnetic ordering is also expected in *A*-site vacant double hydroxyperovskites that form either cubic or tetragonal structures, such as $\text{CuSn}(\text{OH})_6$ (mushistonite), $\text{FeGe}(\text{OH})_6$ (stottite), $\text{FeSn}(\text{OH})_6$ (natanite), $\text{FeSn}(\text{OH})_5\text{O}$ (jeanbandyite), and $\text{MnSn}(\text{OH})_6$ (wickmanite and tetrawickmanite) [606]. In both structures, magnetic ions are arranged into a face-centered cubic or tetragonal sublattice, which has a potential for geometric frustration. However, to the best of my knowledge, the magnetic properties of these hydroxide perovskites have not been investigated until now, neither theoretically nor experimentally. The same likely holds for the naturally occurring stoichiometric *B*-site ordered oxide double-perovskite $\text{Ca}_2\text{NbFe}^{3+}\text{O}_6$ (latrappite).

7. Molecular magnets

7.1. Magnetism in spin clusters

After having discussed one-, two-, and three-dimensional magnetic interaction networks that are found in natural minerals, we now turn to zero-dimensional structures represented by nearly noninteracting spin clusters. The simplest possible example of such a cluster is a spin dimer, which we already discussed in chapter 2. However, larger magnetic clusters that consist of more than two spins can also be found in minerals. They often form regular geometric arrangements of ions that can be viewed as magnetic “molecules”, arranged into a crystal by nonmagnetic spacer atoms. Such clusters would not be stable as standalone molecules outside of the crystal, which offers a natural connection between mineralogy and the highly active research field of molecular magnetism.

Molecular nanomagnets and single-molecule magnets have been in the focus of condensed-matter research since several decades [611–615]. The finite number of spins in the cluster leads to a discrete spectrum of magnetic energy levels. Unlike conventional magnets, magnetic clusters cannot develop a long-range magnetic order. Instead, the ground state is protected by an energy barrier for spin reversal, so that magnetic relaxation slows down below some characteristic blocking temperature T_B that depends on the energy gap separating the ground state from the next excited energy level. This guarantees that the magnetic moments at sufficiently low temperatures acquire a certain static ground-state configuration, by analogy with an ordered state of an infinite system. The magnetic excitation spectrum of such a molecule corresponds to a discrete set of transitions to excited states with different total spin quantum number S , of which only a subset of transitions with $|\Delta S| \leq 1$ can be probed by inelastic neutron scattering. This principle has been most vividly

illustrated by Caciuffo *et al.* [616] in an INS experiment performed on a butterfly-shaped iron molecular cluster with eight Fe^{3+} ions.

Of particular interest are molecular nanomagnets that show geometric frustration [617–619]. This situation occurs whenever the cluster contains antiferromagnetically interacting classical or quantum spins that are arranged in equilateral triangles or, more generally, form closed loops with an odd number of vertices. For instance, a ring of N spins with only nearest-neighbor AFM interactions would be frustrated for every odd N [611]. In 3D, geometrically frustrated clusters can be exemplified by regular or quasiregular polyhedra that contain odd-sided facets. For instance, the Fe_{30} spin icosidodecahedron depicted in Fig. 54 has been experimentally realized in the giant magnetic keplerate molecule $\text{Mo}_{72}\text{Fe}_{30}$ [620, 621], one of the largest single-molecule magnets synthesized to date. It can be thought of as an analog of the kagomé lattice on a sphere, consisting of corner-sharing equilateral triangles that are separated by pentagons (rather than hexagons in the planar kagomé case) [622]. A cuboctahedron, realized in the natural mineral tschörtnerite (see section 7.4), is the only other example of such an arrangement, where the corner-sharing triangles are separated by squares [623, 624].

The presence of frustration may lead to ground-state degeneracy or to the presence of multiple magnetic configurations of the cluster that are very close in energy. In experiments, this can be seen as the appearance of discrete jumps in the field dependence of the magnetization [611], as even relatively weak magnetic fields (as compared to the saturation field) are sufficient to tip the energy balance towards another competing ground-state configuration [618]. From the theory point of view, the benefit of magnetic clusters is that their energy levels can be computed very accurately using exact diagonalization (at least for not too big clusters that preclude this approach due to computational constraints) [617]. This offers not only a perfect opportunity for direct comparisons between theory and experiment, but also allows theorists to predict magnetic properties of various spin clusters that have not been experimentally realized until now. For example, magnetization and specific heat have been calculated for clusters with icosahedral and dodecahedral symmetries under assumption of only nearest-neighbor Heisenberg AFM interactions [625, 626].

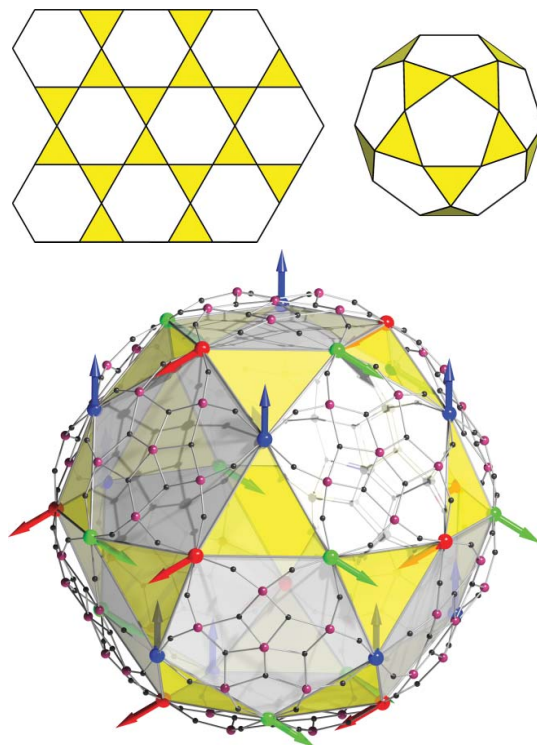


Figure 54. An icosidodecahedron as a molecular analog of the kagomé lattice (top). Its realization in the form of a $\text{Mo}_{72}\text{Fe}_{30}$ cluster is shown below. Reproduced with permission from Ref. [619], copyright by the Royal Society of Chemistry.

7.2. Olivenite and libethenite: A weakly interacting network of AFM tetramer units

The minerals olivenite, $\text{Cu}_2(\text{AsO}_4)(\text{OH})$ [189], and libethenite, $\text{Cu}_2(\text{PO}_4)(\text{OH})$ [627], share the orthorhombic adamite-type structure (space group $Pnnm$) that is built up from linear chains formed by edge-sharing $\text{Cu}(1)\text{O}_4(\text{OH})_2$ octahedra and dimers of edge-sharing $\text{Cu}(2)\text{O}_4(\text{OH})$ trigonal bipyramids [628, 629], as shown in Fig. 55. At the same time, specific heat, magnetization, and magnetic susceptibility measurements on synthetic libethenite samples indicated the absence of any long-range magnetic order down to 1.8 K and a spin gap of about 12 meV [629], suggesting the presence of magnetic clusters with a spin-singlet ground state. From the spin-dimer analysis based on extended Hückel tight-binding calculations, Belik *et al.* [629] concluded that the magnetic couplings both along the chains and within the dimers are negligibly weak, in accordance with the GKA rules for the $\text{Cu}(1)-\text{O}-\text{Cu}(1)$ bond angles of 96.7° and 100.3° , respectively. The strongest AFM superexchange interaction $J_1 \approx 12$ meV actually occurs between the $\text{Cu}(1)$ and $\text{Cu}(2)$ atoms mediated by the OH group with a large $\text{Cu}(1)-\text{O}-\text{Cu}(2)$ bridging angle of 122.9° , and the next-strongest interaction J_2 is given by the $\text{Cu}(2)-\text{O} \cdots \text{O}-\text{Cu}(2)$ super-superexchange between the structural dimers. Therefore, the magnetic model of libethenite involves weakly interacting rhombic tetramer clusters coupled by J_1 . This gives the natural explanation of the spin gap as the separation between the spin-singlet ground state and the excited triplet state of the cluster.

This scenario has been verified more recently by ^{31}P NMR [630] and powder neutron spectroscopy measurements [631]. The temperature-dependent shift of the NMR line points towards low-dimensional magnetism and can be perfectly described by the isolated spin-tetramer model. The spin-lattice relaxation rate measurements confirmed the presence of a 12 meV spin gap, which coincides with the leading exchange parameter J_1 [630] and perfectly agrees with the earlier results of Belik *et al.* [629]. This energy also coincides with the lowest dispersionless magnetic excitation (E_1) measured on a powder sample using neutron spectroscopy, which corresponds to the transition from the singlet ground state to the first excited triplet state. However, the second higher-energy excitation (E_2), which is expected at twice this energy (~ 24 meV) according to the simple tetramer model, was observed at a lower energy of $E_2 = 20$ meV. It corresponds to the transition from the ground state to the second excited triplet state. The observed ratio $E_2/E_1 \approx 5/3$ could be explained by including diagonal couplings of the order of 4 meV within the tetramer [631].

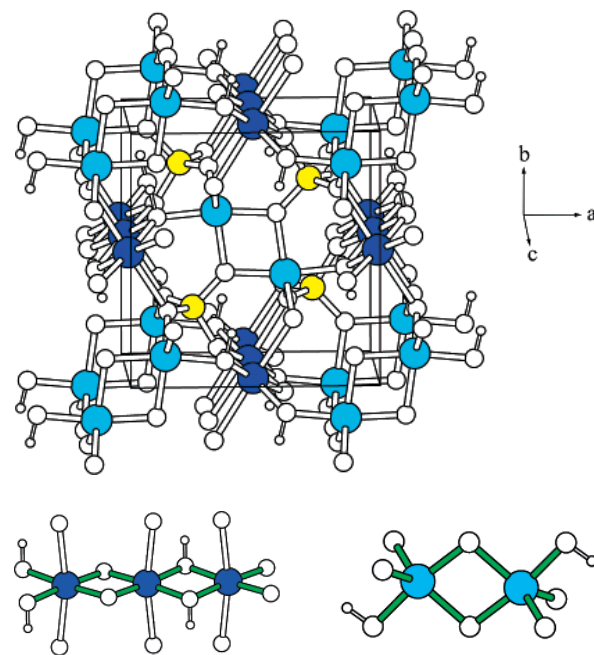


Figure 55. The crystal structure of adamite-type minerals with its two building blocks: an edge-sharing $[\text{Cu}(1)_2\text{O}_6(\text{OH})_2]_\infty$ chain and an edge-sharing $\text{Cu}(2)_2\text{O}_6(\text{OH})_2$ dimer. Reproduced with permission from Ref. [629], copyright by the American Chemical Society.

Apart from the copper-based spin- $\frac{1}{2}$ systems represented by olivenite and libethenite, the same adamite-type crystal structure is also realized in several magnetic systems with higher half-integer values of the spin. These include the synthetic compounds $\text{Co}_2(\text{PO}_4)(\text{OH})$ [628, 632] and $\text{Co}_2(\text{AsO}_4)(\text{OH})$ [633] with $S = 3/2$ and the mineral eveite, $\text{Mn}_2(\text{AsO}_4)(\text{OH})$, with $S = 5/2$. However, their magnetic properties are drastically different. The Co compounds are known as 3D antiferromagnets [628, 632, 633], whereas partial substitution of Cu for Co in the $(\text{Co}_{1-x}\text{Cu}_x)_2(\text{OH})\text{PO}_4$ series of solid solutions suppresses the ordering temperature and leads to the onset of low-dimensional magnetic properties [634]. This crossover has been explained theoretically by a combination of structural distortions and changes in the localized band structure [635]. Compounds with a partial substitution of Co^{2+} ($S = 3/2$) with Ni^{2+} ($S = 1$) [636] and with the substitution of (PO_4^{3-}) by (AsO_4^{3-}) [637] have been also studied. The corresponding Mn compounds, however, received much less attention with respect to their magnetic properties and would deserve a dedicated investigation.

7.3. Boleite: Cu_{24} clusters in the form of truncated cubes

The complex halide mineral boleite with the formula $\text{KPb}_{26}\text{Ag}_9\text{Cu}_{24}(\text{OH})_{48}\text{Cl}_{62}$ [638, 639] forms large deep-blue cubic crystals. Its crystal structure, with the space group $Pm\bar{3}m$, has a large cubic unit cell with the lattice parameter $a = 15.29$. All atoms in the unit cell, except for the Cu^{2+} ions, are nonmagnetic. There are 24 structurally equivalent magnetic Cu^{2+} ions per unit cell that form a cluster shaped as a truncated cube (see Fig. 56). The large distance between such clusters ensures that they are magnetically decoupled and can be seen as isolated molecular magnets. One expects two dominant superexchange interactions that act along the sides of the triangles, J_1 , with the $\text{Cu}-\text{O}-\text{Cu}$ bridging angle of 125.2° , and along the rungs connecting them, J_2 , with the bridging angle of 94.7° [640]. According to the GKA rules, J_1 must be antiferromagnetic and therefore strongly frustrated, whereas J_2 is expected to be smaller due to the proximity of the $\text{Cu}-\text{O}-\text{Cu}$ bridging angle to the point where the FM and AFM exchange contributions are compensated [88].

Magnetic properties of boleite were recently studied by Dreier *et al.* [640] using several natural mm-sized single crystals. They compared magnetic susceptibility measurements with the results of exact diagonalization to reveal the ground state of the Cu_{24} cluster, quantify the exchange interactions, and understand the low-temperature spin dynamics. According to their results, the spin system in boleite is characterized by two distinct temperature scales. At temperatures below ~ 100 K, the spins on individual triangles (trimers), bound by strong intratrimer interactions $J_1 \approx 17.9$ meV, freeze into a state that represents a linear combination

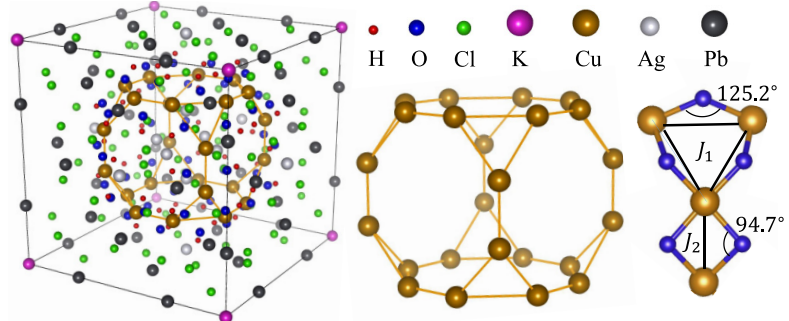


Figure 56. The crystal structure of boleite: The unit cell (left), the Cu_{24} cluster (middle), and its fragment showing relevant exchange interactions and bond angles (right). Reproduced with permission from Ref. [640], copyright by the American Physical Society.

of basis states of the form $|\uparrow\downarrow\downarrow\rangle$ and equivalent cyclic permutations thereof, resulting in an effective $S = 1/2$ degree of freedom on every triangle. At much lower temperatures, $T \lesssim 5$ K, these effective spins that sit at the vertices of the cube undergo dimerization due to the weaker interactions $J_2 \approx 3.3$ meV. This results in a singlet ground state of the whole cluster, separated from the nearest magnetic excited state by a small spin gap of the order of 1 meV. The authors used a combined projectional and trimer (CPT) model with these parameters and could successfully describe the measurements in the whole measured range of temperatures [640].

Unfortunately, the need to rely on natural single crystals, that may vary in their chemical composition and structural quality, and the inability to synthesize the deuterated version of boleite artificially for neutron-scattering experiments have so far precluded more thorough investigations of their spin dynamics. In particular, the value of the spin gap has not been measured directly. Also, no magnetization plateaus or similar anomalies could be revealed, most probably due to the insufficient chemical and structural homogeneity of the natural samples. Neutron-scattering experiments, described in the appendix B of Ref. [640], were essentially unsuccessful as they were unable to detect any magnetic signal, most likely because of the large incoherent-scattering background from hydrogen. Reportedly, even the use of polarized neutrons could not overcome this problem. On the other hand, the search for higher-energy excitations at the scale of J_1 proved to be very difficult due to the large number of optical phonons in this energy region. Notwithstanding, boleite certainly represents a unique natural realization of a molecular-magnet system, realizing a quantum $S = 1/2$ magnetic cluster that has not been reported so far in any other compound. Therefore, the synthesis of chemically pure artificial boleite would certainly open up a new research direction for a number of experimental techniques, including high-field magnetization, local probes, and neutron spectroscopy.

Two minerals that are closely related to boleite are pseudoboleite, $\text{Pb}_{31}\text{Cu}_{24}\text{Cl}_{62}(\text{OH})_{48}$ [641], and cumengeite, $\text{Pb}_{21}\text{Cu}_{20}\text{Cl}_{42}(\text{OH})_{40} \cdot 6\text{H}_2\text{O}$ [642]. They have less symmetric tetragonal unit cells in which Cu^{2+} ions occupy two inequivalent general Wyckoff positions. In pseudoboleite, the Cu_{24} clusters have approximately the same shape and size as in boleite, but are arranged in a body-centered tetragonal lattice, therefore one expects that the essential physical properties of individual clusters should remain the same. In cumengeite, the

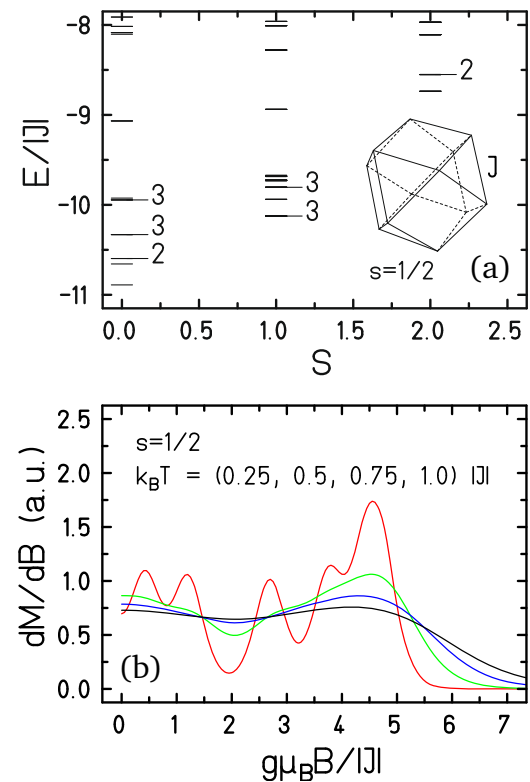


Figure 57. (a) Calculated low-lying energy levels for a regular cuboctahedral cluster of antiferromagnetically interacting spin- $\frac{1}{2}$ ions with an exchange constant J (see inset). Numbers near selected levels denote their multiplicities. (b) Differential susceptibility of the same cluster as a function of applied field for several temperatures. Reproduced from Ref. [623], copyright by Elsevier B.V.

Cu_{20} clusters are flattened, as would result from collapsing the truncated cube by eliminating the rungs parallel to the c direction.

7.4. Tschörtnerite: Cuboctahedral Cu_{12} clusters

In 1993, a new mineral of the zeolite group [643] with a conspicuously large cubic unit cell (space group $Fm\bar{3}m$, lattice parameter $a = 31.62 \text{ \AA}$) was discovered by the mineral collector Jochen Tschörtner at the Bellberg volcano near Mayen, Eifel, Germany. It was named tschörtnerite after a detailed structural characterization published 5 years later [644]. The mineral is very rare and is found only in small cubic light-blue transparent crystals with a maximum size up to 0.15 mm, which can be described by the chemical formula $\text{Ca}_4(\text{K,Ca,Sr,Ba})_3\text{Cu}_3\text{Al}_{12}\text{Si}_{12}\text{O}_{48}(\text{OH})_8 \cdot 20\text{H}_2\text{O}$. Despite the very complex structure and chemistry of tschörtnerite, its putative spin- $\frac{1}{2}$ magnetic sublattice is surprisingly simple and symmetric. The copper ions occupy a single Wyckoff position and form well separated Cu_{12} clusters in the form of regular cuboctahedra, surrounded by nonmagnetic atoms. This mineral can therefore serve as a paradigmatic example of a crystal consisting of nearly noninteracting frustrated magnetic molecules with several nearest-neighbor superexchange paths, similar to the above-discussed boleite.

The relatively small size of the clusters allows for an exact diagonalization of its complete energy spectrum [623, 624], which is reproduced here in Fig. 57 (a). As it is common for many geometrically frustrated low-dimensional quantum magnets [645], the ground state of the molecule is a spin singlet, and there are several low-lying excited singlet states below the first triplet. The rather high symmetry of the cluster leads to a high degeneracy among its energy levels. The lowest of the $S = 0$ excitations defines an energy gap of $\sim 0.23|J|$, whereas the first $S = 1$ excitation is found at $\sim 0.77|J|$ and is ninefold degenerate. The corresponding differential susceptibility as a function of an applied magnetic field, $g\mu_B B/|J|$, was calculated for different values of the normalized temperature, $k_B T/|J|$, as plotted in Fig. 57 (b).

8. Itinerant magnetism

8.1. Mackinawite: The natural prototype of an iron-based superconductor

Practically all minerals discussed to this point were insulators. Indeed, there are very few examples of naturally occurring stoichiometric metallic minerals that show magnetic properties. I deliberately leave aside the discussion of nickel-iron alloys, for example, that occur in meteorites [36, 646], as they are non-stoichiometric, well understood and described, and represent little interest from the point of view of fundamental solid-state physics. However, it is well known that some of the binary iron-chalcogenide compounds, for instance the metastable tetragonal iron-sulfide phase (space group $P4/nmm$) that is isostructural to the mineral mackinawite, $t\text{-(Fe,Ni)}_{1+x}\text{S}_{1-y}$, are metallic [647–650]. Tetragonal iron sulfide recently became famous as an unconventional superconductor with a T_c of $\sim 4.5 \text{ K}$ [651, 652], showing structural similarity to the superconducting iron arsenides [653, 654]. However, one should not forget that the interest in this compound existed much earlier in geochemistry and mineralogy [655–658]. Unfortunately, naturally occurring mackinawite usually contains significant admixtures of other transition metals (Co, Ni, Cu) that can

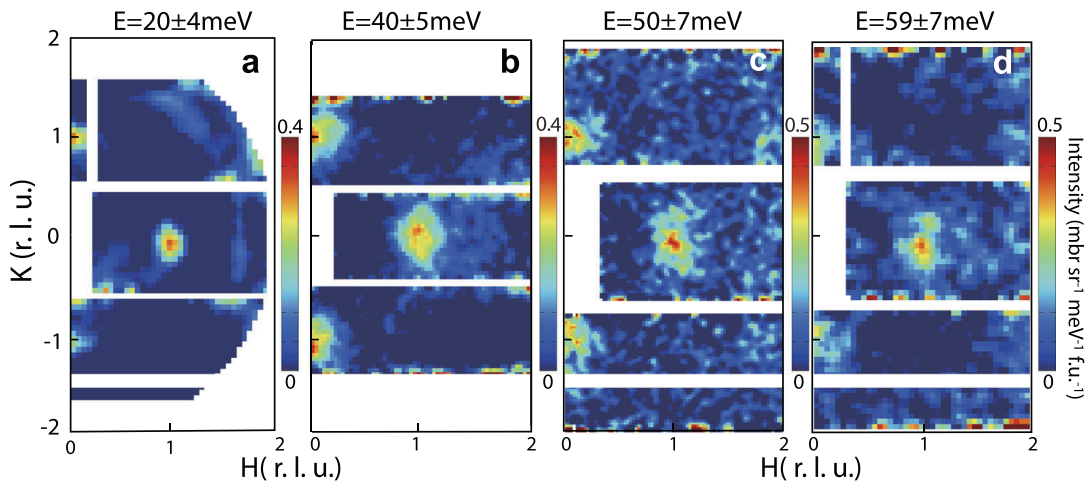


Figure 58. Spin excitations in tetragonal FeS, measured by time-of-flight neutron spectroscopy at different energy transfers, as indicated above each panel. Reproduced with permission from Ref. [662].

intercalate between the iron sheets, occupying interstitial sites [659, 660]. Because it is known that at much as 10% of Co or Ni impurities can suppress superconductivity in iron chalcogenides [661], it is doubtful that superconductivity can be found in natural mackinawite samples.

Already in 1971, Mössbauer measurements on natural mackinawite were performed down to 4.2 K [663]. However, these early data showed no signatures of magnetic order, and a low-spin state of iron was concluded. Three decades later, low-temperature Mössbauer measurements were repeated on synthetic $t\text{-Fe}_{1+x}\text{S}_{1-y}$, revealing clear signatures of magnetic order [658]. From more recent studies [650, 664], it became known that this order represents a commensurate AFM structure with the propagation vector $(\frac{1}{4} \frac{1}{4} 0)$ and a Néel temperature $T_N \approx 116$ K. It has been even suggested that this magnetic state may stabilize a topologically nontrivial band structure with symmetry-protected surface states [665]. Remarkably, around the same time, other authors [662, 666] suggested that the magnetic order in mackinawite originates from impurities and is not an intrinsic property of pure $t\text{-FeS}$. In high-quality single crystals, neutron scattering found no signatures of static magnetic order down to 3 K [662]. Moreover, inelastic neutron scattering data, reproduced here in Fig. 58, revealed dynamic spin-stripe fluctuations residing at the usual $(\pi, 0)$ wave vector that corresponds to the nesting of the hole and electron Fermi surfaces, as in most other iron-based superconductors [667, 668]. These fluctuations do not couple to superconductivity, suggesting that FeS is a weakly correlated analog of its sibling compound FeSe. This conclusion follows from a much smaller enhancement of the effective electron mass and from a much larger energy scale for spin fluctuations [662].

9. Summary and outlook

The numerous case studies presented in this review illustrate that the world of minerals offers an inexhaustible source of materials and crystal structures as a playground for the realization of various models in quantum magnetism and for trying computational approaches of modern

quantum chemistry. A considerable number of works summarized here were undertaken during the last two decades, marking an appearance of a new interdisciplinary field of research that bridges mineralogy with low-temperature condensed-matter physics. For most of the studied compounds, it was impossible to comprehend the underlying physics that determines their magnetic properties from just a superficial examination of their structure. On many occasions, the application of modern experimental and computational methods offered new surprises, and the ultimate understanding of the magnetic properties of most minerals was gained from a long sequence of trial and error that extended over several decades. At the same time, we have to admit that apart from a mere handful of examples presented here, the majority of known minerals have not been so far subjected even to the simplest low-temperature physical characterization, not even to magnetic susceptibility or magnetization measurements. In this respect, physicists have barely scratched the surface of the vast variety of magnetic minerals that could serve as subjects for future studies. There are ongoing systematic low-temperature investigations of natural samples from the world's largest mineral collections [669]. It is therefore interesting to speculate here about the potential interest that other naturally occurring crystal structures with magnetic ions could represent for the condensed-matter physics community.

There are abundant examples of copper oxysalt minerals realizing various spin- $\frac{1}{2}$ magnetic sublattices at low temperatures that have not, as of yet, received much attention from the point of view of their low-temperature physical properties. A general structural classification of cuprates illustrated with multiple examples has been discussed, for instance, by Leonyuk *et al.* [670, 671], and the structural details resulting from Jahn-Teller effects in Cu^{2+} oxysalt minerals have been reviewed by Burns and Hawthorne [389]. Some of these minerals realize very complex crystal structures, as it is the case for chloromenite, $\text{Cu}_9\text{O}_2(\text{SeO}_3)_4\text{Cl}_6$, that was recently identified as a promising multiferroic material [672]. Its lattice contains five structurally inequivalent copper sites that order antiferromagnetically below the Néel temperature of $T_N \approx 16$ K, that can be further increased with magnetic fields. At a higher temperature of $T_E \approx 267$ K, an antiferroelectric transition takes place.

A low-dimensional structure consisting of $\text{Cu}_3(\text{OH})_2$ ferrimagnetic ribbons of edge-sharing copper octahedra is realized in the copper-molybdate mineral lindgrenite, $\text{Cu}_3(\text{MoO}_4)_2(\text{OH})_2$ [673]. Neutron-diffraction measurements revealed that below the ordering temperature of ~ 13 K, the magnetic moments on the two inequivalent copper sites both point along the a axis and are antiparallel to each other, showing no signs of geometric frustration [674]. On the other hand, the dehydrated version of the same mineral, $\text{Cu}_3\text{Mo}_2\text{O}_9$ [675], forms distorted tetrahedral spin chains running parallel to the b axis that support a weakly ferromagnetic noncollinear magnetic order as a result of frustration [676].

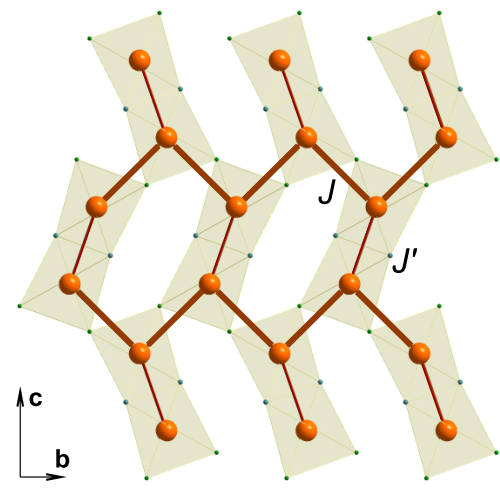


Figure 59. The 2D network of structural dimers in nissenite, forming a coupled lattice of zigzag magnetic chains. Larger spheres denote Cu^{2+} ions, small dots are oxygen atoms.

A much simpler two-dimensional arrangement of structural dimers, shown in Fig. 59, occurs in the copper phosphate mineral nissonite, $\text{Cu}_2\text{Mg}_2(\text{PO}_4)_2(\text{OH})_2 \cdot 5\text{H}_2\text{O}$, crystallizing in the space group $C2/c$ [677]. According to GKA rules, it should be described by two dominant AFM interactions, resulting in coupled AFM zigzag chains. It would be therefore interesting to investigate its magnetic ground state and study its proximity to a magnetic QCP. Another phosphate mineral cornetite, $\text{Cu}_3(\text{PO}_4)(\text{OH})_3$, features buckled layers consisting of edge-sharing zigzag chains of Jahn-Teller distorted octahedra, cross-linked by edge-sharing octahedral dimers [678]. Edge-sharing sheets consisting of distorted copper-ion polyhedra are also found in pseudomalachite, $\text{Cu}_5(\text{PO}_4)_2(\text{OH})_4$ [679], its isostructural arsenate analog cornwallite, $\text{Cu}_5(\text{AsO}_4)_2(\text{OH})_4$, and its polymorph cornubite [680]. Another arsenate mineral bradaczekite, $\text{NaCu}_4(\text{AsO}_4)_3$, features chains formed by edge-sharing CuO_6 octahedra and AsO_4 groups, linked into 2D sheets [681].

A very rich variety of low-dimensional structures can be also found in copper sulfate minerals [497, 498]. To name just a few examples, the mineral leightonite, $\text{K}_2\text{Ca}_2\text{Cu}(\text{SO}_4)_4 \cdot 2\text{H}_2\text{O}$ [682], has two sets of linear copper chains that run at 65.5° to each other. In cyanochroite, $\text{K}_2\text{Cu}(\text{SO}_4)_2 \cdot 6\text{H}_2\text{O}$ [683], and in kröhnkite, $\text{Na}_2\text{Cu}(\text{SO}_4)_2 \cdot 2\text{H}_2\text{O}$ [684], the Cu^{2+} ions are well separated by SO_4 groups, water molecules, and alkali-metal ions, resulting in large Cu–Cu distances with no immediate superexchange paths. This could result in exceedingly small magnetic interactions and spin dynamics, restricted to very low energies.

Recent years also saw heightened interest to the copper-tellurium oxide minerals [351, 602]. Some of them have been already discussed in sections 5.4 and 6.4 as prospective maple-leaf lattice antiferromagnets or promising quantum spin-liquid candidates. Very recently, another copper-tellurium compound Cu_3TeO_6 , naturally occurring as the green mineral mcalpineite [686], was identified as a host of topological magnon excitations [685, 687]. The interesting geometry of its magnetic lattice, composed of almost planar regular vertex-shared hexagons of Cu^{2+} $S = \frac{1}{2}$ spins, has been noted already in 2005, as it was first characterized by magnetic susceptibility, torque magnetometry, and neutron powder diffraction measurements [688]. This structure became known as a “spin web” [689]. Large synthetic single crystals of Cu_3TeO_6 have been produced by the PbCl_2 flux method [690]. The compound orders magnetically below $T_N \approx 61.7$ K, developing a collinear AFM order as shown in Fig. 60. Such a magnetic state has a PT symmetry (P and T being space-inversion and time-reversal operations, respectively), which implies that magnons are expected to exhibit nontrivial topological properties, as it was recently confirmed in INS measurements [685, 687]. In a recent review, Norman [351] also emphasized that the mineral leisingite, $\text{MgCu}_2\text{TeO}_6(\text{H}_2\text{O})_6$ [691], is a realization of a spin- $\frac{1}{2}$ honeycomb lattice with an expected compensation of superexchange interactions along the Cu–O–Cu paths, whereas jensenite, $\text{Cu}_3\text{TeO}_6(\text{H}_2\text{O})_2$ [692], contains distorted brucite-like honeycomb layers in combination with isolated dimers [602].

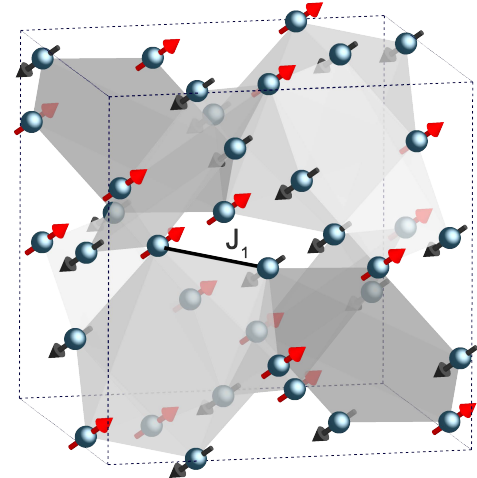


Figure 60. The magnetic structure of Cu_3TeO_6 , reproduced from Ref. [685].

Finally, crystal structures that combine Cu^{2+} spin- $\frac{1}{2}$ moments with other magnetic ions are also common. For instance, the new arsenate mineral auriacusite of the olivenite group, $\text{Fe}^{3+}\text{Cu}^{2+}\text{AsO}_4\text{O}$, with the structure shown in Fig. 61, has a network of connected copper octahedra, connected via magnetic Fe^{3+} sites [693]. Another arsenate mineral arthurite, $\text{CuFe}_2^{3+}(\text{AsO}_4)_2(\text{OH})_2 \cdot 4\text{H}_2\text{O}$, has a monoclinic structure (space group $P2_1/c$), in which copper and iron planes alternate along the a axis [694]. The copper planes have a nearly perfect triangular-lattice structure, consisting of isosceles triangles with the base of 5.60 Å and the sides of 5.58 Å, whereas the iron planes consist of structural dimers formed by edge-sharing octahedra, which are in turn arranged by corner sharing into buckled layers as shown in Fig. 62. Then, a newly discovered mineral iyoite, $\text{MnCuCl}(\text{OH})_3$ [342], is a Mn-Cu ordered analogue of botallackite. Its structure is based on brucite-like sheets orthogonal to the a axis, built from distorted edge-sharing $\text{Mn}(\text{OH})_5\text{Cl}$ and $\text{Cu}(\text{OH})_4\text{Cl}$ octahedral chains that alternate along the c direction. It is therefore expected to show magnetic properties arising from an interaction of quantum and classical spins on two interpenetrating quasi-low-dimensional sublattices.

The examples given here are intended to show that the investigations of quantum magnetism in crystal structures motivated by naturally occurring minerals are far from being complete. Many new studies appear every year, which are concerned with the physical problems that are absolutely

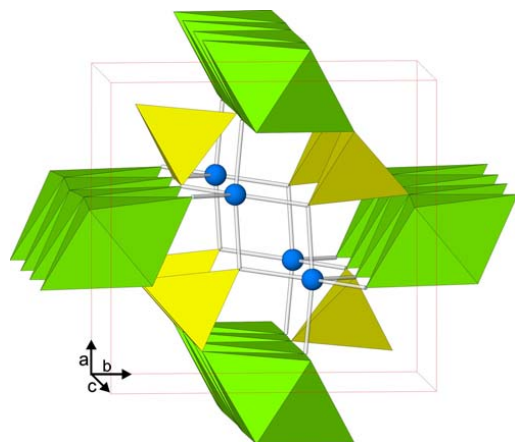


Figure 61. The crystal structure of auriacusite. The spheres represent Fe^{3+} ions, Cu octahedra are shown in green, and As tetrahedra in yellow. Reproduced with permission from Ref. [693], copyright by Springer-Verlag.

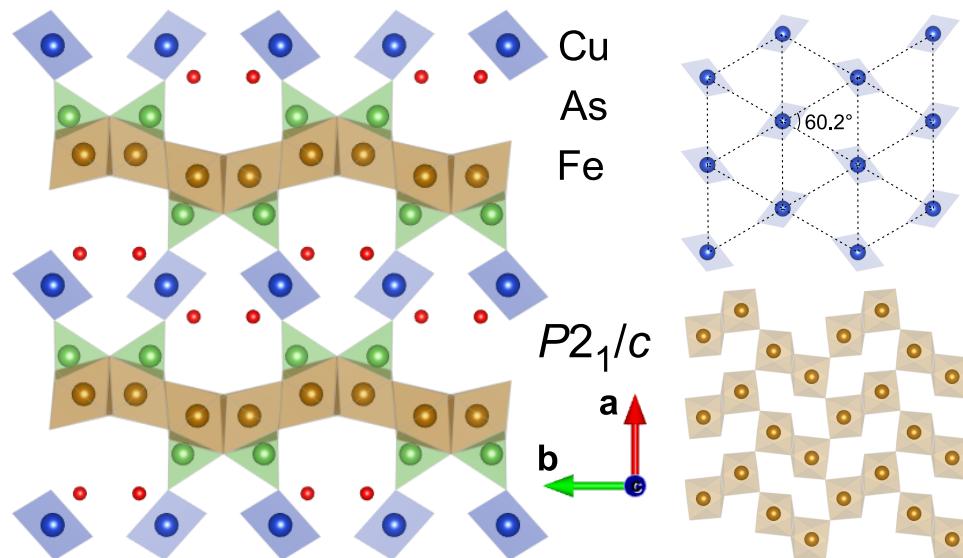


Figure 62. The crystal structure of arthurite [694]. The right panels show copper (top) and iron (bottom) planes viewed along the a axis.

central for modern solid-state physics. Future progress will certainly depend on the ability to reproduce complex mineral structures in the form of chemically pure synthetic samples, and the incessant discoveries of new minerals should guide chemists in this endeavor. In this emerging field of knowledge, new results are expected from fruitful collaborations among mineralogists, crystallographers, chemists and crystal growers, experimental solid-state physicists, and condensed-matter theorists.

Acknowledgments

I would like to thank H. Rosner (MPI CPfS, Dresden) and K. Lefmann (Niels Bohr Institutet, Copenhagen) for stimulating discussions, as well as J. Hunger, U. Bläß, and Th. Schlothauer for the inspiration gained from visiting the mineral collection at the TU Bergakademie Freiberg. I also thank A. S. Cameron for a thorough proofreading of the manuscript and A. A. Tsirlin for very helpful critical suggestions on its content. This work has been funded by the German Research Foundation (DFG) within the Collaborative Research Center SFB 1143 in Dresden (project C03).

References

- [1] Bohm J 1985 *Acta Physica Hungarica* **57** 161–178
- [2] Scheel H J 2000 *J. Cryst. Growth* **211** 1–12
- [3] Mattis D C 1981 *History of Magnetism in The Theory of Magnetism I* (Springer Series in Solid-State Sciences vol 17, p 1–38, Springer-Verlag Berlin Heidelberg)
- [4] Roda A 2011 *Chemiluminescence and Bioluminescence* (RSC Publishing)
- [5] Arago F 1811 *Mémoires de la classe des sciences mathématiques et physiques de l'Institut Impérial de France* **1** 93–134
- [6] Weber H F 1875 *Phil. Mag.* **49** 161
- [7] Einstein A 1907 *Annalen der Physik* **22** 180
- [8] Bundy F P, Hall H T, Strong H M and Wentorf R H 1955 *Nature* **176** 51–55
- [9] Soule D E, McClure J W and Smith L B 1964 *Phys. Rev.* **134** A453–A470
- [10] Zhou S Y, Gweon G H, Graf J, Fedorov A V, Spataru C D, Diehl R D, Kopelevich Y, Lee D H, Louie S G and Lanzara A 2006 *Nature Phys.* **2** 595–599
- [11] Grüneis A, Attaccalite C, Pichler T, Zabolotnyy V, Shiozawa H, Molodtsov S L, Inosov D, Koitzsch A, Knupfer M, Schiessling J, Follath R, Weber R, Rudolf P, Wirtz L and Rubio A 2008 *Phys. Rev. Lett.* **100** 037601
- [12] Brockhouse B N 1961 *Methods for Neutron Spectrometry* (Chalk River, Ontario)
- [13] Brockhouse B N, Woods A D B, Dolling G and Thorson I M 1964 *Research with Inelastic Neutron Scattering at the NRU Reactor* (International Conference on the peaceful uses of atomic energy, Geneva) pp 1–13
- [14] Brockhouse B N 1957 *Phys. Rev.* **106** 859–864
- [15] Néel L 1948 *Annales de Physique* **3** 137–198
- [16] Shull C G, Wollan E O and Koehler W C 1951 *Phys. Rev.* **84** 912–921
- [17] Samuels E J, Bleeker E J, Dobrzynski L and Riste T 1968 *J. Appl. Phys.* **39** 1114–1115
- [18] Samuels E J, Hutchings M T and Shirane G 1970 *Physica (Utrecht)* **48** 13
- [19] Samuels E J and Shirane G 1970 *Phys. Stat. Sol.* **42** 241–256
- [20] Morin F J 1950 *Phys. Rev.* **78** 819–820
- [21] Besser P J, Morrish A H and Searle C W 1967 *Phys. Rev.* **153** 632–640
- [22] Shull C G, Strauser W A and Wollan E O 1951 *Phys. Rev.* **83** 333–345
- [23] Nathans R, Pickart S J, Alperin H A and Brown P J 1964 *Phys. Rev.* **136** A1641–A1647
- [24] Hulthén L 1936 *Proc. Acad. Sci. Amst.* **39** 190
- [25] Robinson P, Harrison R J, McEnroe S A and Hargraves R B 2002 *Nature* **418** 517–520

- [26] McEnroe S A, Harrison R J, Jackson M J, Hirt A M, Robinson P, Langenhorst F, Heidelbach F, Kasama T, Putnis A, Brown L L and Golla-Schindler U 2005 *J. Phys.: Conf. Ser.* **17** 154
- [27] Brok E, Sales M, Lefmann K, Kuhn L T, Schmidt W F, Roessli B, Robinson P, McEnroe S A and Harrison R J 2014 *Phys. Rev. B* **89** 054430
- [28] Chattopadhyay T, Burlet P and Brown P J 1991 *J. Phys.: Condens. Matter* **3** 5555–5561
- [29] Chattopadhyay T, Burlet P, Regnault L P and Rossat-Mignod J 1989 *Physica B: Condens. Matter* **156 & 157** 241–243
- [30] Chattopadhyay T, Brückel T and Burlet P 1992 *Physica B: Condens. Matter* **180 & 181** 71–72
- [31] Kimber S A J and Chatterji T 2015 *J. Phys.: Condens. Matter* **27** 226003
- [32] Kimber S A J, Salamat A, Evans S R, Jeschke H O, Muthukumar K, Tomić M, Salvat-Pujol F, Valentí R, Kaisheva M V, Zizak I and Chatterji T 2013 *Proc. Nat. Acad. Sci. USA* **111** 5106–5110
- [33] Ghose S, Coey J M D and Salje E (eds) 1988 *Structural and Magnetic Phase Transitions in Minerals (Advances in Physical Geochemistry vol 7)* (Springer)
- [34] Rinaldi R 2002 *Eur. J. Mineral.* **14** 195–202
- [35] Dove M T 2002 *Eur. J. Mineral.* **14** 203–224
- [36] Stacey F D and Banerjee S K 1974 *The Physical Principles of Rock Magnetism (Developments in Solid Earth Geophysics vol 5)*, Elsevier, Amsterdam
- [37] O'Reilly W 1984 *Rock and Mineral Magnetism* (Springer, Boston, MA)
- [38] O'Reilly W 1976 *Rep. Prog. Phys.* **39** 857–908
- [39] Hunt C P and Moskowitz B P 1995 *Magnetic properties of rocks and minerals* in Ahrens T J *Rock Physics and Phase Relations: A Handbook of Physical Constants* vol 3 (Washington, DC: Am. Geophys. Union) pp 189–204
- [40] Dunlop D J and Özdemir O 1997 *Rock magnetism: Fundamentals and Frontiers* (Cambridge Univ. Press)
- [41] Harrison R J 2000 *Rev. Mineral. Geochem.* **39** 175–202
- [42] Wang Y, Pascut G L, Gao B, Tyson T A, Haule K, Kiryukhin V and Cheong S W 2015 *Sci. Rep.* **5** 12268
- [43] Kurumaji T, Ishiwata S and Tokura Y 2015 *Phys. Rev. X* **5** 031034
- [44] Li Y, Gao G and Yao K 2017 *Europhys. Lett.* **118** 37001
- [45] McAlister S P and Strobel P 1983 *J. Magn. Magn. Mater.* **30** 340–348
- [46] Kurumaji T, Takahashi Y, Fujioka J, Masuda R, Shishikura H, Ishiwata S and Tokura Y 2017 *Phys. Rev. B* **95** 020405
- [47] Ter-Oganessian N V, Guda A A and Sakhnenko V P 2017 *Sci. Rep.* **7** 16410
- [48] Wang J and Sun X 2015 *Energy Environ. Sci.* **8** 1110
- [49] Rousse G, Carvajal J R, Patoux S and Masquelier C 2003 *Chem. Mater.* **15** 4082
- [50] Li J, Garlea V O, Zarestky J L and Vaknin D 2006 *Phys. Rev. B* **73** 024410
- [51] Valdez M N, Efthimiopoulos I, Taran M, Müller J, Bykova E, McCammon C, Koch-Müller M and Wilke M 2018 *Phys. Rev. B* **97** 184405
- [52] Golosova N O, Kozlenko D P, Dubrovinsky L S, Cerantola V, Bykov M, Bykova E, Kichanov S E, Lukin E V, Savenko B N, Ponomareva A V and Abrikosov I A 2017 *Phys. Rev. B* **96** 134405
- [53] Normand B 2009 *Contemp. Phys.* **50** 533
- [54] Balents L 2010 *Nature* **464** 199–208
- [55] Mendels P and Wills A S 2011 *Kagomé Antiferromagnets: Materials vs. Spin Liquid Behaviors* in Lacroix C, Mendels P, and Mila F (eds) *Introduction to Frustrated Magnetism* (Springer Series in Solid-State Sciences, vol **164**, 2nd ed, Springer-Verlag Berlin) pp 475–507
- [56] Norman M R 2016 *Rev. Mod. Phys.* **88** 041002
- [57] Mendels P and Bert F 2016 *C. R. Physique* **17** 455–470
- [58] Savary L and Balents L 2017 *Rep. Prog. Phys.* **80** 016502
- [59] Zhou Y, Kanoda K and Ng T K 2017 *Rev. Mod. Phys.* **89** 025003
- [60] Sachdev S 2011 *Quantum Phase Transitions* (Cambridge Univ. Press)
- [61] Carr L D (ed) 2011 *Understanding Quantum Phase Transitions* (CRC Press)
- [62] Cavadini N, Heigold G, Henggeler W, Furrer A, Güdel H U, Krämer K and Mutka H 2000 *J. Phys.: Condens. Matter* **12** 5463–5472
- [63] Cavadini N, Heigold G, Henggeler W, Furrer A, Güdel H U, Krämer K and Mutka H 2001 *Phys. Rev. B* **63** 172414

- [64] Oosawa A, Kato T, Tanaka H, Kakurai K, Müller M and Mikeska H J 2002 *Phys. Rev. B* **65** 094426
- [65] Cavadini N, Henggeler W, Furrer A, Krämer K, Güdel H U, Mutka H, Wildes A and Vorderwisch P 2000 *Triplet Excitations in a Family of $S = 1/2$ Unconventional Antiferromagnets* in Furrer A (ed) *Neutron Scattering in Novel Materials* (Proc. of the 8th Summer School on Neutron Scattering, Zuoz, Switzerland) pp 237–251
- [66] Cavadini N, Rüegg C, Furrer A, Güdel H U, Krämer K, Mutka H and Vorderwisch P 2002 *Phys. Rev. B* **65** 132415
- [67] Matsumoto M, Normand B, Rice T M and Sigrist M 2002 *Phys. Rev. Lett.* **89** 077203
- [68] Rüegg C, Cavadini N, Furrer A, Güdel H U, Krämer K, Mutka H, Wildes A, Habicht K and Vorderwisch P 2003 *Nature* **423** 62–65
- [69] Chitov G Y, Ramakko B W and Azzouz M 2008 *Phys. Rev. B* **77** 224433
- [70] Fritz L, Doretto R L, Wessel S, Wenzel S, Burdin S and Vojta M 2011 *Phys. Rev. B* **83** 174416
- [71] Shastry B S and Sutherland B 1981 *Physica B+C* **108** 1069
- [72] Koga A and Kawakami N 2000 *Phys. Rev. Lett.* **84** 4461–4464
- [73] Johnston D C, Kremer R K, Troyer M, Wang X, Klümper A, Bud'ko S L, Panchula A F and Canfield P C 2000 *Phys. Rev. B* **61** 9558–9606
- [74] Dagotto E 1999 *Rep. Prog. Phys.* **62** 1525–1571
- [75] Batchelor M T, Guan X W, Oelkers N and Tsuboi Z 2007 *Adv. Phys.* **56** 465–543
- [76] Eccleston R S, Uehara M, Akimitsu J, Eisaki H, Motoyama N and Uchida S 1998 *Phys. Rev. Lett.* **81** 1702–1705
- [77] Kageyama H, Onizuka K, Ueda Y, Mushnikov N V, Goto T, Yoshimura K and Kosuge K 1998 *J. Phys. Soc. Jpn.* **67** 4304–4305
- [78] Kageyama H, Yoshimura K, Stern R, Mushnikov N V, Onizuka K, Kato M, Kosuge K, Slichter C P, Goto T and Ueda Y 1999 *Phys. Rev. Lett.* **82** 3168–3171
- [79] Corboz P and Mila F 2013 *Phys. Rev. B* **87** 115144
- [80] Janod E, Leonyuk L and Maltsev V 2000 *Sol. Stat. Commun.* **116** 513–518
- [81] Lebernegg S, Tsirlin A A, Janson O and Rosner H 2013 *Phys. Rev. B* **88** 224406
- [82] Canévet E, Fåk B, Kremer R K, Chun J H, Enderle M, Gordon E E, Bettis J L, Whangbo M H, Taylor J W and Adroja D T 2015 *Phys. Rev. B* **91** 060402
- [83] Goodenough J B 1955 *Phys. Rev.* **100** 564–573
- [84] Kanamori J 1959 *J. Phys. Chem. Solids* **10** 87
- [85] Anderson P W 1963 *Sol. State Phys.* **14** 99
- [86] Miyahara S, Fouet J B, Manmana S R, Noack R M, Mayaffre H, Sheikin I, Berthier C and Mila F 2007 *Phys. Rev. B* **75** 184402
- [87] Braden M, Wilkendorf G, Lorenzana J, Aïn M, McIntyre G J, Behruzi M, Heger G, Dhalenne G and Revcolevschi A 1996 *Phys. Rev. B* **54** 1105–1116
- [88] Lebernegg S, Tsirlin A A, Janson O and Rosner H 2014 *Phys. Rev. B* **89** 165127
- [89] Brunton G 1973 *Am. Mineral.* **58** 551
- [90] Burns P C, Eby R K and Hawthorne F C 1991 *Acta Cryst. C* **47** 916–919
- [91] Vergasova L P, Filatov S K, Gorskaya M G, Molchanov A A, Krivovichev S V and Ananiev V V 2000 *Eur. J. Mineral.* **12** 1041–1044
- [92] Krivovichev S V, Molchanov A V and Filatov S K 2000 *Crystallogr. Rep.* **45** 723–727
- [93] Vasiliev A N, Volkova O S, Zvereva E A, Koshelev A V, Urusov V S, Chareev D A, Petkov V I, Sukhanov M V, Rahaman B and Saha-Dasgupta T 2015 *Phys. Rev. B* **91** 144406
- [94] Ghose S, Fehlmann M and Sundaralingam M 1965 *Acta Crystallogr.* **18** 777
- [95] Eby K and Hawthorne F C 1990 *Acta Cryst. C* **46** 2291
- [96] Lebernegg S, Tsirlin A A, Janson O and Rosner H 2013 *Phys. Rev. B* **87** 235117
- [97] Mikeska H J and Kolezhuk A K 2004 *One-dimensional magnetism* in Schollwöck U, Richter J, Farnell D J J, and Bishop R F (eds) *Quantum Magnetism* (Lecture Notes in Physics vol **645**, Springer Berlin Heidelberg) pp 1–83
- [98] Lecheminant P 2013 *One-Dimensional Quantum Spin Liquids* in Diep H T (ed) *Frustrated Spin Systems* (World Scientific, Singapore) pp 321–381
- [99] Zhao L, Hung T L, Li C C, Chen Y Y, Wu M K, Kremer R K, Banks M G, Simon A, Whangbo M H, Lee C, Kim J S, Kim I and Kim K H 2012 *Adv. Mater.* **24** 2469

- [100] Lee C, Liu J, Whangbo M H, Koo H J, Kremer R K and Simon A 2012 *Phys. Rev. B* **86** 060407
- [101] Tolédano P, Ayala A P, Furtado Filho A F G, do Nascimento J P C, Silva M A S and Sombra A S B 2017 *J. Phys.: Condens. Matter* **29** 035701
- [102] Boehm M, Coad S, Roessli B, Zheludev A, Zolliker M, Böni P, Paul D M, Eisaki H, Motoyama N and Uchida S 1998 *Europhys. Lett.* **43** 77–82
- [103] de Graaf C, de P R Moreira I, Illas F, O I and Labarta A 2002 *Phys. Rev. B* **66** 014448
- [104] Xiang H J, Lee C and Whangbo M H 2007 *Phys. Rev. B* **76** 220411
- [105] Lorenz W E A, Kuzian R O, Drechsler S L, Stein W D, Wizent N, Behr G, Málek J, Nitzsche U, Rosner H, Hiess A, Schmidt W, Klingeler R, Loewenhaupt M and Büchner B 2009 *Europhys. Lett.* **88** 37002
- [106] Drechsler S L, Málek J, Lorenz W E A, Kuzian R O, Klingeler R, Nishimoto S, Nitzsche U, Knupfer M, Wizent N and Behr G 2010 *J. Phys.: Conf. Ser.* **200** 012028
- [107] Masuda T, Zheludev A, Bush A, Markina M and Vasiliev A 2004 *Phys. Rev. Lett.* **92** 177201
- [108] Masuda T, Zheludev A, Roessli B, Bush A, Markina M and Vasiliev A 2005 *Phys. Rev. B* **72** 014405
- [109] Park S, Choi Y J, Zhang C L and Cheong S W 2007 *Phys. Rev. Lett.* **98** 057601
- [110] Seki S, Yamasaki Y, Soda M, Matsuura M, Hirota K and Tokura Y 2008 *Phys. Rev. Lett.* **100** 127201
- [111] Drechsler S L, Richter J, Gippius A A, Vasiliev A, Bush A A, Moskvin A S, Málek J, Prots Y, Schnelle W and Rosner H 2006 *Europhys. Lett.* **73** 83–89
- [112] Enderle M, Mukherjee C, Fåk B, Kremer R K, Broto J M, Rosner H, Drechsler S L, Richter J, Malek J and Prokofiev A 2005 *Europhys. Lett.* **70** 237–243
- [113] Büttgen N, Krug von Nidda H A, Svistov L E, Prozorova L A, Prokofiev A and Aßmus W 2007 *Phys. Rev. B* **76** 014440
- [114] Büttgen N, Kraetschmer W, Svistov L E, Prozorova L A and Prokofiev A 2010 *Phys. Rev. B* **81** 052403
- [115] Mourigal M, Enderle M, Kremer R K, Law J M and Fåk B 2011 *Phys. Rev. B* **83** 100409
- [116] Nawa K, Takigawa M, Krämer S, Horvatić M, Berthier C, Yoshida M and Yoshimura K 2017 *Phys. Rev. B* **96** 134423
- [117] Dutton S E, Kumar M, Mourigal M, Soos Z G, Wen J J, Broholm C L, Andersen N H, Huang Q, Zbiri M, Toft-Petersen R and Cava R J 2012 *Phys. Rev. Lett.* **108** 187206
- [118] Drechsler S L, Volkova O, Vasiliev A N, Tristan N, Richter J, Schmitt M, Rosner H, Málek J, Klingeler R, Zvyagin A A and Büchner B 2007 *Phys. Rev. Lett.* **98** 077202
- [119] Vavilova E, Moskvin A S, Arango Y C, Sotnikov A, Drechsler S L, Klingeler R, Volkova O, Vasiliev A, Kataev V and Büchner B 2009 *Europhys. Lett.* **88** 27001
- [120] Sudan J, Lüscher A and Läuchli A M 2009 *Phys. Rev. B* **80** 140402
- [121] Chubukov A V 1991 *Phys. Rev. B* **44** 4693–4696
- [122] Agradipidis C E, Drechsler S L, van den Brink J and Nishimoto S 2018 *Coexistence of valence-bond formation and topological order in the frustrated ferromagnetic J_1 - J_2 chain* Preprint: arXiv:1806.08662 (unpublished)
- [123] Kecke L, Momoi T and Furusaki A 2007 *Phys. Rev. B* **76** 060407
- [124] Vekua T, Honecker A, Mikeska H J and Heidrich-Meisner F 2007 *Phys. Rev. B* **76** 174420
- [125] Hikihara T, Kecke L, Momoi T and Furusaki A 2008 *Phys. Rev. B* **78** 144404
- [126] Nishimoto S, Drechsler S L, Kuzian R, Richter J, Málek J, Schmitt M, van den Brink J and Rosner H 2012 *Europhys. Lett.* **98** 37007
- [127] Yakubovich O V, Simonov M A and Belov N V 1975 *Sov. Phys. Crystallogr.* **20** 87
- [128] Hoffmann C, Armbruster T and Kunz M 1997 *Eur. J. Mineral.* **9** 7
- [129] Li R K and Greaves C 2004 *Phys. Rev. B* **70** 132411
- [130] Li R, Li G and Greaves C 2018 *J. Mater. Chem. A* **6** 5260
- [131] Okamoto K, Tonegawa T and Kaburagi M 2003 *J. Phys.: Condens. Matter* **15** 5979–5995
- [132] Takano K, Kubo K and Sakamoto H 1996 *J. Phys.: Condens. Matter* **8** 6405–6411
- [133] Richter J, Ivanov N B and Schulenburg J 1998 *J. Phys.: Condens. Matter* **10** 3635–3649
- [134] Koga A, Okunishi K and Kawakami N 2000 *Phys. Rev. B* **62** 5558–5563
- [135] Verkholyak T and Strečka J 2016 *Phys. Rev. B* **94** 144410
- [136] Sakurai H, Yoshimura K, Kosuge K, Tsujii N, Abe H, Kitazawa H, Kido G, Michor H and Hilscher G 2002 *J. Phys. Soc. Jpn.* **71** 1161–1165

- [137] Zhou H D, Choi E S, Jo Y J, Balicas L, Lu J, Lumata L L, Urbano R R, Kuhns P L, Reyes A P, Brooks J S, Stillwell R, Tozer S W, Wiebe C R, Whalen J and Siegrist T 2010 *Phys. Rev. B* **82** 054435
- [138] Vekua T and Honecker A 2006 *Phys. Rev. B* **73** 214427
- [139] Dagotto E and Rice T M 1996 *Science* **271** 618–623
- [140] Majumdar C K and Ghosh D K 1969 *J. Math. Phys.* **10** 1399
- [141] Shastry B S and Sutherland B 1981 *Phys. Rev. Lett.* **47** 964–967
- [142] Lebernegg S, Janson O, Rousochatzakis I, Nishimoto S, Rosner H and Tsirlin A A 2017 *Phys. Rev. B* **95** 035145
- [143] Vergasova L P and Filatov S K 1983 *Doklady Akademii Nauk SSSR* **270** 415–417
- [144] Burns P C and Hawthorne F C 1993 *Amer. Mineral.* **78** 187–189
- [145] Stout J W and Chisholm R C 1962 *J. Chem. Phys.* **36** 979
- [146] Banks M G, Kremer R K, Hoch C, Simon A, Ouladdiaf B, Broto J M, Rakoto H, Lee C and Whangbo M H 2009 *Phys. Rev. B* **80** 024404
- [147] Schmitt M, Janson O, Schmidt M, Hoffmann S, Schnelle W, Drechsler S L and Rosner H 2009 *Phys. Rev. B* **79** 245119
- [148] van den Handel J, Gijssman H M and Poulis N J 1952 *Physica* **18** 862
- [149] Marshall W 1958 *J. Phys. Chem. Solids* **7** 159
- [150] Seki S, Kurumaji T, Ishiwata S, Matsui H, Murakawa H, Tokunaga Y, Kaneko Y, Hasegawa T and Tokura Y 2010 *Phys. Rev. B* **82** 064424
- [151] Katsura H, Nagaosa N and Balatsky A V 2005 *Phys. Rev. Lett.* **95** 057205
- [152] Mostovoy M 2006 *Phys. Rev. Lett.* **96** 067601
- [153] Sergienko I A and Dagotto E 2006 *Phys. Rev. B* **73** 094434
- [154] Tokura Y, Seki S and Nagaosa N 2014 *Rep. Prog. Phys.* **77** 076501
- [155] Pertlik F 1975 *Tschermaks Mineral. Petrog. Mitt.* **22** 211–217
- [156] Caslin K, Kremer R K, Razavi F S, Schulz A, Muñoz A, Pertlik F, Liu J, Whangbo M H and Law J M 2014 *Phys. Rev. B* **89** 014412
- [157] Caslin K, Kremer R K, Razavi F S, Hanfland M, Syassen K, Gordon E E and Whangbo M H 2016 *Phys. Rev. B* **93** 022301
- [158] Kuzian R O, Nishimoto S, Drechsler S L, Málek J, Johnston S, van den Brink J, Schmitt M, Rosner H, Matsuda M, Oka K, Yamaguchi H and Ito T 2012 *Phys. Rev. Lett.* **109** 117207
- [159] Wolter A U B, Lipps F, Schäpers M, Drechsler S L, Nishimoto S, Vogel R, Kataev V, Büchner B, Rosner H, Schmitt M, Uhlarz M, Skourski Y, Wosnitza J, Süllow S and Rule K C 2012 *Phys. Rev. B* **85** 014407
- [160] Kamieniarz G, Bieliński M, Szukowski G, Szymczak R, Dyeyev S and Renard J P 2002 *Comp. Phys. Commun.* **147** 716–719
- [161] Baran M, Jedrzejczak A, Szymczak H, Maltsev V, Kamieniarz G, Szukowski G, Loison C, Ormeci A, Drechsler S L and Rosner H 2006 *Phys. Stat. Sol. (c)* **3** 220–224
- [162] Schäpers M, Rosner H, Drechsler S L, Süllow S, Vogel R, Büchner B and Wolter A U B 2014 *Phys. Rev. B* **90** 224417
- [163] Rule K C, Willenberg B, Schäpers M, Wolter A U B, Büchner B, Drechsler S L, Ehlers G, Tenant D A, Mole R A, Gardner J S, Süllow S and Nishimoto S 2017 *Phys. Rev. B* **95** 024430
- [164] Cemal E, Enderle M, Kremer R K, Fåk B, Ressouche E, Gvozdikova M V, Zhitomirsky M E and Ziman T 2018 *Phys. Rev. Lett.* **120** 067203
- [165] Willenberg B, Schäpers M, Rule K C, Süllow S, Reehuis M, Ryll H, Klemke B, Kiefer K, Schottenhamel W, Büchner B, Ouladdiaf B, Uhlarz M, Beyer R, Wosnitza J and Wolter A U B 2012 *Phys. Rev. Lett.* **108** 117202
- [166] Schäpers M, Wolter A U B, Drechsler S L, Nishimoto S, Müller K H, Abdel-Hafiez M, Schottenhamel W, Büchner B, Richter J, Ouladdiaf B, Uhlarz M, Beyer R, Skourski Y, Wosnitza J, Rule K C, Ryll H, Klemke B, Kiefer K, Reehuis M, Willenberg B and Süllow S 2013 *Phys. Rev. B* **88** 184410
- [167] Willenberg B, Schäpers M, Wolter A U B, Drechsler S L, Reehuis M, Hoffmann J U, Büchner B, Studer A J, Rule K C, Ouladdiaf B, Süllow S and Nishimoto S 2016 *Phys. Rev. Lett.* **116** 047202
- [168] Povarov K Y, Feng Y and Zheludev A 2016 *Phys. Rev. B* **94** 214409
- [169] Yasui Y, Sato M and Terasaki I 2011 *J. Phys. Soc. Jpn.* **80** 033707
- [170] Yasui Y, Yanagisawa Y, Sato M and Terasaki I 2011 *J. Phys.: Conf. Ser.* **320** 012087

[171] Feng Y, Povarov K Y and Zheludev A 2018 *Three dimensional magnetic phase diagram of the strongly frustrated quantum spin chain system PbCuSO₄(OH)₂* Preprint: arXiv:1804.02215 (unpublished)

[172] Gattow G and Zemann J 1958 *Acta Cryst.* **11** 866–872

[173] Zigan F and Schuster H D 1972 *Z. Kristallogr.* **135** 416

[174] Belokoneva E L, Gubina Y K and Forsyth J B 2001 *Phys. Chem. Miner.* **28** 498–507

[175] Jeschke H, Opahle I, Kandpal H, Valentí R, Das H, Saha-Dasgupta T, Janson O, Rosner H, Brühl A, Wolf B, Lang M, Richter J, Hu S, Wang X, Peters R, Pruschke T and Honecker A 2011 *Phys. Rev. Lett.* **106** 217201

[176] Honecker A, Hu S, Peters R and Richter J 2011 *J. Phys.: Condens. Matter* **23** 164211

[177] Rule K C, Wolter A U B, Süllow S, Tennant D A, Brühl A, Köhler S, Wolf B, Lang M and Schreuer J 2008 *Phys. Rev. Lett.* **100** 117202

[178] Rule K C, Tennant D A, Caux J S, Gibson M C R, Telling M T F, Gerischer S, Süllow S and Lang M 2011 *Phys. Rev. B* **84** 184419

[179] Kikuchi H, Fujii Y, Chiba M, Mitsudo S, Idehara T, Tonegawa T, Okamoto K, Sakai T, Kuwai T, Kindo K, Matsuo A, Higemoto W, Nishiyama K, Horvatić M and Bertheir C 2005 *Prog. Theor. Phys.* **159** 1–10

[180] Aimo F, Krämer S, Klanjšek M, Horvatić M, Berthier C and Kikuchi H 2009 *Phys. Rev. Lett.* **102** 127205

[181] Ohta H, Okubo S, Kamikawa T, Kunimoto T, Inagaki Y, Kikuchi H, Saito T, Azuma M and Takano M 2003 *J. Phys. Soc. Jpn.* **72** 2464–2467

[182] Okubo S, Kamikawa T, Kunimoto T, Inagaki Y, Ohta H, Nojiri H and Kikuchi H 2004 *J. Magn. Magn. Mater.* **272–276** 912–913

[183] Kamenskyi D 2012 *Electron spin resonance studies of frustrated quantum spin systems* Ph.D. thesis TU Dresden

[184] Finney J J 1966 *Acta Cryst.* **21** 437–440

[185] Kikuchi H, Fujii Y, Takahashi D, Azuma M, Shimakawa Y, Taniguchi T, Matsuo A and Kindo K 2011 *J. Phys.: Conf. Ser.* **320** 012045

[186] Sen D, Shastry B S, Walstedt R E and Cava R 1996 *Phys. Rev. B* **53** 6401–6405

[187] Le Bacq O, Pasturel A, Lacroix C and Núñez Regueiro M D 2005 *Phys. Rev. B* **71** 014432

[188] Olariu A, Bono D, Bert F, Mendels P, Darie C, Bordet P, Hillier A D, Baines C and Amato A 2006 *Physica B: Condens. Matter* **374–375** 152–155

[189] Heritsch H 1938 *Z. Kristallogr.* **99** 466

[190] Fujihara M, Sugimoto T, Tohyama T, Mitsuda S, Mole R A, Yu D H, Yano S, Inagaki Y, Morodomi H, Kawae T, Sagayama H, Kumai R, Murakami Y, Tomiyasu K, Matsuo A and Kindo K 2018 *Phys. Rev. Lett.* **120** 077201

[191] Starova G L, Filatov S K, Fundamensky V S and Vergasova L P 1991 *Mineral. Mag.* **55** 613–616

[192] Masuda T, Zheludev A, Manaka H, Regnault L P, Chung J H and Qiu Y 2006 *Phys. Rev. Lett.* **96** 047210

[193] Janson O, Tsirlin A A, Schmitt M and Rosner H 2010 *Phys. Rev. B* **82** 014424

[194] Podlesnyak A, Anovitz L M, Kolesnikov A I, Matsuda M, Prisk T R, Toth S and Ehlers G 2016 *Phys. Rev. B* **93** 064426

[195] Heide H G and Boll-Dornberger K 1955 *Acta Cryst.* **8** 425

[196] Ribbe P H, Gibbs G V and Hamil M 1977 *Am. Mineral.* **62** 807–811

[197] Spence R D and Muller J H 1958 *J. Chem. Phys.* **29** 961

[198] Eisenberg W R and Forstat H 1964 *J. Phys. Soc. Jpn.* **19** 406

[199] Newnham R E and Santoro R P 1967 *Phys. Stat. Sol.* **19** K87

[200] Kiseleva I A, Ogorodova L P, Melchakova L V and Bisengalieva M R 1993 *J. Chem. Thermodyn.* **25** 621

[201] Wintenberger M, André G and Gardette M F 1993 *Sol. Stat. Commun.* **87** 309–312

[202] Belokoneva E L, Gubina Y K, Forsyth J B and Brown P J 2002 *Phys. Chem. Miner.* **29** 430

[203] Law J M, Hoch C, Whangbo M H and Kremer R K 2010 *Z. Anorg. Allg. Chem.* **636** 54

[204] Gros C, Lemmens P, Choi K Y, Güntherodt G, Baenitz M and Otto H H 2002 *Europhys. Lett.* **60** 276

[205] Berlie A and Terry I 2017 *Europhys. Lett.* **120** 47006

[206] Ohta H, Okubo S, Souda N, Tomoo M, Sakurai T, Yoshida Y, Ohmichi E, Fujisawa M, Tanaka H and Kato R 2009 *Appl. Magn. Reson.* **35** 399–410

[207] Burns P C 1998 *Mineral. Mag.* **62** 461–469

[208] Stolz J and Armbruster T 1998 *Neues Jahrb. Mineral. Monatsh.* (6) 278

[209] Vilminot S, Richard-Plouet M, André G, Swierczynski D, Guillot M, Bourée-Vigneron F and Drillon M 2003

J. Sol. Stat. Chem. **170** 255–264

[210] Vilminot S, André G, Bourée-Vigneron F, Richard-Plouet M and Kurmoo M 2007 *Inorg. Chem.* **46** 10079

[211] Bissengaliyeva M R, Bekturgenov N S, Gogol D B, Taimassova S T, Koketai T A and Bespyatov M A 2013 *J. Chem. Eng. Data* **58** 2904–2912

[212] Koo H J, Kremer R K and Whangbo M H 2012 *J. Phys. Soc. Jpn.* **81** 063704

[213] Fujisawa M, Kikuchi H, Fujii Y, Mitsudo S, Matsuo A and Kindo K 2011 *J. Phys.: Conf. Ser.* **320** 012031

[214] Fujii Y, Kikuchi H, Nakagawa K, Takada S and Fujisawa M 2015 *Phys. Procedia* **75** 589–596

[215] Fujii Y, Ishikawa Y, Kikuchi H, Narumi Y, Nojiri H, Hara S and Sato H 2013 *J. Korean Phys. Soc.* **62** 2054–2058

[216] Richter J, Schulenburg J and Honecker A 2004 *Quantum magnetism in two dimensions: From semi-classical Néel order to magnetic disorder* in Schollwöck U, Richter J, Farnell D J J, and Bishop R F (eds) *Quantum Magnetism* (Lecture Notes in Physics vol **645**, Springer Berlin Heidelberg) pp 85–153

[217] Farnell D J J, Götze O, Richter J, Bishop R F and Li P H Y 2014 *Phys. Rev. B* **89** 184407

[218] Yu U 2015 *Phys. Rev. E* **91** 062121

[219] Schmidt B and Thalmeier P 2017 *Phys. Rep.* **703** 1–59

[220] Richter J, Schulenburg J, Honecker A and Schmalfuß D 2004 *Phys. Rev. B* **70** 174454

[221] Zheng Y Z, Tong M L, Xue W, Zhang W X, Chen X M and F Grandjean G J L 2007 *Angew. Chem. Int. Ed.* **46** 6076–6080

[222] Choy T P and Kim Y B 2009 *Phys. Rev. B* **80** 064404

[223] Yang B J, Paramekanti A and Kim Y B 2010 *Phys. Rev. B* **81** 134418

[224] Okuma R, Yajima T, Nishio-Hamane D, Okubo T and Hiroi Z 2017 *Phys. Rev. B* **95** 094427

[225] Harris A B, Kallin C and Berlinsky A J 1992 *Phys. Rev. B* **45** 2899–2919

[226] Janson O, Richter J and Rosner H 2008 *Phys. Rev. Lett.* **101** 106403

[227] Suttorp R, Platt C, Reuther J and Thomale R 2014 *Phys. Rev. B* **89** 020408

[228] Iqbal Y, Jeschke H O, Reuther J, Valentí R, Mazin I I, Greiter M and Thomale R 2015 *Phys. Rev. B* **92** 220404

[229] Elhajal M, Canals B and Lacroix C 2002 *Phys. Rev. B* **66** 014422

[230] Ballou R, Canals B, Elhajal M, Lacroix C and Wills A S 2003 *J. Magn. Magn. Mater.* **262** 465–471

[231] Grohol D, Nocera D G and Papoutsakis D 2003 *Phys. Rev. B* **67** 064401

[232] Cépas O, Fong C M, Leung P W and Lhuillier C 2008 *Phys. Rev. B* **78** 140405

[233] Chalker J 2011 *Geometrically Frustrated Antiferromagnets: Statistical Mechanics and Dynamics* in Lacroix C, Mendels P, and Mila F (eds) *Introduction to Frustrated Magnetism* (Springer Series in Solid-State Sciences, vol **164**, 2nd ed, Springer-Verlag Berlin) pp 3–22

[234] Grohol D, Matan K, Cho J H, Lee S H, Lynn J W, Nocera D G and Lee Y S 2005 *Nature Mater.* **4** 323–328

[235] Townsend M G, Longworth G and Roudaut E 1986 *Phys. Rev. B* **33** 4919–4926

[236] Nishiyama M, Morimoto T, Maegawa S, Inami T and Oka Y 2001 *Canad. J. Phys.* **79** 1511–1516

[237] Okuta K, Hara S, Sato H, Narumi Y and Kindo K 2011 *J. Phys. Soc. Jpn.* **80** 063703

[238] Misguich G and Lhuillier C 2013 *Two-Dimensional Quantum Antiferromagnets* in Diep H T (ed) *Frustrated Spin Systems* (World Scientific, Singapore) pp 235–319

[239] Liao H J, Xie Z Y, Chen J, Liu Z Y, Xie H D, Huang R Z, Normand B and Xiang T 2017 *Phys. Rev. Lett.* **118** 137202

[240] Fåk B, Kermarrec E, Messio L, Bernu B, Lhuillier C, Bert F, Mendels P, Koteswararao B, Bouquet F, Ollivier J, Hillier A D, Amato A, Colman R H and Wills A S 2012 *Phys. Rev. Lett.* **109** 037208

[241] Bernu B, Lhuillier C, Kermarrec E, Bert F, Mendels P, Colman R and Wills A S 2013 *Phys. Rev. B* **87** 155107

[242] Yildirim T and Harris A B 2006 *Phys. Rev. B* **73** 214446

[243] Wang F, Vishwanath A and Kim Y B 2007 *Phys. Rev. B* **76** 094421

[244] Kaneko R, Misawa T and Imada M 2010 *J. Phys. Soc. Jpn.* **79** 073708

[245] Masuda H, Okubo T and Kawamura H 2012 *Phys. Rev. Lett.* **109** 057201

[246] Dommange S, Mambrini M, Normand B and Mila F 2003 *Phys. Rev. B* **68** 224416

[247] Läuchli A, Dommange S, Normand B and Mila F 2007 *Phys. Rev. B* **76** 144413

[248] Bert F, Bono D, Mendels P, Ladieu F, Duc F, Trombe J C and Millet P 2005 *Phys. Rev. Lett.* **95** 087203

[249] Yoshida M, Takigawa M, Yoshida H, Okamoto Y and Hiroi Z 2009 *Phys. Rev. Lett.* **103** 077207

[250] Yoshida M, Takigawa M, Krämer S, Mukhopadhyay S, Horvatić M, Berthier C, Yoshida H, Okamoto Y and Hiroi

Z 2012 *J. Phys. Soc. Jpn.* **81** 024703

[251] Okamoto Y, Yoshida H and Hiroi Z 2009 *J. Phys. Soc. Jpn.* **78** 033701

[252] Okamoto Y, Ishikawa H, Nilsen G J and Hiroi Z 2012 *J. Phys. Soc. Jpn.* **81** 033707

[253] Boldrin D, Knight K and Wills A S 2016 *J. Mater. Chem. C* **4** 10315–10322

[254] Wills A S 2001 *Phys. Rev. B* **63** 064430

[255] Katoa M, Horia T, Obaa N, Yoshimuraa K and Goto T 2003 *Physica B: Condens. Matter* **329–333** 1042–1043

[256] Okubo S, Nakata R, Ikeda S, Takahashi N, Sakurai T, Zhang W M, Ohta H, Shimokawa T, Sakai T, Okuta K, Hara S and Sato H 2017 *J. Phys. Soc. Jpn.* **86** 024703

[257] Buurma A J C, Handayani I P, Mufti N, Blake G R, van Loosdrecht P H M and Palstra T T M 2012 *J. Sol. Stat. Chem.* **195** 50–54

[258] Inami T, Maegawa S and Takano M 1998 *J. Magn. Magn. Mater.* **177–181** 752–753

[259] Inami T, Nishiyama M, Maegawa S and Oka Y 2000 *Phys. Rev. B* **61** 12181–12186

[260] Nishiyama M, Maegawa S, Inami T and Oka Y 2003 *Phys. Rev. B* **67** 224435

[261] Matan K, Bartlett B M, Helton J S, Sikolenko V, Mat'aš S, Prokeš K, Chen Y, Lynn J W, Grohol D, Sato T J, Tokunaga M, Nocera D G and Lee Y S 2011 *Phys. Rev. B* **83** 214406

[262] Fujita T, Yamaguchi H, Kimura S, Kashiwagi T, Hagiwara M, Matan K, Grohol D, Nocera D G and Lee Y S 2012 *Phys. Rev. B* **85** 094409

[263] Matan K, Grohol D, Nocera D G, Yildirim T, Harris A B, Lee S H, Nagler S E and Lee Y S 2006 *Phys. Rev. Lett.* **96** 247201

[264] Coomer F C, Harrison A, Oakley G S, Kulda J, Stewart J R, Stride J A, Fåk B, Taylor J W and Visser D 2006 *J. Phys.: Condens. Matter* **18** 8847–8858

[265] de Vries M A, Johal T K, Mirone A, Claydon J S, Nilsen G J, Rønnow H M, van der Laan G and Harrison A 2009 *Phys. Rev. B* **79** 045102

[266] Matan K, Helton J S, Grohol D, Nocera D G, Wakimoto S, Kakurai K and Lee Y S 2009 *Physica B: Condens. Matter* **404** 2529–2531

[267] Freitas A S and de Albuquerque D F 2015 *Phys. Rev. E* **91** 012117

[268] Braithwaite R S W, Mereiter K, Paar W H and Clark A M 2004 *Mineral. Mag.* **68** 527–539

[269] Shores M P, Nytko E A, Bartlett B M and Nocera D G 2005 *J. Am. Chem. Soc.* **127** 13462–13463

[270] Chu S, Müller P, Nocera D G and Lee Y S 2011 *Appl. Phys. Lett.* **98** 092508

[271] Han T H, Helton J S, Chu S, Prodi A, Singh D K, Mazzoli C, Müller P, Nocera D G and Lee Y S 2011 *Phys. Rev. B* **83** 100402

[272] Han T H, Helton J S, Chu S, Nocera D G, Rodriguez-Rivera J A, Broholm C and Lee Y S 2012 *Nature* **492** 406–410

[273] Rigol M and Singh R R P 2007 *Phys. Rev. Lett.* **98** 207204

[274] Misguich G and Sindzingre P 2007 *Eur. Phys. J. B* **59** 305–309

[275] Mendels P, Bert F, de Vries M A, Olariu A, Harrison A, Duc F, Trombe J C, Lord J S, Amato A and Baines C 2007 *Phys. Rev. Lett.* **98** 077204

[276] Helton J S, Matan K, Shores M P, Nytko E A, Bartlett B M, Yoshida Y, Takano Y, Suslov A, Qiu Y, Chung J H, Nocera D G and Lee Y S 2007 *Phys. Rev. Lett.* **98** 107204

[277] Imai T, Nytko E A, Bartlett B M, Shores M P and Nocera D G 2008 *Phys. Rev. Lett.* **100** 077203

[278] Zorko A, Nellutla S, van Tol J, Brunel L C, Bert F, Duc F, Trombe J C, de Vries M A, Harrison A and Mendels P 2008 *Phys. Rev. Lett.* **101** 026405

[279] Han T, Chu S and Lee Y S 2012 *Phys. Rev. Lett.* **108** 157202

[280] Jeschke H O, Salvat-Pujol F and Valentí R 2013 *Phys. Rev. B* **88** 075106

[281] Nilsen G J, de Vries M A, Stewart J R, Harrison A and Rønnow H M 2013 *J. Phys.: Condens. Matter* **25** 106001

[282] Kozlenko D P, Kusmartseva A F, Lukin E V, Keen D A, Marshall W G, de Vries M A and Kamenev K V 2012 *Phys. Rev. Lett.* **108** 187207

[283] Nikolic P and Senthil T 2003 *Phys. Rev. B* **68** 214415

[284] Hermele M, Ran Y, Lee P A and Wen X G 2008 *Phys. Rev. B* **77** 224413

[285] Anderson P W 1973 *Mater. Res. Bull.* **8** 153

[286] Mambrinia M and Mila F 2000 *Eur. Phys. J. B* **17** 651–659

- [287] Fu M, Imai T, Han T H and Lee Y S 2015 *Science* **350** 655–658
- [288] Sherman N E, Imai T and Singh R R P 2016 *Phys. Rev. B* **94** 140415
- [289] Jiang H C, Weng Z Y and Sheng D N 2008 *Phys. Rev. Lett.* **101** 117203
- [290] Yan S, Huse D A and White S R 2011 *Science* **332** 1173–1176
- [291] Depenbrock S, McCulloch I P and Schollwöck U 2012 *Phys. Rev. Lett.* **109** 067201
- [292] Jiang H C, Wang Z and Balents L 2012 *Nature Phys.* **8** 902–905
- [293] Messio L, Bernu B and Lhuillier C 2012 *Phys. Rev. Lett.* **108** 207204
- [294] Nishimoto S, Shibata N and Hotta C 2013 *Nature Commun.* **4** 2287
- [295] Ju H and Balents L 2013 *Phys. Rev. B* **87** 195109
- [296] Dodds T, Bhattacharjee S and Kim Y B 2013 *Phys. Rev. B* **88** 224413
- [297] Iqbal Y, Poilblanc D and Becca F 2015 *Phys. Rev. B* **91** 020402
- [298] Marston J B and Zeng C 1991 *J. Appl. Phys.* **69** 5962
- [299] Singh R R P and Huse D A 1992 *Phys. Rev. Lett.* **68** 1766–1769
- [300] Elstner N and Young A P 1994 *Phys. Rev. B* **50** 6871–6876
- [301] Lecheminant P, Bernu B, Lhuillier C, Pierre L and Sindzingre P 1997 *Phys. Rev. B* **56** 2521–2529
- [302] Waldtmann C, Everts H U, Bernu B, Lhuillier C, Sindzingre P, Lecheminant P and Pierre L 1998 *Eur. Phys. J. B* **2** 501–507
- [303] Mila F 1998 *Phys. Rev. Lett.* **81** 2356–2359
- [304] Syromyatnikov A V and Maleyev S V 2002 *Phys. Rev. B* **66** 132408
- [305] Budnik R and Auerbach A 2004 *Phys. Rev. Lett.* **93** 187205
- [306] Wang F and Vishwanath A 2006 *Phys. Rev. B* **74** 174423
- [307] Ran Y, Hermele M, Lee P A and Wen X G 2007 *Phys. Rev. Lett.* **98** 117205
- [308] Singh R R P and Huse D A 2007 *Phys. Rev. B* **76** 180407
- [309] Nakano H and Sakai T 2011 *J. Phys. Soc. Jpn.* **80** 053704
- [310] Iqbal Y, Becca F, Sorella S and Poilblanc D 2013 *Phys. Rev. B* **87** 060405
- [311] Iqbal Y, Poilblanc D and Becca F 2014 *Phys. Rev. B* **89** 020407
- [312] Messio L, Bieri S, Lhuillier C and Bernu B 2017 *Phys. Rev. Lett.* **118** 267201
- [313] Shimokawa T, Watanabe K and Kawamura H 2015 *Phys. Rev. B* **92** 134407
- [314] Han T H, Norman M R, Wen J J, Rodriguez-Rivera J A, Helton J S, Broholm C and Lee Y S 2016 *Phys. Rev. B* **94** 060409
- [315] Helton J S, Matan K, Shores M P, Nytko E A, Bartlett B M, Qiu Y, Nocera D G and Lee Y S 2010 *Phys. Rev. Lett.* **104** 147201
- [316] Imai T, Fu M, Han T H and Lee Y S 2011 *Phys. Rev. B* **84** 020411
- [317] Freedman D E, Han T H, Prodi A, Müller P, Huang Q Z, Chen Y S, Webb S M, Lee Y S, McQueen T M and Nocera D G 2010 *J. Am. Chem. Soc.* **132** 16185–16190
- [318] Keimer B, Birgeneau R J, Cassanho A, Endoh Y, Erwin R W, Kastner M A and Shirane G 1991 *Phys. Rev. Lett.* **67** 1930–1933
- [319] Park J G, McEwen D T A K A and Murani A P 2002 *J. Phys.: Condens. Matter* **14** 3865–3873
- [320] Aronson M C, Osborn R, Robinson R A, Lynn J W, Chau R, Seaman C L and Maple M B 1995 *Phys. Rev. Lett.* **75** 725–728
- [321] Schröder A, Aepli G, Coldea R, Adams M, Stockert O, v Löhneysen H, Bucher E, Ramazashvili R and Coleman P 2000 *Nature* **407** 351–355
- [322] Schröder A, Aepli G, Bucher E, Ramazashvili R and Coleman P 1998 *Phys. Rev. Lett.* **80** 5623–5626
- [323] Sachdev S 2008 *Nature Phys.* **4** 173–185
- [324] Griffiths R B 1969 *Phys. Rev. Lett.* **23** 17–19
- [325] Castro Neto A H, Castilla G and Jones B A 1998 *Phys. Rev. Lett.* **81** 3531–3534
- [326] Bhatt R N and Lee P A 1982 *Phys. Rev. Lett.* **48** 344–347
- [327] Sushkov A B, Jenkins G S, Han T H, Lee Y S and Drew H D 2017 *J. Phys.: Condens. Matter* **29** 095802
- [328] Zorko A, Herak M, Gomilšek M, van Tol J, Velázquez M, Khuntia P, Bert F and Mendels P 2017 *Phys. Rev. Lett.* **118** 017202
- [329] Colman R H, Sinclair A and Wills A S 2011 *Chem. Mater.* **23** 1811–1817

[330] Malcherek T, Bindi L, Dini M, Ghiara M R, Donoso A M, Nestola F, Rossi M and Schlüter J 2014 *Mineral. Mag.* **78** 583–590

[331] Clissold M E, Leverett P, Williams P A, Hibbs D E and Nickel E H 2007 *Can. Mineral.* **45** 317–320

[332] Kampf A R, Sciberras M J, Williams P A, Dini M and Donoso A A M 2013 *Mineral. Mag.* **77** 3047–3054

[333] Kermarrec E, Mendels P, Bert F, Colman R H, Wills A S, Strobel P, Bonville P, Hillier A and Amato A 2011 *Phys. Rev. B* **84** 100401

[334] Li Y S and Zhang Q M 2013 *J. Phys.: Condens. Matter* **25** 026003

[335] Colman R H, Ritter C and Wills A S 2008 *Chem. Mater.* **20** 6897–6899

[336] Colman R H, Sinclair A and Wills A S 2010 *Chem. Mater.* **22** 5774–5779

[337] Nilsen G J, Simonet V, Colin C V, Okuma R, Okamoto Y, Tokunaga M, Hansen T C, Khalyavin D D and Hiroi Z 2017 *Phys. Rev. B* **95** 214415

[338] Kermarrec E, Zorko A, Bert F, Colman R H, Koteswararao B, Bouquet F, Bonville P, Hillier A, Amato A, van Tol J, Ozarowski A, Wills A S and Mendels P 2014 *Phys. Rev. B* **90** 205103

[339] Boldrin D, Fåk B, Enderle M, Bieri S, Ollivier J, Rols S, Manuel P and Wills A S 2015 *Phys. Rev. B* **91** 220408

[340] Puphal P, Bolte M, Sheptyakov D, Pustogow A, Kliemt K, Dressel M, Baenitz M and Krellner C 2017 *J. Mater. Chem. C* **5** 2629–2635

[341] Schlüter J and Malcherek T 2007 *Neues Jahrb. Mineral. Abhandl.* **184** 39–43

[342] Nishio-hamane D, Momma K, Ohnishi M, Shimobayashi N, Miyawaki R, Tomita N, Okuma R, Kampf A R and Minakawa T 2017 *Mineral. Mag.* **81** 485–498

[343] Domenge J C, Sindzingre P, Lhuillier C and Pierre L 2005 *Phys. Rev. B* **72** 024433

[344] Bieri S, Messio L, Bernu B and Lhuillier C 2015 *Phys. Rev. B* **92** 060407

[345] Bieri S, Lhuillier C and Messio L 2016 *Phys. Rev. B* **93** 094437

[346] Oswald H R 1969 *Helv. Chim. Acta* **52** 2369

[347] Yoshida H, Noguchi N, Matsushita Y, Ishii Y, Ihara Y, Oda M, Okabe H, Yamashita S, Nakazawa Y, Takata A, Kida T, Narumi Y and Hagiwara M 2017 *J. Phys. Soc. Jpn.* **86** 033704

[348] Crichton W A and Müller H 2017 *Mineral. Mag.* **81** 1105–1124

[349] Sun W, Huang Y X, Pan Y and Mi J X 2016 *Phys. Chem. Miner.* **43** 127–136

[350] Burns P C, Pluth J J, Smith J V, Eng P, Steele I and Housley R M 2000 *American Mineralogist* **85** 604–607

[351] Norman M R 2018 *J. Magn. Magn. Mater.* **452** 507–511

[352] Hiroi Z, Hanawa M, Kobayashi N, Nohara M, Takagi H, Kato Y and Takigawa M 2001 *J. Phys. Soc. Jpn.* **70** 3377–3384

[353] Okubo S, Ohta H, Hazuki K, Sakurai T, Kobayashi N and Hiroi Z 2001 *Physica B: Condens. Matter* **294–295** 75–78

[354] Fukaya A, Fudamoto Y, Gat I M, Ito T, Larkin M I, Savici A T, Uemura Y J, Kyriakou P P, Luke G M, Rovers M T, Kojima K M, Keren A, Hanawa M and Hiroi Z 2003 *Phys. Rev. Lett.* **91** 207603

[355] Yoshida H, Okamoto Y, Tayama T, Sakakibara T, Tokunaga M, Matsuo A, Narumi Y, Kindo K, Yoshida M, Takigawa M and Hiroi Z 2009 *J. Phys. Soc. Jpn.* **78** 043704

[356] Okamoto Y, Tokunaga M, Yoshida H, Matsuo A, Kindo K and Hiroi Z 2011 *Phys. Rev. B* **83** 180407

[357] Schnyder A P, Starykh O A and Balents L 2008 *Phys. Rev. B* **78** 174420

[358] Janson O, Richter J, Sindzingre P and Rosner H 2010 *Phys. Rev. B* **82** 104434

[359] Nilsen G J, Coomer F C, de Vries M A, Stewart J R, Deen P P, Harrison A and Rønnow H M 2011 *Phys. Rev. B* **84** 172401

[360] Yoshida H, Yamaura J i, Isobe M, Okamoto Y, Nilsen G J and Hiroi Z 2012 *Nature Commun.* **3** 860

[361] Yamashita S, Moriura T, Nakazawa Y, Yoshida H, Okamoto Y and Hiroi Z 2010 *J. Phys. Soc. Jpn.* **79** 083710

[362] Sugawara K, Sugimoto K, Fujii T, Higuchi T, Katayama N, Okamoto Y and Sawa H 2018 *J. Phys. Soc. Jpn.* **87** 024601

[363] Ishikawa H, Yamaura J, Okamoto Y, Yoshida H, Nilsen G J and Hiroi Z 2012 *Acta Cryst. C* **68** i41–i44

[364] Janson O, Furukawa S, Momoi T, Sindzingre P, Richter J and Held K 2016 *Phys. Rev. Lett.* **117** 037206

[365] Ishikawa H, Yoshida M, Nawa K, Jeong M, Krämer S, Horvatić M, Berthier C, Takigawa M, Akaki M, Miyake A, Tokunaga M, Kindo K, Yamaura J, Okamoto Y and Hiroi Z 2015 *Phys. Rev. Lett.* **114** 227202

[366] Chern L E, Schaffer R, Sorn S and Kim Y B 2017 *Phys. Rev. B* **96** 165117

- [367] Watanabe D, Sugii K, Shimozawa M, Suzuki Y, Yajima T, Ishikawa H, Hiroi Z, Shibauchi T, Matsuda Y and Yamashita M 2016 *Proc. Nat. Acad. Sci. USA* **113** 8653–8657
- [368] Katsura H, Nagaosa N and Lee P A 2010 *Phys. Rev. Lett.* **104** 066403
- [369] Yoshida M, Nawa K, Ishikawa H, Takigawa M, Jeong M, Krämer S, Horvatić M, Berthier C, Matsui K, Goto T, Kimura S, Sasaki T, Yamaura J, Yoshida H, Okamoto Y and Hiroi Z 2017 *Phys. Rev. B* **96** 180413
- [370] Nilsen G J, Okamoto Y, Ishikawa H, Simonet V, Colin C V, Cano A, Chapon L C, Hansen T, Mutka H and Hiroi Z 2014 *Phys. Rev. B* **89** 140412
- [371] Guillemin C 1955 *C. R. Hebd. Séances Acad. Sci.* **240** 2331–2333
- [372] Ma Z, He R and Zhu X 1990 *Acta Geol. Sinica* **64** 302–308
- [373] Yoshida H, Michiue Y, Takayama-Muromachi E and Isobe M 2012 *J. Mater. Chem.* **22** 18793
- [374] Yoshida M, Okamoto Y, Takigawa M and Hiroi Z 2013 *J. Phys. Soc. Jpn.* **82** 013702
- [375] Colman R H, Bert F, Boldrin D, Hillier A D, Manuel P, Mendels P and Wills A S 2011 *Phys. Rev. B* **83** 180416
- [376] Zhang W M, Ohta H, Okubo S, Fujisawa M, Sakurai T, Okamoto Y, Yoshida H and Hiroi Z 2010 *J. Phys. Soc. Jpn.* **79** 023708
- [377] Quilliam J A, Bert F, Colman R H, Boldrin D, Wills A S and Mendels P 2011 *Phys. Rev. B* **84** 180401
- [378] El Shawish S, Cépas O and Miyashita S 2010 *Phys. Rev. B* **81** 224421
- [379] Zorko A, Bert F, Ozarowski A, van Tol J, Boldrin D, Wills A S and Mendels P 2013 *Phys. Rev. B* **88** 144419
- [380] Owerre S A 2017 *Europhys. Lett.* **117** 37006
- [381] Boldrin D, Fåk B, Canévet E, Ollivier J, Walker H C, Manuel P, Khalyavin D and Wills A S 2018 *Vesignieite: a $S = 1/2$ kagomé antiferromagnet with dominant third-neighbor exchange* Preprint: arXiv:1806.03074 (unpublished)
- [382] Elliott P, Brugger J and Caradoc-Davies T 2010 *Mineral. Mag.* **74** 39–53
- [383] Ishikawa H, Okamoto Y and Hiroi Z 2013 *J. Phys. Soc. Jpn.* **82** 063710
- [384] Fujihala M, Zheng X G, Morodomi H, Kawae T, Matsuo A, Kindo K and Watanabe I 2014 *Phys. Rev. B* **89** 100401
- [385] Messio L, Lhuillier C and Misguich G 2011 *Phys. Rev. B* **83** 184401
- [386] Boldrin D and Wills A S 2015 *J. Mater. Chem. C* **3** 4308
- [387] Ishikawa H, Yajima T, Miyake A, Tokunaga M, Matsuo A, Kindo K and Hiroi Z 2017 *Chem. Mater.* **29** 6719–6725
- [388] Ghose B S and Wan C 1979 *Acta Cryst.* **B35** 819–823
- [389] Burns P C and Hawthorne F C 1996 *The Canadian Mineralogist* **34** 1089–1105
- [390] Pekov I V, Siidra O I, Chukanov N V, Yapaskurt V O, Britvin S N, Krivovichev S V, Schüller W and Ternes B 2015 *Miner. Petrol.* **109** 705–711
- [391] Pring A, Gatehouse B M and Birch W D 1990 *Am. Mineral.* **75** 1421
- [392] Nazarchuk E V, Krivovichev S V, Pankratova O Y and Filatov S K 2000 *Phys. Chem. Miner.* **27** 440–444
- [393] Millet P, Bastide B, Pashchenko V, Gnatchenko S, Gapon V, Ksari Y and Stepanov A 2001 *J. Mater. Chem.* **11** 1152–1157
- [394] Constable E, Raymond S, Petit S, Ressouche E, Bourdarot F, Debray J, Josse M, Fabelo O, Berger H, de Brion S and Simonet V 2017 *Phys. Rev. B* **96** 014413
- [395] Gnedilov V, Pashkevich Y, Lemmens P, Kurnosov V, Berdonosov P, Dolgikh V, Kuznetsova E, Pryadun V, Zakharov K and Vasiliev A 2017 *Phys. Rev. B* **96** 115144
- [396] Miller K H, Stephens P W, Martin C, Constable E, Lewis R A, Berger H, Carr G L and Tanner D B 2012 *Phys. Rev. B* **86** 174104
- [397] Pregelj M, Zaharko O, Günther A, Loidl A, Tsurkan V and Guerrero S 2012 *Phys. Rev. B* **86** 144409
- [398] Prishchenko D A, Tsirlin A A, Tsurkan V, Loidl A, Jesche A and Mazurenko V G 2017 *Phys. Rev. B* **95** 064102
- [399] Rousouchatzakis I, Richter J, Zinke R and Tsirlin A A 2015 *Phys. Rev. B* **91** 024416
- [400] Nikolaev S A, Mazurenko V V, Tsirlin A A and Mazurenko V G 2016 *Phys. Rev. B* **94** 144412
- [401] Wu H C, Chandrasekhar K D, Yuan J K, Huang J R, Lin J Y, Berger H and Yang H D 2017 *Phys. Rev. B* **95** 125121
- [402] Zakharov K V, Zvereva E A, Berdonosov P S, Kuznetsova E S, Dolgikh V A, Clark L, Black C, Lightfoot P, Kockelmann W, Pchelkina Z V, Streletsov S V, Volkova O S and Vasiliev A N 2014 *Phys. Rev. B* **90** 214417
- [403] Zakharov K V, Zvereva E A, Kuznetsova E S, Berdonosov P S, Dolgikh V A, Markina M M, Olenev A V, Shakin A A, Volkova O S and Vasiliev A N 2016 *J. Alloy. Compd.* **685** 442–447
- [404] Markina M M, Zakharov K V, Zvereva E A, Denisov R S, Berdonosov P S, Dolgikh V A, Kuznetsova E S, Olenev

A V and Vasiliev A N 2017 *Phys. Chem. Miner.* **44** 277–285

[405] Zakharov K V, Zvereva E A, Markina M M, Stratan M I, Kuznetsova E S, Dunaev S F, Berdonosov P S, Dolgikh V A, Olenev A V, Klimin S A, Mazaev L S, Kashchenko M A, Ahmed M A, Banerjee A, Bandyopadhyay S, Iqbal A, Rahaman B, Saha-Dasgupta T and Vasiliev A N 2016 *Phys. Rev. B* **94** 054401

[406] Vilminot S, Richard-Plouet M, André G, Swierczynski D, Bourée-Vigneron F and Kurmoo M 2006 *Dalton Trans.* **11** 1455–1462

[407] Gomilšek M, Klanjšek M, Žitko R, Pregelj M, Bert F, Mendels P, Li Y, Zhang Q M and Zorko A 2017 *Phys. Rev. Lett.* **119** 137205

[408] Li Y, Pan B, Li S, Tong W, Ling L, Yang Z, Wang J, Chen Z, Wu Z and Zhang Q 2014 *New J. Phys.* **16** 093011

[409] Gomilšek M, Klanjšek M, Pregelj M, Coomer F C, Luetkens H, Zaharko O, Fennell T, Li Y, Zhang Q M and Zorko A 2016 *Phys. Rev. B* **93** 060405

[410] Gomilšek M, Klanjšek M, Pregelj M, Luetkens H, Li Y, Zhang Q M and Zorko A 2016 *Phys. Rev. B* **94** 024438

[411] Fejer E E, Clark A M, Couper A G and Elliott C J 1977 *Mineral. Mag.* **41** 433–436

[412] Burns P C, Cooper M A and Hawthorne F C 1995 *Canad. Mineral.* **33** 633–639

[413] Elliot P and Cooper M 2010 *Mineral. Mag.* **74** 797

[414] Elliott P, Cooper M A and Pring A 2014 *Mineral. Mag.* **78** 1755–1762

[415] Jeschke H O, Salvat-Pujol F, Gati E, Hoang N H, Wolf B, Lang M, Schlueter J A and Valentí R 2015 *Phys. Rev. B* **92** 094417

[416] Han T H, Singleton J and Schlueter J A 2014 *Phys. Rev. Lett.* **113** 227203

[417] Han T H, Isaacs E D, Schlueter J A and Singleton J 2016 *Phys. Rev. B* **93** 214416

[418] Ranjith K M, Klein C, Tsirlin A A, Rosner H, Krellner C and Baenitz M 2018 *Magnetic resonance as a local probe for kagomé magnetism in barlowite Cu₄(OH)₆FB_r* Preprint: arXiv:1804.00893 (unpublished)

[419] Liu Z, Zou X, Mei J W and Liu F 2015 *Phys. Rev. B* **92** 220102

[420] Guterding D, Valentí R and Jeschke H O 2016 *Phys. Rev. B* **94** 125136

[421] Feng Z, Li Z, Meng X, Yi W, Wei Y, Zhang J, Wang Y C, Jiang W, Liu Z, Li S, Liu F, Luo J, Li S, Zheng G q, Meng Z Y, Mei J W and Shi Y 2017 *Chin. Phys. Lett.* **34** 077502

[422] Feng Z, Yi W, Zhu K, Ma J, Luo J, Li S, Meng Z Y and Shi Y 2018 *From claringbullite to a new spin liquid candidate Cu₃Zn(OH)₆FC_l* Preprint: arXiv:1806.00803 (unpublished)

[423] Feng Z, Wei Y, Liu R, Yan D, Wang Y C, Luo J, Senyshyn A, dela Cruz C, Yi W, Mei J W, Meng Z Y, Shi Y and Li S 2017 *Effect of Zn doping on the antiferromagnetism in kagomé Cu_{4-x}Zn_x(OH)₆FB_r* Preprint: arXiv:1712.06732 (unpublished)

[424] Tsirlin A A, Janson O, Lebernegg S and Rosner H 2013 *Phys. Rev. B* **87** 064404

[425] Tomczak P, Schulenburg J, Richter J and Ferchmin A R 2001 *J. Phys.: Condens. Matter* **13** 3851–3857

[426] Taniguchi S, Nishikawa T, Yasui Y, Kobayashi Y, Sato M, Nishioka T, Kontani M and Sano K 1995 *J. Phys. Soc. Jpn.* **64** 2758–2761

[427] Jagannathan A, Moessner R and Wessel S 2006 *Phys. Rev. B* **74** 184410

[428] Valdés J F, Lebrecht W and Vogel E E 2007 *Physica A: Stat. Mech. Appl.* **385** 551–557

[429] Isobe M, Koishi S, Kouno N, Yamaura J I, Yamauchi T, Ueda H, Gotou H, Yagi T and Ueda Y 2006 *J. Phys. Soc. Jpn.* **75** 073801

[430] Miura H 1986 *Mineral. J. Jpn.* **13** 119–129

[431] Schmalfuß D, Tomczak P, Schulenburg J and Richter J 2002 *Phys. Rev. B* **65** 224405

[432] Cave D, Coomer F C, Molinos E, Klauss H H and Wood P T 2006 *Angew. Chem. Int. Ed.* **45** 803–806

[433] Merlini S, Pasero M, Sabelli C and Trosti-Ferroni R 1992 *Neues Jahrb. Mineral. Monatsh.* (8) 349–357

[434] Olmi F, Sabelli C and Trosti-Ferroni R 1995 *Eur. J. Mineral.* **7** 1331

[435] Kampf A R, Mills S J, Housley R M and Marty J 2013 *Amer. Mineral.* **98** 506

[436] Mills S J, Kampf A R, Christy A G, Housley R M, Rossman G R, Reynolds R E and Marty J 2014 *Mineral. Mag.* **78** 1325–1340

[437] Farnell D J J, Darradi R, Schmidt R and Richter J 2011 *Phys. Rev. B* **84** 104406

[438] Ohtani T, Honjo H and Wada H 1987 *Mat. Res. Bull.* **22** 829–840

[439] Kipp D O and Vanderah T A 1990 *Mat. Res. Bull.* **25** 933–937

[440] Pabst A 1938 *Am. Mineral.* **23** 175–176

- [441] Dannhauser W and Vaughan P A 1955 *J. Am. Chem. Soc.* **77** 896–897
- [442] Muir A H and Wiedersich H 1967 *J. Phys. Chem. Solids* **28** 65–71
- [443] Apostolov A 1969 *C. R. Acad. Sc. Bulgarie* **22** 11
- [444] Doumerc J P, Wichainchai A, Ammar A, Pouchard M and Hagenmuller P 1986 *Mat. Res. Bull.* **21** 745–752
- [445] Mitsuda S, Yoshizawa H, Yaguchi N and Mekata M 1991 *J. Phys. Soc. Jpn.* **60** 1885–1889
- [446] Mekata M, Yaguchi N, Takagi T, Mitsuda S and Yoshizawa H 1992 *J. Magn. Magn. Mater.* **104–107** 823–824
- [447] Mekata M, Yaguchi N, Takagi T, Sugino T, Mitsuda S, Yoshizawa H, Hosoi N and Shinjo T 1993 *J. Phys. Soc. Jpn.* **62** 4474–4487
- [448] Frontzek M, Ehlers G, Podlesnyak A, Cao H, Matsuda M, Zaharko O, Aliouane N, Barilo S and Shiryaev S V 2012 *J. Phys.: Condens. Matter* **24** 016004
- [449] Ehlers G, Podlesnyak A A, Frontzek M, Freitas R S, Ghivelder L, Gardner J S, Shiryaev S V and Barilo S 2013 *J. Phys.: Condens. Matter* **25** 496009
- [450] Kimura K, Nakamura H, Ohgushi K and Kimura T 2008 *Phys. Rev. B* **78** 140401
- [451] Seki S, Onose Y and Tokura Y 2008 *Phys. Rev. Lett.* **101** 067204
- [452] Soda M, Kimura K, Kimura T and Hirota K 2010 *Phys. Rev. B* **81** 100406
- [453] Mun E, Frontzek M, Podlesnyak A, Ehlers G, Barilo S, Shiryaev S V and Zapf V S 2014 *Phys. Rev. B* **89** 054411
- [454] Seki S, Yamasaki Y, Shiomi Y, Iguchi S, Onose Y and Tokura Y 2007 *Phys. Rev. B* **75** 100403
- [455] Kanetsuki S, Mitsuda S, Nakajima T, Anazawa D, Katori H A and Prokes K 2007 *J. Phys.: Condens. Matter* **19** 145244
- [456] Nakajima T, Mitsuda S, Haku T, Shibata K, Yoshitomi K, Noda Y, Aso N, Uwatoko Y and Terada N 2011 *J. Phys. Soc. Jpn.* **80** 014714
- [457] Nakajima T, Suno A, Mitsuda S, Terada N, Kimura S, Kaneko K and Yamauchi H 2011 *Phys. Rev. B* **84** 184401
- [458] Fukuda T, Nojiri H, Motokawa M, Asano T, Mekata M and Ajiro Y 1998 *Physica B: Condens. Matter* **246–247** 569–571
- [459] Terada N, Narumi Y, Sawai Y, Katsumata K, Staub U, Tanaka Y, Kikkawa A, Fukui T, Kindo K, Yamamoto T, Kanmuri R, Hagiwara M, Toyokawa H, Ishikawa T and Kitamura H 2007 *Phys. Rev. B* **75** 224411
- [460] Fishman R S, Ye F, Fernandez-Baca J A, Haraldsen J T and Kimura T 2008 *Phys. Rev. B* **78** 140407
- [461] Kimura T, Lashley J C and Ramirez A P 2006 *Phys. Rev. B* **73** 220401
- [462] Haraldsen J T, Swanson M, Alvarez G and Fishman R S 2009 *Phys. Rev. Lett.* **102** 237204
- [463] Terada N, Mitsuda S, Oohara Y, Yoshizawa H and Takei H 2004 *J. Magn. Magn. Mater.* **272–276** e997–e998
- [464] Terada N, Mitsuda S, Fujii T and Petitgrand D 2007 *J. Phys.: Condens. Matter* **19** 145241
- [465] Ye F, Fernandez-Baca J A, Fishman R S, Ren Y, Kang H J, Qiu Y and Kimura T 2007 *Phys. Rev. Lett.* **99** 157201
- [466] Fishman R S 2008 *J. Appl. Phys.* **103** 07B109
- [467] Frontzek M, Haraldsen J T, Podlesnyak A, Matsuda M, Christianson A D, Fishman R S, Sefat A S, Qiu Y, Copley J R D, Barilo S, Shiryaev S V and Ehlers G 2011 *Phys. Rev. B* **84** 094448
- [468] Takagi T and Mekata M 1995 *J. Phys. Soc. Jpn.* **64** 4609
- [469] Ye F, Ren Y, Huang Q, Fernandez-Baca J A, Dai P, Lynn J W and Kimura T 2006 *Phys. Rev. B* **73** 220404
- [470] Terada N, Mitsuda S, Ohsumi H and Tajima K 2006 *J. Phys. Soc. Jpn.* **75** 023602
- [471] Kimura S, Nishihagi N, Yamaguchi H, Kashiwagi T, Hagiwara M, Terada N and Kindo K 2010 *J. Low Temp. Phys.* **159** 80–83
- [472] Seki S, Kida N, Kumakura S, Shimano R and Tokura Y 2010 *Phys. Rev. Lett.* **105** 097207
- [473] Poienar M, Damay F, Martin C, Robert J and Petit S 2010 *Phys. Rev. B* **81** 104411
- [474] Lin S Z, Barros K, Mun E, Kim J W, Frontzek M, Barilo S, Shiryaev S V, Zapf V S and Batista C D 2014 *Phys. Rev. B* **89** 220405
- [475] Park K, Oh J, Leiner J C, Jeong J, Rule K C, Le M D and Park J G 2016 *Phys. Rev. B* **94** 104421
- [476] Kajimoto R, Tomiyasu K, Nakajima K, Ohira-Kawamura S, Inamura Y and Okuda T 2015 *J. Phys. Soc. Jpn.* **84** 074708
- [477] Töpfer J, Trari M, Gravereau P, Chaminade J P and Coumenc J P 1995 *Z. Kristallogr.* **210** 184–187
- [478] Damay F, Poienar M, Martin C, Maignan A, Rodriguez-Carvajal J, André G and Doumerc J P 2009 *Phys. Rev. B* **80** 094410
- [479] Ushakov A V, Streletsov S V and Khomskii D I 2014 *Phys. Rev. B* **89** 024406

[480] Vecchini C, Poienar M, Damay F, Adamopoulos O, Daoud-Aladine A, Lappas A, Perez-Mato J M, Chapon L C and Martin C 2010 *Phys. Rev. B* **82**(9) 094404

[481] Zorko A, Kokalj J, Komelj M, Adamopoulos O, Luetkens H, Arcón D and Lappas A 2015 *Sci. Rep.* **5** 9272

[482] Becca F and Mila F 2002 *Phys. Rev. Lett.* **89** 037204

[483] Terada N, Tsuchiya Y, Kitazawa H, Osakabe T, Metoki N, Igawa N and Ohoyama K 2011 *Phys. Rev. B* **84** 064432

[484] Bramwell S T, Carling S G, Harding C J, Harris K D M, Kariuki B M, Nixon L and Parkin I P 1996 *J. Phys.: Condens. Matter* **8** L123–L129

[485] Serrano-González H, Bramwell S T, Harris K D M, Kariuki B M, Nixon L, Parkin I P and Ritter C 1998 *J. Appl. Phys.* **83** 6314–6316

[486] Zhitomirsky M E 1996 *Phys. Rev. B* **54** 353–358

[487] Inami T, Ajiro Y and Goto T 1996 *J. Phys. Soc. Jpn.* **65** 2374–2376

[488] Serrano-González H, Bramwell S T, Harris K D M, Kariuki B M, Nixon L, Parkin I P and Ritter C 1999 *Phys. Rev. B* **59** 14451–14460

[489] Inami T 2007 *J. Sol. Stat. Chem.* **180** 2075–2079

[490] Sabelli C and Zanazzi P F 1972 *Acta Cryst. B* **28** 1182–1189

[491] Medenbach O and Gebert W 1993 *Neues Jahrb. Mineral. Monatsh.* (9) 401–407

[492] Pekov I V, Zubkova N V, Yapaskurt V O, Belakovskiy D I, Chukanov N V, Kasatkin A V, Kuznetsov A M and Pushcharovsky D Y 2013 *Mineral. Petrol.* **107** 201–210

[493] Sabelli C 1982 *Am. Mineral.* **67** 388–393

[494] Giester G, Rieck B and Brandstatter F 1998 *Mineral. Petrol.* **63** 19–34

[495] Mellini M and Merlino S 1978 *Z. Kristallogr.* **147** 129–140

[496] Sabelli C and Zanazzi P F 1968 *Acta Cryst. B* **24** 1214–1221

[497] Hawthorne F C, Krivovichev S V and Burns P C 2000 *Rev. Mineral. Geochem.* **40** 1–112

[498] Schindler M, Huminicki D M C and Hawthorne F C 2006 *Canad. Mineral.* **44** 1403–1429

[499] Momma K and Izumi F 2011 *J. Appl. Cryst.* **44** 1272–1276

[500] Shirata Y, Tanaka H, Matsuo A and Kindo K 2012 *Phys. Rev. Lett.* **108** 057205

[501] Zhou H D, Xu C, Hallas A M, Silverstein H J, Wiebe C R, Umegaki I, Yan J Q, Murphy T P, Park J H, Qiu Y, Copley J R D, Gardner J S and Takano Y 2012 *Phys. Rev. Lett.* **109** 267206

[502] Susuki T, Kurita N, Tanaka T, Nojiri H, Matsuo A, Kindo K and Tanaka H 2013 *Phys. Rev. Lett.* **110** 267201

[503] Ma J, Kamiya Y, Hong T, Cao H B, Ehlers G, Tian W, Batista C D, Dun Z L, Zhou H D and Matsuda M 2016 *Phys. Rev. Lett.* **116** 087201

[504] Li Y, Liao H, Zhang Z, Li S, Jin F, Ling L, Zhang L, Zou Y, Pi L, Yang Z, Wang J, Wu Z and Zhang Q 2015 *Sci. Rep.* **5** 16419

[505] Li Y, Chen G, Tong W, Pi L, Liu J, Yang Z, Wang X and Zhang Q 2015 *Phys. Rev. Lett.* **115** 167203

[506] Shen Y, Li Y D, Wo H, Li Y, Shen S, Pan B, Wang Q, Walker H C, Steffens P, Boehm M, Hao Y, Quintero-Castro D L, Harriger L W, Frontzek M D, Hao L, Meng S, Zhang Q, Chen G and Zhao J 2016 *Nature* **540** 559–562

[507] Xu Y, Zhang J, Li Y S, Yu Y J, Hong X C, Zhang Q M and Li S Y 2016 *Phys. Rev. Lett.* **117** 267202

[508] Li Y, Adroja D, Bewley R I, Voneshen D, Tsirlin A A, Gegenwart P and Zhang Q 2017 *Phys. Rev. Lett.* **118** 107202

[509] Li Y, Adroja D, Voneshen D, Bewley R I, Zhang Q, Tsirlin A A and Gegenwart P 2017 *Nature Commun.* **8** 15814

[510] Paddison J A M, Daum M, Dun Z, Ehlers G, Liu Y, Stone M B, Zhou H and Mourigal M 2017 *Nature Phys.* **13** 117–122

[511] Zhu Z, Maksimov P A, White S R and Chernyshev A L 2017 *Phys. Rev. Lett.* **119** 157201

[512] Baenitz M, Ranjith K M, Schlender P, Sichelschmidt J, Sarkar R, Khim S, Sokolov D A, Klauss H H, Yasuoka H, Mackenzie A P, Inosov D S and Doert T 2018 *Yb-delafoossites as pseudo spin-1/2 triangular magnets: magnetism, specific heat, NMR and the quest for spin liquids* contribution TT41.1 at the DPG Spring Meeting, <https://www.dpg-verhandlungen.de/year/2018/conference/berlin/part/tt/session/41>

[513] Sichelschmidt J, Baenitz M, Schlender P and Doert T 2018 *ESR on the S = 1/2 triangular magnet NaYbS₂* poster TT 72.57 at the DPG Spring Meeting, <https://www.dpg-verhandlungen.de/year/2018/conference/berlin/part/tt/session/72>

[514] Zhu Z and White S R 2015 *Phys. Rev. B* **92** 041105

[515] Iaconis J, Liu C, Halász G B and Balents L 2018 *SciPost Phys.* **4**(1) 003

- [516] Mumme W G, Sarp H and Chiappero P J 1994 *Arch. Sci. (Geneve)* **47** 117–124
- [517] Yoder C H, Bushong E, Liu X, Weidner V, McWilliams P, Martin K, Lorgunpai J, Haller J and Schaeffer R W 2010 *Mineral. Mag.* **74** 433–440
- [518] Effenberger H 1986 *Neues Jahrb. Mineral. Monatsh.* (3) 101–110
- [519] Fennell T, Piatek J O, Stephenson R A, Nilsen G J and Rønnow H M 2011 *J. Phys.: Condens. Matter* **23** 164201
- [520] Cooper M A and Hawthorne F C 1995 *Canad. Mineral.* **33** 1125–1129
- [521] Tsirlin A A, Belik A A, Shpanchenko R V, Antipov E V, Takayama-Muromachi E and Rosner H 2008 *Phys. Rev. B* **77** 092402
- [522] Nath R, Tsirlin A A, Rosner H and Geibel C 2008 *Phys. Rev. B* **78** 064422
- [523] Sengupta P, Batista C D, McDonald R D, Cox S, Singleton J, Huang L, Papageorgiou T P, Ignatchik O, Herrmannsdörfer T, Manson J L, Schlueter J A, Funk K A and Wosnitza J 2009 *Phys. Rev. B* **79** 060409
- [524] Tsirlin A A, Nath R, Abakumov A M, Furukawa Y, Johnston D C, Hemmida M, Krug von Nidda H A, Loidl A, Geibel C and Rosner H 2011 *Phys. Rev. B* **84** 014429
- [525] Li G L, Wu S Y, Kuang M Q, Hu X F and Xu Y Q 2017 *J. Struct. Chem.* **58** 700–705
- [526] Kawahara A 1976 *Mineral. J.* **8** 193–199
- [527] Koshelev A V, Zvereva E A, Chareev D A, Volkova O S, Vymazalova A, Laufek F, Kovalchuk E V, Rahaman B, Saha-Dasgupta T and Vasiliev A N 2016 *Phys. Chem. Miner.* **43** 43–49
- [528] Sarma K B N, Reddy B J and Lakshman S V J 1982 *Phys. Lett. A* **92** 305–308
- [529] Feng W L 2012 *Physica B: Condens. Matter* **407** 3865–3867
- [530] Lebernegg S, Tsirlin A A, Janson O, Redhammer G J and Rosner H 2016 *New J. Phys.* **18** 033020
- [531] Galy J, Jaud J, Pulou R and Sempère R 1984 *Bull. Mineral.* **107** 641–648
- [532] Gentsch M and Weber K 1984 *Acta Cryst. C* **40** 1309–1311
- [533] Dunn P J and Rouse R C 1975 *Mineral. Mag.* **40** 1–5
- [534] Hawthorne F C and Groat L A 1985 *Am. Mineral.* **70** 1050–1055
- [535] Mellini M and Merlino S 1979 *Z. Kristallogr.* **149** 249–257
- [536] Dabinett T R, Humberstone D, Leverett P and Williams P A 2008 *Pure Appl. Chem.* **80** 1317–1323
- [537] Zittlau A H, Shi Q, Boerio-Goates J, Woodfield B F and Majzlan J 2013 *Chemie der Erde* **73** 39–50
- [538] Castelnovo C, Moessner R and Sondhi S L 2012 *Annu. Rev. Condens. Matter Phys.* **3** 35–55
- [539] Kimchi I, Analytis J G and Vishwanath A 2014 *Phys. Rev. B* **90** 205126
- [540] Hermanns M, O'Brien K and Trebst S 2015 *Phys. Rev. Lett.* **114** 157202
- [541] O'Brien K, Hermanns M and Trebst S 2016 *Phys. Rev. B* **93** 085101
- [542] Wan Y and Kim Y B 2016 *Phys. Rev. B* **94** 224401
- [543] Chillal S, Iqbal Y, Jeschke H O, Rodriguez-Rivera J A, Bewley R, Manuel P, Khalyavin D, Steffens P, Thomale R, Islam A T M N, Reuther J and Lake B 2018 *A quantum spin liquid based on a new three-dimensional lattice* Preprint: arXiv:1712.07942 (unpublished)
- [544] Koteswararao B, Kumar R, Khuntia P, Bhowal S, Panda S K, Rahman M R, Mahajan A V, Dasgupta I, Baenitz M, Kim K H and Chou F C 2014 *Phys. Rev. B* **90** 035141
- [545] Khuntia P, Bert F, Mendels P, Koteswararao B, Mahajan A V, Baenitz M, Chou F C, Baines C, Amato A and Furukawa Y 2016 *Phys. Rev. Lett.* **116** 107203
- [546] Powell D W, Thomas R G, Williams P A, Birch W D and Plimer I R 1994 *Mineral. Mag.* **58** 505
- [547] Gaulin B D and Gardner J S 2011 *Experimental Studies of Pyrochlore Antiferromagnets* in Lacroix C, Mendels P, and Mila F (eds) *Introduction to Frustrated Magnetism* (Springer Series in Solid-State Sciences, vol **164**, 2nd ed, Springer-Verlag Berlin) pp 177–206
- [548] Gaulin B D and Gardner J S 2013 *Experimental Studies of Frustrated Pyrochlore Antiferromagnets* in Diep, H T (ed) *Frustrated Spin Systems* (World Scientific, Singapore) pp 475–507
- [549] Takagi H and Niitaka S 2011 *Highly Frustrated Magnetism in Spinels* in Lacroix C, Mendels P, and Mila F (eds) *Introduction to Frustrated Magnetism* (Springer Series in Solid-State Sciences, vol **164**, 2nd ed, Springer-Verlag Berlin) pp 155–175
- [550] Reimers J N, Berlinsky A J and Shi A C 1991 *Phys. Rev. B* **43** 865–878
- [551] Okubo T, Nguyen T H and Kawamura H 2011 *Phys. Rev. B* **84** 144432
- [552] Tymoshenko Y V, Onykiienko Y A, Müller T, Thomale R, Rachel S, Cameron A S, Portnichenko P Y, Efremov D V,

Tsurkan V, Abernathy D L, Ollivier J, Schneidewind A, Piovano A, Felea V, Loidl A and Inosov D S 2017 *Phys. Rev. X* **7** 041049

[553] Gingras M J P 2011 *Spin Ice* in Lacroix C, Mendels P and Mila F (eds) *Introduction to Frustrated Magnetism* (Springer Series in Solid-State Sciences, vol **164**, 2nd ed, Springer-Verlag Berlin) pp 293–329

[554] Henley C L 2009 *J. Phys.: Conf. Ser.* **145** 012022

[555] Talanov V M, Shirokov V B and Talanov M V 2015 *Acta Cryst. A* **71** 301–318

[556] Hopkinson J M, Isakov S V, Kee H Y and Kim Y B 2007 *Phys. Rev. Lett.* **99** 037201

[557] Lawler M J, Paramekanti A, Kim Y B and Balents L 2008 *Phys. Rev. Lett.* **101** 197202

[558] Zhou Y, Lee P A, Ng T K and Zhang F C 2008 *Phys. Rev. Lett.* **101** 197201

[559] Lawler M J, Kee H Y, Kim Y B and Vishwanath A 2008 *Phys. Rev. Lett.* **100** 227201

[560] Bergholtz E J, Läuchli A M and Moessner R 2010 *Phys. Rev. Lett.* **105** 237202

[561] Singh R R P and Oitmaa J 2012 *Phys. Rev. B* **85** 104406

[562] Chen G and Balents L 2008 *Phys. Rev. B* **78** 094403

[563] Kimchi I and Vishwanath A 2014 *Phys. Rev. B* **89** 014414

[564] Shindou R 2016 *Phys. Rev. B* **93** 094419

[565] Mizoguchi T, Hwang K, Lee E K H and Kim Y B 2016 *Phys. Rev. B* **94** 064416

[566] Buessen F L and Trebst S 2016 *Phys. Rev. B* **94** 235138

[567] Huang B, Kim Y B and Lu Y M 2017 *Phys. Rev. B* **95** 054404

[568] Nussinov Z and van den Brink J 2015 *Rev. Mod. Phys.* **87** 1–59

[569] Kitaev A 2006 *Ann. Phys.* **321** 2–111

[570] Chaloupka J, Jackeli G and Khaliullin G 2010 *Phys. Rev. Lett.* **105** 027204

[571] Reuther J, Thomale R and Trebst S 2011 *Phys. Rev. B* **84** 100406

[572] Lee E K H, Schaffer R, Bhattacharjee S and Kim Y B 2014 *Phys. Rev. B* **89** 045117

[573] Hermanns M and Trebst S 2014 *Phys. Rev. B* **89** 235102

[574] Lee E K H and Kim Y B 2015 *Phys. Rev. B* **91** 064407

[575] Halász G B, Perreault B and Perkins N B 2017 *Phys. Rev. Lett.* **119** 097202

[576] Krivovichev S V, Hawthorne F C and Williams P A 2017 *Struct. Chem.* **28** 153–159

[577] Pollard A M, Thomas R G and Williams P A 1989 *Mineral. Mag.* **53** 557–563

[578] Malcherek T, Mihailova B and Welch M D 2017 *Phys. Chem. Miner.* **44** 307–321

[579] Jambor J L, Dutrizac J E, Roberts A C, Grice J D and Szymanski J T 1996 *Can. Mineral.* **34** 61–72

[580] Zheng X G, Mori T, Nishiyama K, Higemoto W, Yamada H, Nishikubo K and Xu C N 2005 *Phys. Rev. B* **71** 174404

[581] Kang J, Lee C and Whangbo M H 2009 *Study of the magnetic structures of the atacamite and botallackite forms of Cu₂(OH)₃Cl in terms of first-principles DFT calculations*, abstract #K1.103 at the 2009 APS March Meeting, <http://adsabs.harvard.edu/abs/2009APS..MAR.K1103K>

[582] Mori W and Yamaguchi K 1995 *Mol. Cryst. Liq. Cryst. Sci. Technol. Sect. A* **274** 113–118

[583] Zheng X G and Otabe E S 2004 *Sol. Stat. Commun.* **130** 107

[584] Zenmyo K, Kubo H, Tokita M, Hamasaki T, Hagihala M, Zheng X G, Kawae T, Takeuchi Y and Matsumura M 2013 *J. Phys. Soc. Jpn.* **82** 084707

[585] Heinze L, Beltran-Rodriguez R, Bastien G, Wolter A U B, Reehuis M, Hoffmann J U, Rule K C and Süllow S 2018 *Physica B: Condens. Matter* **536** 377–378

[586] Zheng X, Hagihala M, Nishiyama K and Kawae T 2009 *Physica B: Condens. Matter* **404** 677–679

[587] Maegawa S, Oyamada A and Sato S 2010 *J. Phys. Soc. Jpn.* **79** 011002

[588] Zheng X G, Yamashita T, Hagihala M, Fujihala M and Kawae T 2009 *Physica B: Condens. Matter* **404** 680–682

[589] Zheng X G, Kawae T, Kashitani Y, Li C S, Tateiwa N, Takeda K, Yamada H, Xu C N and Ren Y 2005 *Phys. Rev. B* **71** 052409

[590] Zheng X G, Kubozono H, Nishiyama K, Higemoto W, Kawae T, Koda A and Xu C N 2005 *Phys. Rev. Lett.* **95** 057201

[591] Zheng X G, Kawae T, Yamada H, Nishiyama K and Xu C N 2006 *Phys. Rev. Lett.* **97** 247204

[592] Zheng X G, Hagihala M and Toriyi T 2007 *J. Magn. Magn. Mater.* **310** 1288–1290

[593] Hagihala M, Zheng X G, Toriyi T and Kawae T 2007 *J. Phys.: Condens. Matter* **19** 145281

[594] Liu X D, Zheng X G, Meng D D, Xu X L and Guo Q X 2013 *J. Phys.: Condens. Matter* **25** 256003

[595] Nishiyama M, Oyamada A, Itou T, Maegawa S, Okabe H and Akimitsu J 2011 *J. Phys.: Conf. Ser.* **320** 012030

[596] Krivovichev S V, Filatov S K and Burns P C 2002 *Canad. Mineral.* **40** 1185–1190

[597] Okabe H, Suzuki K, Kawashima K, Muranaka T and Akimitsu J 2006 *J. Phys. Soc. Jpn.* **75** 123705

[598] Kawashima K, Okabe H, Suzuki K, Kuroiwa S, Akimitsu J, Sato K H, Koda A and Kadono R 2007 *J. Phys.: Condens. Matter* **19** 145275

[599] Zhao L, Fernández-Díaz M T, Tjeng L H and Komarek A C 2016 *Sci. Adv.* **2** e1600353

[600] Tokura Y and Seki S 2010 *Adv. Mater.* **22** 1554–1565

[601] Pinsard-Gaudart L, Rodríguez-Carvajal J, Gukasov A and Monod P 2004 *Phys. Rev. B* **69** 104408

[602] Christy A G, Mills S J and Kampf A R 2016 *Mineral. Mag.* **80** 415–545

[603] Lam A E, Groat L A, Grice J D and Ercit T S 1999 *Canad. Mineral.* **37** 721–729

[604] Ahmed N, Tsirlin A A and Nath R 2015 *Phys. Rev. B* **91** 214413

[605] Koteswararao B, Panda S K, Kumar R, Yoo K, Mahajan A V, Dasgupta I, Chen B H, Kim K H and Chou F C 2015 *J. Phys.: Condens. Matter* **27** 426001

[606] Mitchell R H, Welch M D and Chakhmouradian A R 2017 *Mineral. Mag.* **81** 411–461

[607] Krivovichev S V 2008 *Z. Kristallogr.* **223** 109–113

[608] Price P M, Browning N D and Butt D P 2015 *J. Am. Ceram. Soc.* **98** 2248–2254

[609] Kagomiya I, Hirota Y, ichi Kakimoto K, Fujii K, Shiraiwa M, Yashima M, Fuwa A and Nakamura S 2017 *Phys. Chem. Chem. Phys.* **19** 31194

[610] Phan T L, Tho P T, Tran N, Kim D H, Lee B W, Yang D S, Thiet D V and Cho S L 2018 *J. Electron. Mater.* **47** 188–195

[611] Schnack J 2004 *Molecular magnetism* in Schollwöck U, Richter J, Farnell D J J, and Bishop R F (eds) *Quantum Magnetism* (Lecture Notes in Physics vol **645**, Springer Berlin Heidelberg) pp 155–194

[612] Gatteschi D, Sessoli R and Villain J 2006 *Molecular Nanomagnets* (Oxford University Press, Oxford)

[613] Schnalle R and Schnack J 2010 *Int. Rev. Phys. Chem.* **29** 403–452

[614] Furrer A and Waldmann O 2013 *Rev. Mod. Phys.* **85** 367–420

[615] Bartolomé J, Luis F and Fernández J F (eds) 2014 *Molecular Magnets* (Springer-Verlag Berlin Heidelberg)

[616] Caciuffo R, Amoretti G, Murani A, Sessoli R, Caneschi A and Gatteschi D 1998 *Phys. Rev. Lett.* **81** 4744–4747

[617] Schmidt R, Richter J and Schnack J 2005 *J. Magn. Magn. Mater.* **295** 164–167

[618] Schröder C, Nojiri H, Schnack J, Hage P, Luban M and Kögerler P 2005 *Phys. Rev. Lett.* **94** 017205

[619] Kögerler P, Tsukerblat B and Müller A 2010 *Dalton Trans.* **39** 21–36

[620] Müller A, Luban M, Schröder C, Modler R, Kögerler P, Axenovich M, Schnack J, Canfield P, Bud'ko S and Harrison N 2001 *Chem. Phys. Chem.* **2** 517–521

[621] Garlea V O, Nagler S E, Zarestky J L, Stassis C, Vaknin D, Kögerler P, McMorrow D F, Niedermayer C, Tennant D A, Lake B, Qiu Y, Exler M, Schnack J and Luban M 2006 *Phys. Rev. B* **73** 024414

[622] Rousouchatzakis I, Läuchli A M and Mila F 2008 *Phys. Rev. B* **77** 094420

[623] Schnack J and Schnalle R 2009 *Polyhedron* **28** 1620–1623

[624] Schnack J and Wendland O 2010 *Eur. Phys. J. B* **78** 535–541

[625] Konstantinidis N P 2005 *Phys. Rev. B* **72** 064453

[626] Konstantinidis N P 2015 *J. Phys.: Condens. Matter* **27** 076001

[627] Cordsen A 1978 *Can. Mineral.* **16** 153

[628] Rojo J M, Mesa J L, Lezama L, Barberis G E and Rojo T 1996 *J. Magn. Magn. Mater.* **157/158** 493–495

[629] Belik A A, Koo H J, Whangbo M H, Tsujii N, Naumov P and Takayama-Muromachi E 2007 *Inorg. Chem.* **46** 8684–8689

[630] Kuo C N and Lue C S 2008 *Phys. Rev. B* **78** 212407

[631] Matsuda M, Dissanayake S E, Abernathy D L, Totsuka K and Belik A A 2015 *Phys. Rev. B* **92** 184428

[632] Rojo J M, Mesa J L, Lezama L, Pizarro J L, Arriortua M I, Fernandez J R, Barberis G E and Rojo T 2002 *Phys. Rev. B* **66** 094406

[633] de Pedro I, Rojo J M, Rodríguez Fernández J, Fernández-Díaz M T and Rojo T 2010 *Phys. Rev. B* **81** 134431

[634] de Pedro I, Rojo J M, Pizarro J L, Fernández J R, Marcos J S, Fernández-Díaz M T, Arriortua M and Rojo T 2007 *J. Mater. Chem.* **17** 3915–3926

[635] Karmakar D and Yakhmi J V 2012 *J. Phys.: Condens. Matter* **24** 436003

[636] Pedro I, Rojo J M, Pizarro J L, Fernández J R, Marcos J S, Fernández-Díaz M T, Arriortua M I and Rojo T 2006 *J. Phys.: Condens. Matter* **18** 3767–3787

[637] Pedro I, Rojo J M, Fernández J R, Marcos J S, Fernández-Díaz M T and Rojo T 2012 *J. Sol. Stat. Chem.* **188** 1–10

[638] Rouse R C 1973 *J. Sol. Stat. Chem.* **6** 86–92

[639] Cooper M A and Hawthorne F C 2000 *The Canadian Mineralogist* **38** 801–808

[640] Dreier E S, Holm S L, Lønbæk K, Hansen U B, Medarde M, Živković I, Babkevich P, Ruminy M, Casati N, Piovano A, Rols S, Nilsen G J, Boehm M, Skoulatos M, Schefer J, Rønnow H M, Fennell T and Lefmann K 2018 *Phys. Rev. B* **97** 014416

[641] Giuseppetti G, Mazzi F and Tadini C 1992 *Neues Jahrb. Mineral. Monatsh.* (3) 113–126

[642] Hawthorne F C and Groat L A 1986 *Mineral. Mag.* **50** 157–162

[643] Armbruster T and Gunter M E 2001 *Rev. Mineral. Geochem.* **45** 1–67

[644] Effenberger H, Giester G, Krause W and Bernhardt H J 1998 *Am. Mineral.* **83** 607–617

[645] Schmidt R, Schnack J and Richter J 2005 *J. Magn. Magn. Mater.* **295** 164

[646] Herndon J M and Rowe M W 1974 *Meteoritics* **53** 289–305

[647] Devey A J, Grau-Crespo R and de Leeuw N H 2008 *J. Phys. Chem. C* **112** 10960

[648] Subedi A, Zhang L, Singh D J and Du M H 2008 *Phys. Rev. B* **78** 134514

[649] Tresca C, Giovannetti G, Capone M and Profeta G 2017 *Phys. Rev. B* **95** 205117

[650] Kuhn S J, Kidder M K, Parker D S, dela Cruz C, McGuire M A, Chance W M, Li L, Debeer-Schmitt L, Ermentrout J, Littrell K C, Eskildsen M R and Sefat A S 2017 *Physica C: Superconductivity* **534** 29–36

[651] Lai X, Zhang H, Wang Y, Wang X, Zhang X, Lin J and Huang F 2015 *J. Am. Chem. Soc.* **137** 10148–10151

[652] Zhang J, Liu F L, Ying T P, Li N N, Xu Y, He L P, Hong X C, Yu Y J, Wang M X, Shen J, Yang W G and Li S Y 2017 *npj Quant. Mater.* **2** 49

[653] Johnston D C 2010 *Adv. Phys.* **59** 803–1061

[654] Stewart G R 2011 *Rev. Mod. Phys.* **83** 1589–1652

[655] Lennie A R, Redfern S A T, Schofield P F and Vaughan D J 1995 *Mineral. Mag.* **59** 677–683

[656] Lennie A R and Vaughan D J 1996 *Mineral. Spec.* **5** 117–130

[657] Lennie A R, Redfern S A T, Champness P E, Stoddart C P, Schofield P F and Vaughan D J 1997 *Am. Mineral.* **82** 302–309

[658] Mullet M, Boursiquot S, Abdelmoula M, Génin J M and Ehrhardt J J 2002 *Geochim. Cosmochim. Acta* **66** 829–836

[659] Kwon K D, Refson K and Sposito G 2015 *Am. Mineral.* **100** 1509–1517

[660] Wilkin R T and Beak D G 2017 *Chem. Geol.* **462** 15–29

[661] Mizuguchi Y, Tomioka F, Tsuda S, Yamaguchi Y and Takano Y 2009 *J. Phys. Soc. Jpn.* **78** 074712

[662] Man H, Guo J, Zhang R, Schönemann R, Yin Z, Fu M, Stone M B, Huang Q, Song Y, Wang W, Singh D J, Lochner F, Hickel T, Eremin I, Harriger L, Lynn J W, Broholm C, Balicas L, Si Q and Dai P 2017 *npj Quant. Mater.* **2** 14

[663] Vaughan D J and Ridout M S 1971 *J. Inorg. Nucl. Chem.* **33** 741–746

[664] Kwon K D, Refson K, Bone S, Qiao R, Yang W I, Liu Z and Sposito G 2011 *Phys. Rev. B* **83** 064402

[665] Hao N, Zheng F, Zhang P and Shen S Q 2017 *Phys. Rev. B* **96** 165102

[666] Kirschner F K K, Lang F, Topping C V, Baker P J, Pratt F L, Wright S E, Woodruff D N, Clarke S J and Blundell S J 2016 *Phys. Rev. B* **94** 134509

[667] Dai P 2015 *Rev. Mod. Phys.* **87** 855–896

[668] Inosov D S 2016 *C. R. Physique* **17** 60–89

[669] Feder T 2014 *Physics Today* **67** 20

[670] Leonyuk L, Babonas G J, Pushcharovskii D Y and Maltsev V 1998 *Crystallogr. Rep.* **43** 256–270

[671] Leonyuk L, Maltsev V, Babonas G J, Szymczak R, Szymczak H and Baran M 2001 *Acta Cryst. A* **57** 34–39

[672] Hsieh D, Wu H C, Kakarla D C, Chang C K, Chuang Y C, Berger H and Yang H D 2018 *Multiferroic properties in chloromenite Cu₉O₂(SeO₃)₄Cl₆* poster T60.2 at the APS March Meeting, <http://meetings.aps.org/Meeting/MAR18/Session/T60.2>

[673] Bao R L, Kong Z P, Gu M, Yue B, Weng L H and He H Y 2006 *Chem. Res. Chin. Univ.* **22** 679–683

[674] Vilminot S, André G, Richard-Plouet M, Bourée-Vigneron F and Kurmoo M 2006 *Inorg. Chem.* **45** 10938–10946

[675] Vilminot S, André G and Kurmoo M 2009 *Inorg. Chem.* **48** 2687–2692

[676] Hase M, Kuroe H, Pomjakushin V Y, Keller L, Tamura R, Terada N, Matsushita Y, Dönni A and Sekine T 2015

Phys. Rev. B **92** 054425

- [677] Groat L A and Hawthorne F C 1990 *Am. Mineral.* **75** 1170–1175
- [678] Eby R K and Hawthorne F C 1989 *Mineral. Petrol.* **40** 127–136
- [679] Shoemaker G L, Anderson J B and Kostiner E 1977 *Am. Mineral.* **62** 1042–1048
- [680] Arlt T and Armbruster T 1999 *Neues Jahrb. Mineral. Monatsh.* (10) 468–480
- [681] Krivovichev S V, Filatov S K and Burns P C 2001 *Proc. Russ. Mineral. Soc.* **130**(5) 1–8
- [682] Menchetti S, Bindi L, Bonazzi P and Olmi F 2002 *Am. Mineral.* **87** 721–725
- [683] Bosi F, Belardi G and Ballirano P 2009 *Am. Mineral.* **94** 74–82
- [684] Hawthorne F C and Ferguson R B 1975 *Acta Cryst. B* **31** 1753–1755
- [685] Bao S, Wang J, Wang W, Cai Z, Li S, Ma Z, Wang D, Ran K, Dong Z Y, Abernathy D L, Yu S L, Wan X, Li J X and Wen J 2018 *Observation of Dirac magnons in a three-dimensional antiferromagnet* Preprint: arXiv:1711.02960 (unpublished)
- [686] Carbone C, Basso R, Cabella R, Martinelli A, Grice J D and Lucchetti G 2013 *Am. Mineral.* **98** 1899–1905
- [687] Yao W, Li C, Wang L, Xue S, Dan Y, Iida K, Kamazawa K, Li K, Fang C and Li Y 2018 *Topological spin excitations observed in a three-dimensional antiferromagnet* Preprint: arXiv:1711.00632 (unpublished)
- [688] Herak M, Berger H, Prester M, Miljak M, Živković I, Milat O, Drobac D, Popović S and Zaharko O 2005 *J. Phys.: Condens. Matter* **17** 7667–7679
- [689] Måansson M, Prša K, Sugiyama J, Andreica D, Luetkens H and Berger H 2012 *Phys. Procedia* **30** 142–145
- [690] He Z and Itoh M 2014 *J. Magn. Magn. Mater.* **354** 146–150
- [691] Margison S M, Grice J D and Groat L A 1997 *Canad. Mineral.* **35** 759–763
- [692] Grice J D, Groat L A and Roberts A C 1996 *Canad. Mineral.* **34** 55–59
- [693] Mills S J, Kampf A R, Poirier G, Raudsepp M and Steele I M 2010 *Miner. Petrol.* **99** 113–120
- [694] Keller P and Hess H 1978 *Neues Jahrb. Mineral. Abhandl.* **133** 291–302